Hierarchical nanofluidic exchanger to harvest ion current from salinegradient.

Saranath Sripriya

THÈSE

Pour obtenir le grade de

DOCTEUR DE L'UNIVERSITÉ GRENOBLE ALPES

École doctorale : PHYS - Physique
Spécialité : Nanophysique
Unité de recherche : Laboratoire Interdisciplinaire de Physique

Echangeur nanofluidique hiérarchique pour exploiter les courants ioniques issus de gradients salins

Hierarchical nanofluidic exchanger to harvest ion current from saline gradient.

Présentée par :

Saranath SRIPRIYA

Direction de thèse :

Elisabeth CHARLAIX Professeur des Universités, Université Grenoble Alpes	Directrice de thèse
Cyril PICARD MAITRE DE CONFERENCES, Université Grenoble Alpes	Co-encadrant de thèse
Frank FOURNEL Expert international CEA, CEA	Co-encadrant de thèse

Rapporteurs :

RENE VAN ROIJ
Professeur, Universiteit Utrecht
ANNE-LAURE BIANCE
Directeur de recherche, CNRS DELEGATION RHONE AUVERGNE

Thèse soutenue publiquement le **24 mars 2023**, devant le jury composé de :

RENE VAN ROIJ Professeur, Universiteit Utrecht	Rapporteur
HUGUES BODIGUEL Professeur des Universités, GRENOBLE INP	Président
ANNE-LAURE BIANCE Directeur de recherche, CNRS DELEGATION RHONE AUVERGNE	Rapporteure
FRANÇOIS RIEUTORD Ingénieur HDR, SOITEC	Examinateur

Invités :

VINCENT LARREY
Ingénieur docteur, CEA CENTRE DE GRENOBLE

March 24, 2023

Hierarchical Nanofluidic Exchanger to harvest Ion Current from Saline Gradient

Saranath Sripriya

Laboratoire Interdisciplinaire de Physique
Université Grenoble Alpes

Thesis Advisors:
Prof. Elisabeth Charlaix
Dr. Cyril Picard
Dr. Frank Fournel

A dissertation submitted in partial fulfillment of the requirements for the degree of Doctor of Philosophy in Physics

I dedicate this manuscript to the woman who taught me how to dream big.
She then dedicated her life to provide me with the means to achieve that dream.
This PhD has been my dream come true and I owe it all to your selfless sacrifices.
Thank you, Maa!

If you look for the light, you can often find it; but if you look for the dark that is all you will ever see.

— Iroh.

Acknowledgements

I want to start by saying how grateful I am to my thesis supervisor, Elisabeth Charlaix, for her unwavering encouragement and trust in me. I still recall the sense of pride I felt when I was offered this position and also the existential dread that washed over me as I panicked about not being able to live up to your expectations. You helped me not only become a better researcher but also a more self-assured adult overall, with your calming influence and your never-ending support. I had never considered being a theoretical physicist before I joined LIPhy, but after our numerous five-hour meetings together over the last four years, there is nothing else I would rather be. I still remember your response when I approached you during my first year of my PhD and expressed my concern that I wasn't adding enough to the scientific discourse. You responded with your usual composure, "*Saranath, I have spent more time as a researcher than you have been alive. You don't need to contribute anything right now; just keep up with me, and in a year you'll be the one giving me instructions on this project.*" I will always be appreciative of the times when you had faith in me even if I had lost faith in myself.

Additionally, I want to thank my co-supervisor Cyril Picard for supporting me when I needed it and for mediating between Elisabeth and myself, particularly during the end of my thesis. Without your help, I could not have completed this PhD. Despite your hectic teaching schedule, you always made time for me and helped me grasp the project well. Your contrasting strategy complements with Elisabeth's extremely well in creating a thorough understanding of a subject. I consider myself tremendously fortunate to have witnessed how we may tackle the same issue from a variety of angles.

I would like to convey my appreciation to Frank Fournel and Vincent Larrey from CEA-Leti for their time and helpful conversations regarding the experimental im-

plementation of my proposed device. I would like to thank Anne Laure Biance from ILM, Lyon who was a member of my suivi de thése committee, for her contribution to this project. Your questions and comments were very beneficial to the development of this thesis. I want to express my sincere gratitude to Kirsten Martens in particular, who acted as a mediator between me and my supervisors. You were patient and proactive in assisting me whenever I had any problems and I cannot overstate how helpful you were throughout my thesis.

This list would be incomplete without mentioning the contribution of a sizable group of people I had the good pleasure to call friends. I'd want to express my gratitude to David, Vincent, Gonzalo, Nil, Akash, Erik, Celine, Nathaniel, Artur, Saire, Adrien, Dandara, Edouardo, Laila, Luiza, Andrea, Maaike, Wanda, Raj, George, Caroline, Cecile, Gautier and others. Throughout my time in France, you have made me feel incredibly welcomed and appreciated. I will never truly forget that you were there for me during the most eventful times of my life.

I have been tremendously fortunate to have family's constant support throughout my life. My grandfather and uncle were the first to encourage me to pursue a PhD and I thank you for always being such an inspiration. I strive to be as dedicated and tenacious as my grandmother, the most determined woman I know. I'd want to express my gratitude to all my cousins, particularly Hiranmayee and Srikanth, for your encouraging words and reassurance during the most trying times of my thesis.

Last but not least, words can't express how grateful I am to my mother and how much I admire her. You have been a rock for me, and everything I am and will be is entirely due to you and the tremendous sacrifices you have made. You've spent your entire life working for my benefit, so now that I'm going to be a doctor, you might want to think about living a little bit for yourself. Your boy finally made it!

Abstract

The mixing of two electrolyte solutions of different concentrations is characterized by a free enthalpy of mixing. The conversion of this enthalpy into useful mechanical work or electricity has the potential to be a new source of clean renewable energy. The energy generated by this process is termed as "osmotic energy", or more specifically "blue energy" when energy is generated by the mixing of sea water with river water. The necessity to drastically lessen the world's reliance on fossil fuels and the remarkable advancement of membrane technology have encouraged the development of novel techniques for harvesting blue energy. The establishment of large-scale power plants focused at harvesting this energy revealed some inherent limitations in membrane-based approaches for the extraction of blue energy, most notably concentration polarization. This manuscript proposes a silicon-based nanofluidic exchanger, which aims at optimizing the coupled solute transport at the microscale and nanoscale to minimize concentration polarization issues and enhance energy recovery. The focus of this manuscript is on the theoretical modelling of the exchanger and the optimization of the exchanger reveals an expected power density two magnitudes higher than existing strategies aimed at blue energy harvesting. These theoretical results are used to propose a fabrication protocol for a Multiscale Exchanger, in collaboration with CEA-Leti, incorporating recent developments of the microfabrication industry to produce minute channels with a large potential for parallelization.

Resumé

Le mélange de deux solutions électrolytiques de concentrations différentes est caractérisé par une enthalpie libre de mélange. Sa conversion en travail mécanique utile ou en électricité peut constituer une source d'énergie renouvelable propre communément appelée "énergie osmotique" ou "énergie bleue" dans le cas du mélange d'eau de rivière et d'eau de mer. La nécessité de réduire drastiquement notre dépendance aux combustibles fossiles et le développement remarquable de nouvelles membranes sélectives ont encouragé la mise au point de nouvelles techniques d'extraction de l'énergie bleue. La mise en place de centrales électriques à grande échelle a permis d'identifier certaines limites inhérentes aux approches membranaires pour l'extraction de l'énergie bleue, notamment la polarisation de concentration. Dans ce manuscrit, nous présentons un échangeur nanofludique à base de silicium qui vise à optimiser le transport couplé des solutés à l'échelle nanométrique et à l'échelle microscopique afin de minimiser les problèmes de polarisation de concentration et d'augmenter la récupération d'énergie. L'accent est mis sur la modélisation théorique d'un tel échangeur. Des densités de puissance de deux ordres de magnitudes supérieures aux stratégies existantes sont ainsi prédites. Ces résultats théoriques ont été utilisés pour concevoir un protocole de fabrication d'un échangeur multi-échelle, en collaboration avec le CEA-Leti, incorporant les développements récents de l'industrie de la microfabrication pour produire une série de canaux infimes massivement parallélisés. La dernière section du manuscrit discute d'un tel potentiel de parallélisation, qui pourrait conduire à un changement de paradigme dans la génération d'énergie basée sur le gradient de salinité en utilisant des nanopores.

Table of Contents

List of Symbols

$\boldsymbol{D}, \boldsymbol{D^{\pm}}$	Coefficient of diffusion of species [m^2/s]
$\boldsymbol{c_{h,l}}$	Local Microchannel Concentrations (high/low) [atoms/m^3]
$\boldsymbol{C_{h,l}}$	Local Microchannel Concentrations (high/low) [mol/m^3]
$\boldsymbol{c_{H,L}}$	Entrance Microchannel Concentrations (high/low) [atoms/m^3]
$\boldsymbol{c_{h,l}^{nano}}$	Nanochannel Concentration at micro-nano interface [atoms/m^3]
$\boldsymbol{c_s}; \boldsymbol{C_s}$	$c_h + c_l$ in [atoms/m^3] or [mol/m^3]
$\boldsymbol{c_d}; \boldsymbol{C_d}$	$c_h - c_l$ in [atoms/m^3] or [mol/m^3]
$\boldsymbol{c_S}, \boldsymbol{c_D}$	$c_H + c_L$ and $c_H + c_L$ [atoms/m^3]
$\boldsymbol{c^+}, \boldsymbol{c^-}$	Local cation/anion concentration inside nanochannel [ions/m^3]
$\boldsymbol{a}, \boldsymbol{b}, \boldsymbol{S_M}, \boldsymbol{L}$	Microchannel depth, width, cross sectional area and exchanger length
$\boldsymbol{H}, \boldsymbol{W}$	Nanochannel height and width
$\boldsymbol{\vec{U}}$	Convection Velocity inside microchannels [m/s]
$\boldsymbol{V_{H,L}}$	Potential inside high/low concentration microchannel [V]
$\boldsymbol{\Psi}$	Normalized microchannel potential (eq.2.6)
$\boldsymbol{\sigma}$	Nanochannel surface charge [C/m^2]
$\boldsymbol{S}$	Nanochannel selectivity (eq.3.3)
$\boldsymbol{J_{nano}^{\pm}}$	Cationic/Anionic nanochannel flux per unit exchanger length [atoms/m^3]
$\boldsymbol{J_{elec}}$	Electrode flux per unit exchanger length [atoms/m^3]
$\boldsymbol{K^{\pm}}$	Normalized nanochannel flux (eq.3.2)
$\boldsymbol{Sh}, \boldsymbol{Pe}$	Sherwood and Péclet number (eq.2.6)
$\boldsymbol{P_{elec}}$	Electrical power generated by exchanger [W]
$\boldsymbol{Pd_{elec}}$	Electrical power generated per unit surface of exchanger [W/m^2]
$\boldsymbol{Du_{h,l}}$	Local Dukhin numbers inside the nanochannel (eq.3.7)
$\boldsymbol{\mathcal{E}}$	Electromotive force equivalent for the exchanger (eq.3.16)

CHAPTER 1

Introduction

1.1 Nanofluidics and a brief history of *Blue Energy*

Nanofluidics refer to the branch of fluid mechanics focused on understanding the dynamics of liquids in or around objects with at least one characteristic dimension less than 100 nm[1,2]. This subsidiary of fluid dynamics started gaining popularity around mid-2000s due to the advancements in the field of microfabrication techniques including, but not limited to, *Silicon-on-Insulator (SoI)*[3] and *Scanning Tunnelling Microscopy*[4]. These techniques enabled the assembly and inspection of features with nanometric dimensions. These fabrication techniques gave way to the rise of microfluidics in *lab-on-chip* sensors[5,6] and eventually, the demand for increased sophistication and miniaturization of chips resulted in the evolution of microfluidics into nanofluidics. The field of nanofluidics is attractive in terms of research, chiefly, as it opens the avenue for fluids to demonstrate new physical phenomenon, which were previously unobserved in macroscopic and microscopic length scales. These phenomenon include effects such as *Debye Overlap* leading to selective permeability of ions through a nanopore[7] and also surface charge governed transport[8]. Analytical and experimental research on these "new" physical phenomenon under nanofluidics led to the observance of a few characteristics, previously only studied in the context of microelectronics, for example, nanofluidic diodes and nanofluidic batteries[9].

One such application of nanofluidics extended toward generation of electricity using salinity difference between two distinct sources of water. This energy derived

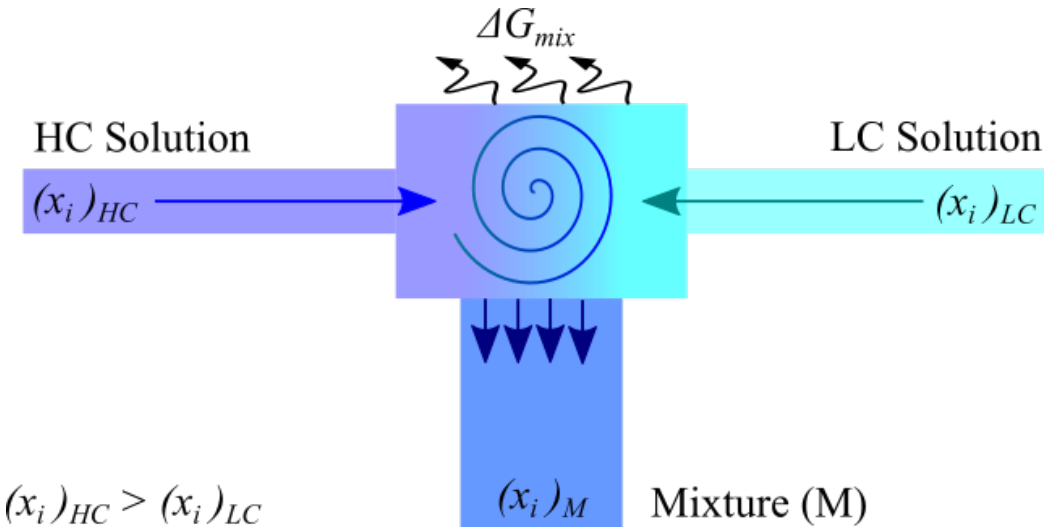

Figure 1.1: Energy release associated with the mixing process. HC, LC and M represent high, low concentration solutions and the resulting mixture respectively. The symbol x_i refers to the mole fraction of species i in the corresponding solution. The mixing energy ΔG_{mix} can be evaluated from eq. 1.1.

from the difference of salt concentrations in water was termed as *Osmotic Energy* or *Blue Energy* when the two sources were sea water and river water. When two solutions of electrolytes of different concentrations are allowed to mix together, the process is accompanied by a release of energy. Osmotic energy refers to the conversion of the released mixing energy into electricity or useful work. The maximum theoretical energy that can be extracted from the mixing of a strong electrolyte that undergoes complete dissociation in water is equal to the Gibb's free energy of mixing (ΔG_{mix}) of the system. This energy is evaluated by the following formula[10]:

$$\frac{\Delta G_{mix}}{RT} = \left(\Sigma x_i \ln(\gamma_i x_i)\right)_M - \phi\left(\Sigma x_i \ln(\gamma_i x_i)\right)_{LC} - (1-\phi)\left(\Sigma x_i \ln(\gamma_i x_i)\right)_{HC} \tag{1.1}$$

where R is the ideal gas constant, T is the temperature in [K] and x_i is the mole fraction of the species i in the resulting mixture (M), low concentration (LC)

and high concentration (HC) solution respectively. The symbol ϕ is the ratio of the number of moles of low concentration solution and the total number of moles in the system, whereas γ is the activity coefficient, whose value depends on the temperature, pressure and the composition of the solution[11]. When seawater (600mM of NaCl) and river water (1.5 mM of NaCl) mix together, the equation above predicts the maximum energy per unit volume of riverwater, that can be extracted is equal to 0.76 kWh/m^3.

The theoretical concept of Blue energy was introduced quite early, way back in 1954 by *R. E. Pattle*[12], who theorized the use of "stacks" made of acidic and basic membranes. Membranes were characterised as acidic or basic on the basis of the functional group which dissociates under suitable pH conditions. Commercially available acidic membranes have either carboxylic (-COO^-) or sulphite (-SO_3^-) groups, imparting a negative surface charge to the membrane, resulting to cation selectivity. Conversely, basic membranes commonly contain tertiary amines (-R_3N^+), providing the membrane with a negative surface charge, leading to anion selectivity. The space between these stacks were to be filled alternatively with salt water and fresh water. According to *Pattle*, when a volume (V) of pure solvent mixes with a saline solution of osmotic pressure π, it results to a release of free energy equal to πV, which can be harvested using traditional hydro-turbines. This source of electricity generation later saw an increased interest when *Sidney Loeb*[13] was able to experimentally demonstrate the concept of *Pressure Retarded Osmosis*. Development of polymer technologies and microfabrication techniques lead to a continued interest in developing membrane based Blue energy extraction techniques and the spike in crude oil prices in 2008 gave rise to a few commercial power-plants, aimed at extracting this untapped source of energy.

1.2 Contemporary Technologies for Blue Energy Harvesting

This section is dedicated to the description of the state-of-art technologies aimed at harvesting Blue energy in the modern age:

1.2.1 Pressure Retarded Osmosis (PRO)

Pressure Retarded Osmosis is the most widely investigated techniques of harvesting Blue energy, since the introduction of its concept in 1954[12]. This process relies on the use of a semi-permeable membrane which separates the source of pure or low salinity water (feed solution) from the high salinity (draw) solution. The draw solution is maintained at a higher pressure compared to the feed solution, but lower than the osmotic pressure required for reverse osmosis. As the chemical potential of the water molecules in the feed solution is higher than that of the draw solution, the water moves through the semi-permeable membrane, resulting to an increase in volume of the draw solution reservoir while diluting its salt concentration. This increased volume is subsequently used to drive a mechanical turbine which generates electrical power. The basic schematic of a PRO power plant was published by *Richard Norman* in 1974[14] and is given in figure 1.2. Figure 1.3 illustrates two types of PRO systems: an "open loop system" where freshwater is lost to sea after the power-generation cycle and the "closed loop system" where the freshwater/seawater mixture is distilled and reused after the power generation. The illustration was published by *Achilli and Childress*[15] in 2010.

The late 1970s saw considerable experimentation performed over the PRO setup in laboratory conditions, particularly by *G.D. Mehta* and *Loeb*[16,17,18]. This led to the successful proof-of-concept for this technology and the quantisation of the power

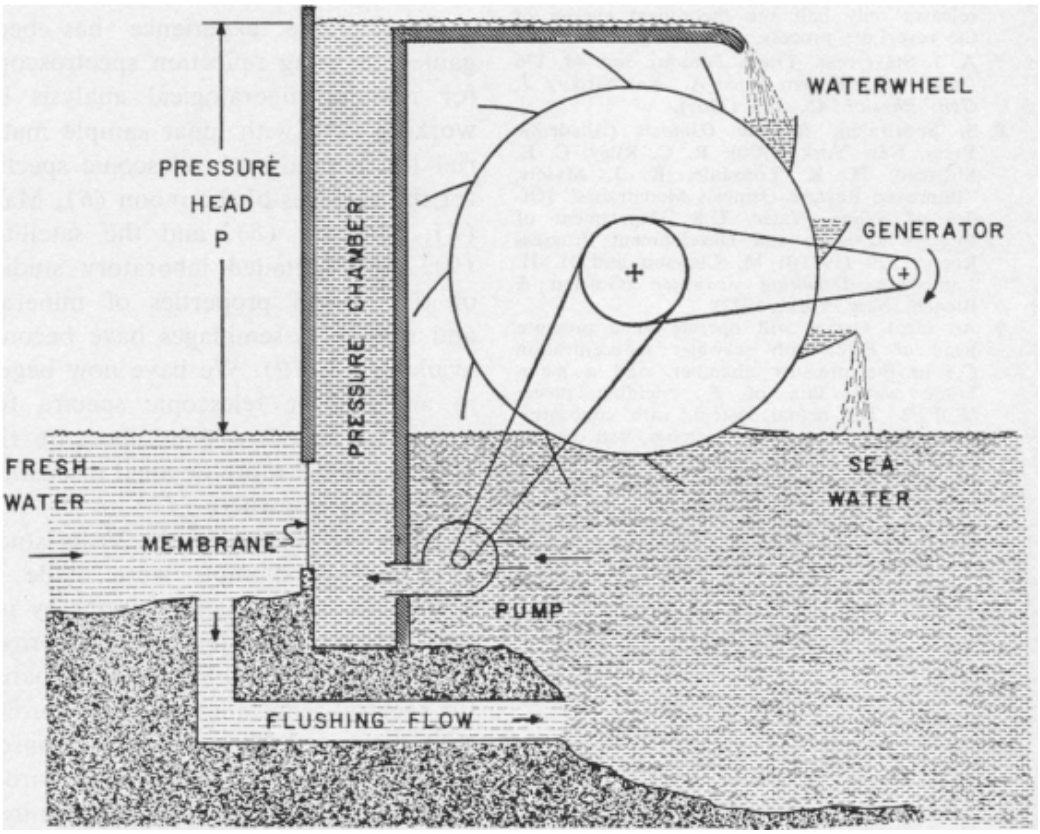

Figure 1.2: Schematic of a simple Pressure Retarded Osmosis setup. Illustration by *Richard Norman* (1974)[14].

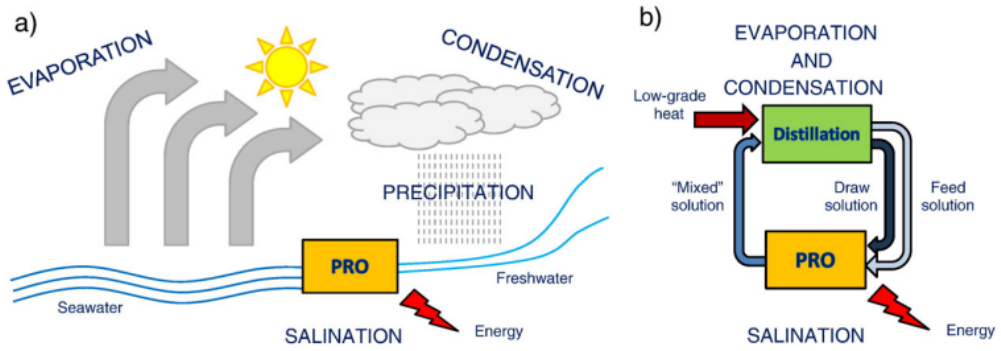

Figure 1.3: Schematic of (a) open-loop and (b) closed-loop Pressure Retarded Osmosis (PRO) setup as illustrated by *Achilli and Childress* in 2010[15]. The open loop was conceptualized initially and was followed by *Sidney Loeb* patenting the closed loop PRO in 1975[13].

that can be extracted from such power plants. The density of power expected was in the range of 1 to 3 W/m^2, which was quite low considering the osmotic pressure difference between the two sources of water used. The low power density were later associated with the effects of reduced water flux through membrane due to concentration polarization (explained later in this chapter) and the fouling of the membranes, although in the 1970s the studies on these effects were still in their infancy. Another factor impacting the low power generated from early PRO systems were the lack of membranes specifically designed for PRO applications[19], as most membranes used in 1970s and 1980s were designed for desalination of water using Reverse Osmosis.

1.2.2 Reverse Electrodialysis (RED)

Reverse Electrodialysis is the second most popular method of employing a salinity gradient to harvest energy, after Pressure Retarded Osmosis[20]. The technique is considered as the advancement of idea proposed by *R. E. Pattle* in 1954[12], who obtained a power output of 0.2 W/m^2 using a "hydroelectric pile" of alternating acidic and basic membranes through the mixing of seawater and freshwater. The studies conducted in the 1970s by two groups, *Fair and Osterle*[21] and *Weinstein and Leitz*[22], provided a breakthrough in the theoretical understanding of the RED system. In spite of the theoretical framework on RED systems being established since 1970s, the popularity of RED systems in the context of energy generation has seen a rapid rise only in the modern era, since 2007[23]. This popularity is owed to the advancement in membrane fabrication technologies and the global focus on the advancement of clean energy. The schematic of a RED setup is illustrated in fig. 1.4, published by *Logan and Elimelech*[24] in 2012. Reverse Electrodialysis uses *Ion Exchange Membranes (IEMs)* which preferentially allow either a cation or an anion, to travel across them. The membranes permeable to cations

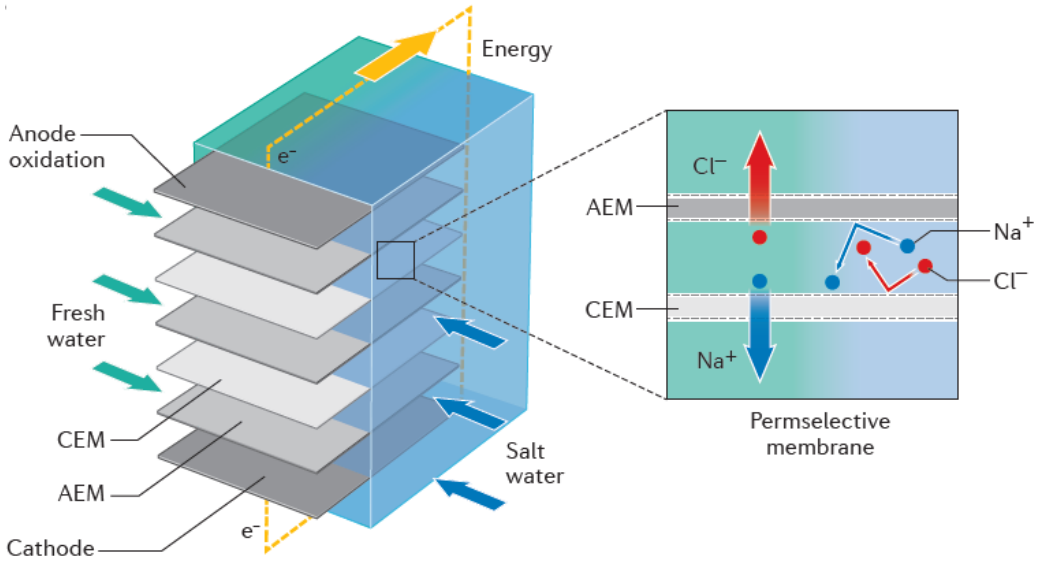

Figure 1.4: Stacked membranes for a Reverse Electrodialysis system. CEM/AEM stand for Cation/Anion Exchange Membrane respectively and the inset describes the motion of ions inside the membrane stack. Figure published by *Logan and Elimelech*[24].

are termed as *Cation Exchange Membranes (CEMs)* and similarly the ones that allow the passage of anions are called *Anion Exchange Membranes (AEMs)*. These membranes are formed into a stack with alternating CEMs and AEMs, arranged next to one another and the space between the membranes is filled with freshwater and saline water alternatively. A flux of ions through the membranes arises due to the salinity gradient of the liquids, this flux leads to the development of a potential difference across the stack, which can be used to generate current using electrodes. The electrodes also maintain electroneutrality of the system and hence through the connection to an external resistance, the circuit can be used to produce electrical energy. Unlike PRO system, this technique does not rely on movable mechanical components like turbine and hence results to low mechanical losses. The electrodes instead form the backbone of the energy generation process and hence have very specific conditions for selection, which increases its cost of

fabrication (elaborated later in this chapter).

Despite the gains obtained from the lack of mechanical components, RED systems rely heavily on the quality of the membrane and its stability. Therefore research on spacers, the porous components that support the membranes and promote mixing[25], to mitigate concentration polarization has seen a rapid rise in the previous decade[26,27,28]. *Guler et al.*[29] designed an anion exchange membrane in 2012, specifically for RED systems and demonstrated a high power density of 1.27 W/m^2.

The appeal of directly generating electricity using salinity gradient resulted in the establishment of two RED pilot plants in 2016, one in the Netherlands[30] and the other in Italy[31],which provided insight over the efficiency of this technique outside a laboratory environment. The pilot plant in Italy was also expanded one year after its installation to include three RED prototypes (initial setup consisted of one prototype), which increased the power output from $\approx$ 30W to 330W, using brine solutions and brackish water[32].

1.2.3 Capacitive Mixing

Capacitive Mixing (CapMix) is relatively a new technology compared to PRO and RED as it was discovered by *Doriano Brogioli*[33] in 2009. A simplified schematic of a CapMix setup, illustrated by *Brogioli* is given in the fig. 1.5a. This setup was later characterized as *Capacitive Double Layer Expansion (CDLE)*[33] technique as two other techniques namely, *Capacitive Donnan Potential (CDP)*[34] and *Mixing Entropy Battery (MEB)*[35] were categorized under the umbrella of extracting osmotic energy using capacitive mixing. Unlike the preceding techniques, CapMix relies on the capacitance produced by porous electrodes due to the formation of an electrical double layer. The capacitance of the cell is defined as the ratio of the

charge stored inside the capacitor to the potential difference across the it[36] *i.e.*:

$$Q = C\Delta V \qquad E = \frac{CV^2}{2} \qquad C \propto \frac{1}{d} \tag{1.2}$$

where $Q, C, \Delta V$ and E represent the charge inside the capacitor, the capacitance, the potential difference across the capacitor and the energy stored in the capacitor respectively. The symbol d represents the separation distance of charges in the capacitor, as this distance increases, the capacitance decreases.

As mentioned earlier there are three different techniques of extracting energy from a CapMix setup, described as follows:

Capacitive Double Layer Expansion (CDLE)

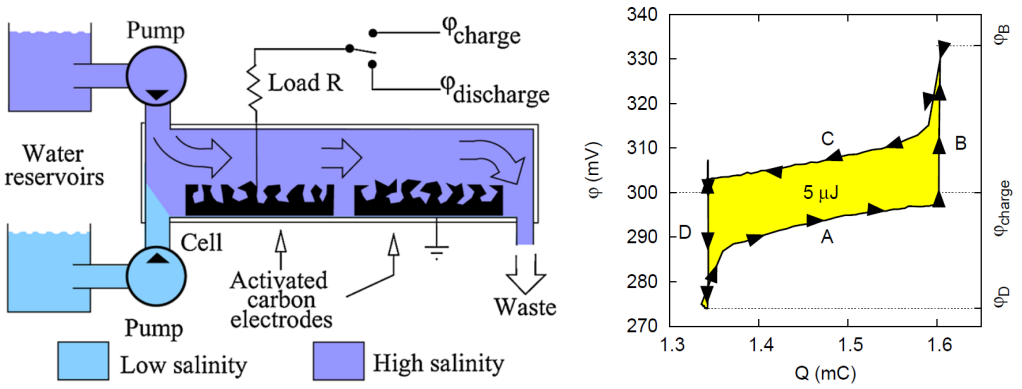

(a) (b)

Figure 1.5: (a) Schematic of a *CDLE* CapMix cell. This setup consists of a cell filled with electrolytes (freshwater, saline water) and two electrodes. The electrodes can trap charges by creating an electrical double layer around themselves. The thickness of the double layer is determined by the concentration of ions in the cell liquid. Hence changing the cell liquid changes the capacitance of the CapMix cell. (b) Plot representing the change of charge stored in the cell (Q) with respect to the potential difference (φ) across the cell. The alphabets (A, B, C and D) represent the different working phases of the CapMix cell. Both images were published by *Doriano Brogioli* in 2009[33].

This method relies on the porous activated carbon electrodes to store electrical energy in the form of a capacitive double layer, formed as a consequence of exposing ions in salt water to an electrode potential. The schematic shown in fig. 1.5a, describes the typical geometry of a CDLE cell. There are four phases in the operation of this cell:

- Phase - A (charging): In this phase, the cell is first filled with salt water and the electrodes are charged from its base potential φ_D to its charged potential φ_{charge} (fig. 1.5b), using an external source. As the potential increases inside the cell, the energy stored inside it increases (eq. 1.2), "charging" the capacitor.

- Phase - B (constant charge): Following the charging phase, the circuit is disconnected from the external potential and the fluid inside the cell is replace with freshwater. As the circuit is open, the charge inside the circuit is conserved while the separation of charges in the electrode double layer (d) increases, thereby increasing the potential across the capacitor to φ_B (eq. 1.2, fig. 1.5b). The increase in the double layer thickness is attributed to the low concentration of ions in freshwater compared to the saline water resulting to an increase of Debye length[37].

- Phase - C (energy extraction): Once the fluid in the cell is exchanged, the circuit is closed using an external resistance (load). As a result, the cell is discharged and creating a flow of current in the circuit. The capacitance of the cell remains constant in this phase, resulting to a drop of potential from φ_B to φ_{charge} (fig. 1.5b). There is a positive net gain in the capacitor as the change of liquid in the cell results to the generation of electrical energy higher than the input energy required for the capacitors initial charge phase.

- Phase - D: The final phase of the CDLE requires the circuit to be open, fol-

lowed by flushing the freshwater and replacing the cell liquid with saline water. This returns the circuit to its initial condition by dropping the potential across the system to φ_D as the charge remains constant, eventually resulting to a decrease in capacitance.

Capacitive Donnan Potential (CDP)

This technique utilizes ion selective membranes (*CEMs* and *AEMs*) inside the CapMix cell, to generate electricity without requiring an external source of potential. First introduced by *Sales et al.*[34] in 2010, this technique relies on the build-up of Donnan Potential which develops as a result of using IEMs inside the CapMix cell, in front of the porous electrodes. The operation mechanism of the CDP cell is identical to the working of a CDLE setup, with the exception that electrical current can be extracted from a CDP cell twice (Phase - 1 and 4 in fig. 1.6), with reversed polarity of electron flow. When saline water is introduced in the cell, the ions present in the solution are segregated due to absorption of the ion exchange membranes. This separation of ions leads to the development of membrane potential, which is recorded as the first voltage peak in the left bottom plot of fig. 1.6. This potential is nullified due to the development of an electrostatic double layer in the solution. When the saline water is flushed and replaced with fresh water, the double layer gets altered and results to the development of a reverse potential as the ions absorbed by the membrane, travel back to the spacer due to a diffusive flux. This flux results to establishment of a reverse voltage, indicated by the second voltage peak in the left bottom plot of fig. 1.6, completing the power generation cycle.

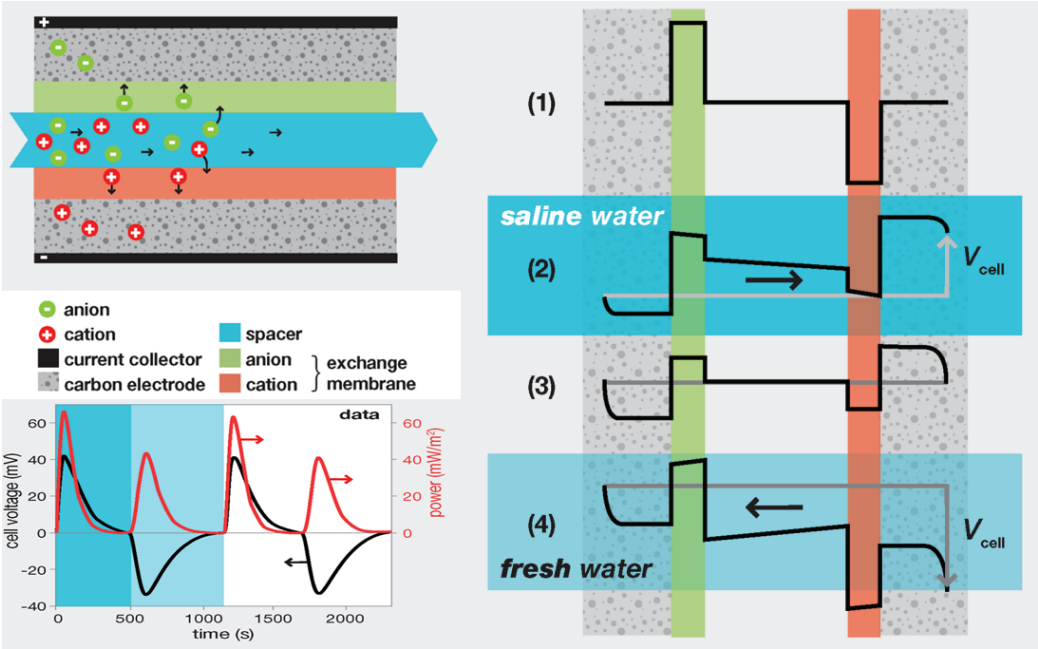

Figure 1.6: (Left Top) Schematic of a *CDP*-CapMix cell. This cell consists of two distinct Ion Exchange Membranes on either side of the *spacer*, where the flow of water is observed. As saline water flows through the cell, the anions travel upwards toward the positive electrode where they are absorbed, whereas the cation moves in the opposite direction. This separation of charges produces a potential (Left bottom) Plot representing the change of voltage (black lines) and extractable power (red lines) in the cell with respect to time. (Right) Change of potential across each membrane, during the four operating cycles. The figure was originally published by *Sales et al.*[34].

CapMix Hybrids

In the recent times, a few variants of CapMix developed and tested in laboratory conditions have shown promising results and are on the road to be developed into a functioning technique of extracting osmotic energy. Most notable amongst them is called *Mixing Entropy Battery (MEB)* developed by *La Mantia et al.* in 2011[35]. The MEB is an electrochemical cell which extracts energy from the difference of salinity gradient from two solutions and stores it as chemical energy inside the electrode material's bulk crystal structure. This technique is also termed as *Battery*

Mixing (BattMix) and it employs the use of faradaic electrodes to convert the chemical energy to electrical current[38,39]. *La Mantia et al.* initially demonstrated the MEB setup using $MnO_2|Na_2Mn_5O_{10}$ and Ag|AgCl as cathodic and anodic electrodes respectively with a NaCl electrolyte. The energy generation cycle for the MEB cell along with the illustration of the battery voltage (ΔE) and charge (q) is provided in the figure 1.7, as published in the original publication[35]. MEB takes advantage of the specific interaction of its electrodes when immersed in low salinity NaCl solution. This results to the removal of Na^+ and Cl^- ions from the electrodes, charging the cell. When the solution inside the cell is exchanged with high concentration sea water, the potential difference between the electrode increases. The last step of the process involves the discharging of the cell, utilizing the increased potential difference and incorporating the Na^+ and Cl^- ions back into the respective electrodes.

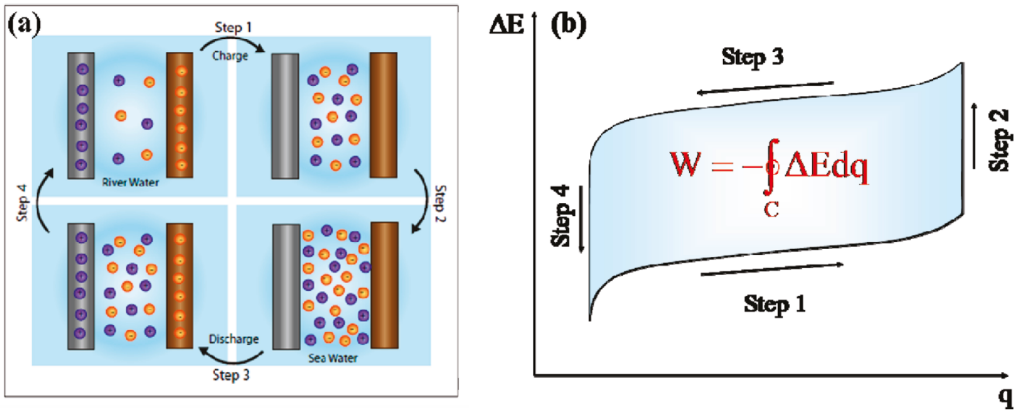

Figure 1.7: (a) Working principle of a Mixing Entropy Battery and (b) Battery cell voltage (ΔE) and charge (q) during the energy generation cycle. Originally published by *La Mantia et al.*[35].

The second technique which has been gaining traction lately in the CapMix hybrid systems involves the use of a single selective membrane and two capacitive layers which adsorb ions inside a CDLE cell. This technique, a combination of

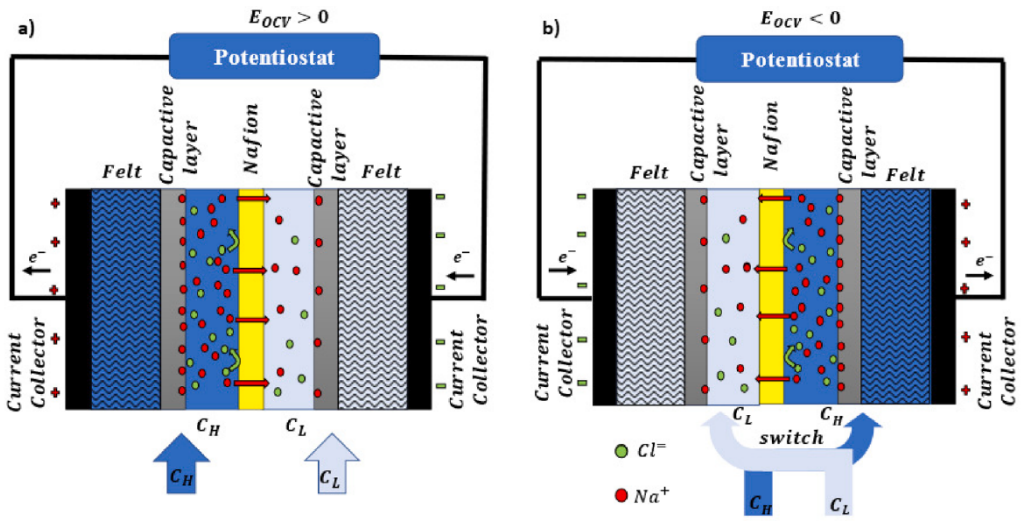

Figure 1.8: Working schematic of CDLE hybrid, as published by *Brahmi and Colin*[40].

a RED-CapMix setup (CRED), demonstrated by *Y. Brahmi and A. Colin* in the beginning of 2022[40], is capable of producing a net power density of 2 W.m^{-2}, which is significantly higher than the rest of the Blue energy extraction techniques demonstrated to date. The working schematic of this technique is illustrated in fig. 1.8 and consists of a cation selective Nafion membrane that separates the high ion concentration solution from the other. Two capacitive layers enclose the solutions into their respective compartments and are capable of holding charge due to the adsorption of cations on their surface. At a given moment, both the compartments contain liquids with different concentrations. The liquids in the compartments are alternated (*i.e.* compartment holding fresh water is flushed and filled with saline water and vice versa) twice during the energy generation cycle. When liquids are allowed to interact, the cations migrate toward the region of low salinity through the nafion membrane, leading to the development of a potential difference. This potential difference creates a flux of electrons that move through the circuit, creating an electronic capacitive current. This current eventually stops when the potential difference across the current collectors balance the sum of the potential

differences at the membrane boundaries and at the boundaries of the capacitive electrodes[40]. Hence the flow of electrons is a result of the membrane potential and of the capacitive electrodes put together. This additional potential due to the capacitive electrodes makes this technology quite attractive in terms of the open circuit voltage as it is accounted to be nearly double for low salinity solutions and five times as much for high salinity solutions. The resulting high density of net power is a consequence of the intuitive concept of using the membrane potential in addition to the capacitive electrodes previously employed in CDLE technique. Authors of this paper demonstrated the high power output of this setup through direct measurements on a load resistor, contrary to most laboratory experiments where the power output is derived through membrane characteristics. The power output obtained is significantly higher than any of CDLE and RED membranes in use. Furthermore, theoretical findings by *Janssen et al.*[41] suggests that this power output be doubled by using warm (waste-heated) freshwater source instead of room temperature water for mixing, making this an interesting new avenue for research.

1.2.4 Membrane-free Processes for Blue Energy Harvesting

The inherent problems associated with the fabrication, fouling and polarization of membranes tempted research toward developing techniques to harvest blue energy without the use of membranes. Albeit the lack of literature and the low power outputs, it is important to list the following two methods due to their innovation in trying to provide a paradigm shift to their existing counterparts.

Hydrogel Swelling

Hydrogels are a three dimensional long polymer chains that have the ability to trap large volumes of water withing them due to the presence of hydrophilic groups on

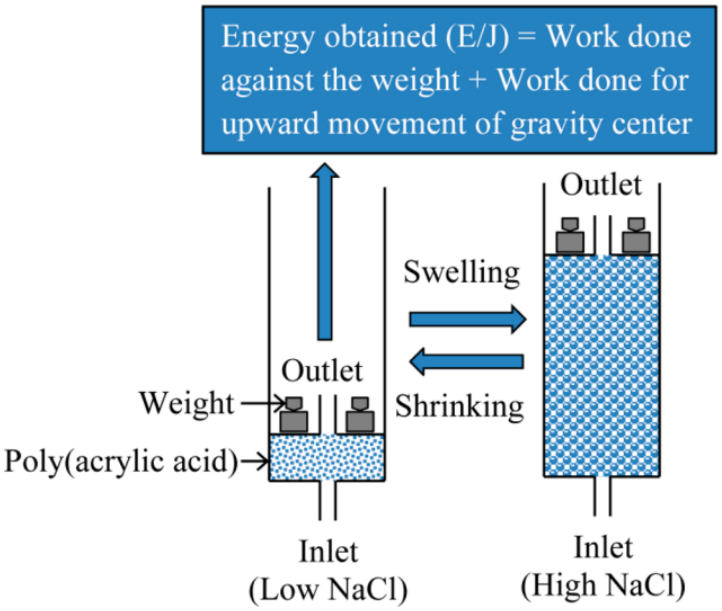

Figure 1.9: Osmotic energy recovery using Hydrogels. Originally published by *Zhu et al.* in 2014[42]. The terms "Shrinking" and "Swelling" are in reference to the reservoir (piston) volume and not to be confused with that of hydrogel shrinking and swelling as it is in the opposite direction.

their surface[43]. When these materials are submerged in freshwater, they swell due to water intake owing to the osmotic pressure and the ability of the carboxylic groups on their surface to form hydrogen bonds with the water molecules[44]. In a similar process, the hydrogel infused with freshwater will expel its water content when exposed to a saline solution as the osmotic pressure difference between the freshwater inside the gel and the outside environment is high and the hydrogen bonds holding the water is broken due to the charge neutralization of the polymer surface. In 2014, *Zhu et al.*[42] designed a piston-type process using poly(acrylic acid) hydrogels which would could be used to produce mechanical work. In this approach, the group alternated the exposure of the hydrogels to solutions of high and low salt concentrations. Schematic of the setup is given in fig. 1.9 as published by *Zhu et al.*[42], shows a piston setup loaded with weights. As the hydrogels

are immersed in fresh water, they expand taking in the water from the piston and as a result the piston moves downwards. The solution in the piston is then switched to saline water, which makes the hydrogels release the water stored inside them, which increases the volume of liquid inside the piston and the piston moves upwards. Hence the salinity difference between two sources of water can be used to produce mechanical work by adding weights on top of the piston. When the load due to the weights is less than the swelling pressure, the shrinking of the gels results to an expansion of reservoir volume, which can act against the applied external load, producing mechanical work. Hence the shrinking and the expansion of the gels can be used cyclically by alternating the salt and the freshwater exposed to the hydrogels, resulting to extraction of osmotic energy. As it is hard to define a surface area for the hydrogel particles, the power output of this method cannot be compared directly with membrane based techniques however the method resulted to a very low energy efficiency of 0.34% which was attributed to energy wasted due to mixing of solutions and to the separation distance between hydrogel particles in solution.

Vapor Pressure Differences

This method was introduced by *Olsson et al.* in 1979[45] and it aimed to use the low vapor pressure of saline water compared to fresh water, to drive a turbine which in-turn generated electricity. The setup consisted of two hollow Aluminum cylinders containing fresh and saline water. The reservoir were kept under vacuum and allowed to evaporate without allowing to mix with one another. The flow rate of vapors and the vapor pressure difference were regulated using a control valve and once sufficient pressure was built between the two reservoirs, the flow of the vapors would be used to run a turbine connected to an electrical generator. The authors reported a maximum power output 7 W/m^2 with an efficiency of 40%,

when operating at a temperature of 40°C, when using freshwater and brine as the interacting solutions.

1.3 Viability and Economic Analyses of Blue Energy Harvesting

It was stated in the beginning of this manuscript that the mixing of sea water with rivers results to a release of mixing energy, equal to 0.76 kWh/m^3 per unit volume of river water. On closer examination at eq. 1.1 is it noticeable that this estimate is only true for the case when an infinite amount of seawater mixes with the river water, resulting to $\phi = 0$ and it decreases monotonously with the increase of the quantity ϕ, essentially reducing the maximum obtainable energy to 0.44 kWh/m^3. It is also evident from eq. 1.1 that higher the contrast between the salt concentrations in the two solutions, higher the mixing energy available for extraction. Hence, when considering the viability of salinity gradient technologies for sustainable energy, it is important to discuss the context of the using solutions other than just sea and river water. Many industries producing high concentration brines as waste, can in theory, utilize Blue Energy harvesting to further improve their energy efficiency. Figure 1.10a illustrates the free energy of mixing that can be extracted (shaded region) and the theoretical maximum energy that is generated due to the mixing of solutions of different salinity gradient (taken from *Yip et al.*[10]). Hence the utilization of osmotic energy is not limited to generating electricity for general use but also has a significant role in the making existing technologies more efficient.

When proposing an alternative to fossil fuels and other renewable sources of energy, the fundamental focus of Blue Energy harvesting comes down to the afford-

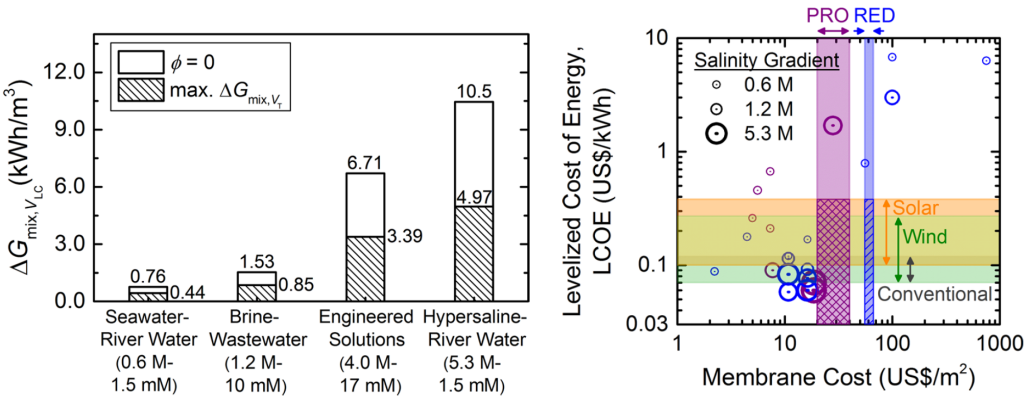

(a) (b)

Figure 1.10: (a) Free energy of mixing per unit volume of low concentration solution for different salinity gradients. The shaded region corresponds to the attainable energy and the clear bar indicate the theoretical maximum. (b) Levelized Cost of Energy (LCOE) as a function of membrane price. Violet and blue circles represent PRO and RED respectively. The size of circles indicates the salinity gradient. The vertical bands indicate the installation cost of PRO and RED membranes stacks. The figures were first published by *Yip et al.*[10] in 2016.

ability of this technology in comparison with the rest. Given that this source of energy is relatively unpopular and operates in only a handful of pilot plants exclusively for PRO and RED, it is unwise to include operational costs of other Blue energy technologies to compare with the current energy market. The comparison of the Levelized Cost of Energy (LCOE) for PRO and RED with the others is illustrated in fig. 1.10b. It is clear from this figure, that higher the cost of the membrane used, lower the concentration of salts required for energy production. In other words, depending on the available source of saline and freshwater, the investment required to install a membrane plant can be greatly reduced. The circles on the right of the dashed bands in fig. 1.10b represent the regions where Blue energy technologies can compete with the other energy production techniques. Hence in areas such as the Dead Sea, where saline water is readily available, blue energy technology can be a viable replacement for energy production. The circles

on the right of the shaded region in fig. 1.10b, convey the opposite message. The lack of natural sources of salt will necessitate high selectivity membranes which come with high investment cost. Moreover, given the propensity of membrane fouling and pre-treatment required, the efficiency of the plant will further drop, rendering it unfeasible. However, the potential for Blue energy technology to be a significant contributor to global energy demand is important. Advancements in material and manufacturing techniques and development of novel methods to address the shortcomings of PRO and RED can result to a development of a robust and sustainable source of energy.

1.4 From Individual Nanopore to Massive Parallelisation: Promises and Bottlenecks

Based on the available literature and the established infrastructure it can be said that Pressure Retarded Osmosis and Reverse Electrodialysis have been the most advanced technologies for harvesting Blue Energy to date. These were among the most notable methods and their popularity resulted to establishment of industrial scale plants in the Netherlands[30,46] and Italy[31]. The establishment of the large scale power-plants resulted in the identification of inherent limitations in the membrane-based approaches toward extraction of Blue energy, mostly notably *Internal Concentration Polarization*, along with a few technique specific issues, detailed as follows:

- **Membrane fouling and pre-treatment**: Due to the high reliance of PRO and RED on the efficiency, stability and the permselectivity of membranes, any impurities in either the draw or the feed solutions would result to a reduction of the water flux through the membrane. The small pore sizes

associated with membranes makes it prone to the effects of fouling, as any impurities in the input solution such as clay particles or biological pollutants can block the passage of ions through it[47]. This necessitates the use of pre-filtration of the input solutions before they are used for power generation and as the pre-filtration techniques are energy consuming themselves, it reduces the net gain of energy from the system, making the operation non-viable for energy extraction from mixing of sea water and river water[48].

- **High operating pressures of PRO systems**: The draw solution in the PRO system needs to be maintained at constant high pressure that is close to, but not greater than, the osmotic pressure of the feed solution. Maintaining this high pressure expends hydrodynamic energy and hence a net gain in energy from PRO is only possible when the draw solutions are limited to hypersaline solutions. The increase in the osmotic flux due to high salinity gradient in case of hypersaline draw solutions can offset the requirement of the hydrodynamic energy[49] at the cost of limited application dependent on the availability of hypersaline water sources.

- **Effect of multivalent ions RED stacks**: Due to the specificity of the membranes used in RED stacks, the ions in the saline source of are required to be monovalent. This is due to the studies done by *Post et al.*[50] which suggest that the use of multivalent ion sources in feed water results to an increased resistance of the membrane, effectively halving the stack efficiency[51].

- **Lack of electrochemical couples for RED**: As mentioned earlier, the electrodes are paramount in the determination of the energy efficiency of RED systems. Despite its importance, the research on electrode materials for RED is quite limited. An efficient electrochemical couple for RED is characterized by the following properties as mentioned by *Scialdone et al.*[52] in

2012: low voltage drop at electrode-solution interface, low cost of fabrication, high solubility of redox couple, chemical and electrochemical stability of redox species along with physical stability of the electrodes. These constraints limit the electrode couple to mainly one candidate that is $FeCl_3$/$FeCl_2$ which demonstrated high stability under RED operative conditions[52]. Hence the lack of diversity in the electrode materials is a major bottlenecks in RED technology.

- **Effect of temperature on feed solutions**: When using natural sources of water as a feed solution, one needs to be aware of the temperature fluctuations that occur due to natural climatic conditions. The work done by *E. Brauns*[53] in 2009 clearly states that the water sources with high temperatures like solar heated desalination brines, are more beneficial in achieving higher power densities through RED. Hence it is expected that the energy generation during the cold winter months will be affected by low power output of the plant. This is especially troubling since the demand for power is at its peak during the winter months due to heating requirements.

- **High cost of up-scaling RED pilot plants**: Typically a RED membrane pair produces a voltage of 0.2V, therefore to counteract the energy losses at the electrodes, a RED plant requires at least 20 pairs of membranes[24] to achieve a net positive in the energy generated, without considering the need for pre-treatment and cleaning. As the surface area of the membranes are increased, these losses can proportionally increase therefore scaling-up of the plant requires an intricate control over various parameters including the geometry of the stack. The second challenge in scaling up of RED plants to fully commercial power plants is the high cost of IEMs, and its sensitivity to the quality of the feed solution. Hence the bottleneck in RED technology lies in the demand for robust, low-cost membranes although their

global demand may result in a drastic reduction of the cost of membrane production[54].

- **Internal Concentration Polarization (ICP)**: Polarization concentration due to accumulation or depletion layer formation as illustrated in Fig. 1.11(a) is a recurrent issue in membrane science. Internal Concentration Polarization has been identified as the major bottleneck in the expansion of membrane based approaches to harvest energy from salinity gradients as illustrated in Fig. 1.11(b). The adverse effect of concentration polarization on membranes was first published by *Lee et al.* in 1981[55]. This effect is predominant in the vicinity of the membrane that separates the feed solution from the draw solution and has a significant effect to the detriment of system efficiency. When a flux of ions travels through the membrane, the concentration of the high salinity (draw) solution drops considerably at the interface between draw solution and the membrane. A reverse effect is seen on the other side of the membrane interface, where the concentration low salinity (feed) solution increases due to the ion-flux. This leads to the development of a boundary layer in the neighbourhood of the membrane resulting to a reduction in the membrane potential. As a result, the driving force responsible for the ion flux through the membrane is greatly diminished leading to reduced efficiency of the membrane. This effect is inherent to all membrane based processes and can only be rectified by spending energy to ensure mixing[55], which further reduces the net energy gained from the system.

All these factors inspired research focusing at the dynamics of ions and fluids inside a single nanopore and use that knowledge to develop a new paradigm in the harvesting of Blue Energy.

Looking at the limitations resulting to low conversion efficiency of the techniques,

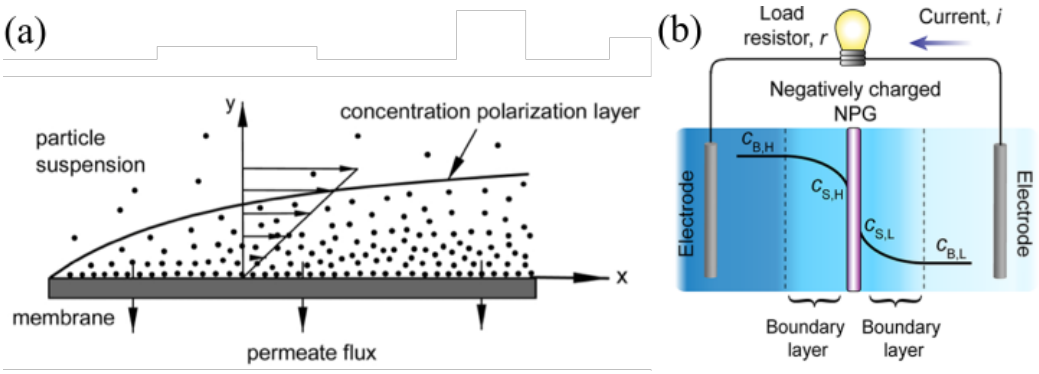

Figure 1.11: (a) Schematic of concentration polarization in membrane science taken from *Chen et al.*[56], (b) Concentration polarization at a membrane - solution interface in the framework of a RED process taken from *Wang et al.*[57].

it is evident that there are problems endemic to the use of membranes. As an attempt to improve conversion performances, researchers aimed at identifying optimal conditions for fluid confinement. Therefore, individual nanopores appeared as ideal elementary unit to probe the dynamics of confined ions and fluids and use that knowledge to develop a new paradigm in the harvesting of Blue Energy.

Electricity generation using nanopores is not a novel idea considering that in biological systems, it is a quite common phenomenon. The neurons inside human brain is the most common example of such a system. The electrical signals or *Synapses*, inside the human brain, responsible for the communication and coordination of metabolic activities, are produced as a result of ion-selective Potassium (K^+) or Sodium (Na^+) nanochannels which are activated by either external stimuli or change in the potentials inside the cell[58]. Another example of a biological process resulting to the production of electricity is the Electric Eel, whose electric organ is capable of generating potentials as high as 600 V using a highly selective ion-channels made out of protein chains, harnessing biological concentration gradients[59]. Researchers in the United States started with a theoretical framework to mimic these biological processes of energy conversion in 2008[60] and the ex-

perimental realization of an reverse electrodialysis setup using a single solid-state nanopore followed soon after[61]. The work of *Guo et al.*[61] highlighted the immense potential of nanopore based power generation as they predicted a power output three magnitude higher than any other ion-exchange membrane, once parallelized. Nanopore based energy generation is still in its infancy when compared to conventional membrane based power generation technologies and therefore results of the experiments, performed usually in controlled laboratory environments, are theoretical extrapolations usually assuming a certain porosity of a nanopore array. The fabrication of such arrays may still present some technical difficulties to realize, which are not considered for studies demonstrating a proof of concept. Hence, the ultrahigh powers resulting from these studies are to be considered as a theoretical maximum rather than a certainty.

Nanopore based materials achieved a breakthrough in energy generation when *Siria et al.* demonstrated a record high power density of 4000 W/m^2 in 2013 using a single transmembrane Boron Nitride Nanotube (BNNT)[62]. The group demonstrated a device comprised of a single nanotube 15-40 nm in diameter and a length of 1μm which separated two reservoirs of Potassium Chloride (KCl) solutions of distinct concentrations. The high density of power obtained in the device was attributed to the large surface charge density which was found to be around 1 C/m^2, using independent surface conductance measurements at low salt concentration with an alkaline pH environment. This surface charge is the main factor controlling the formation of electrical double layer inside the nanopore and the thickness of this double layer varies as a function of the salinity of the solution. Hence, as the nanopore connects the two reservoirs, the width of the double layer changes and induces a longitudinal pressure gradient at the vicinity of the wall which is responsible of the so called diffusio-osmotic flow.

This diffusio-osmotic flow promotes charge transport and produces an electrical

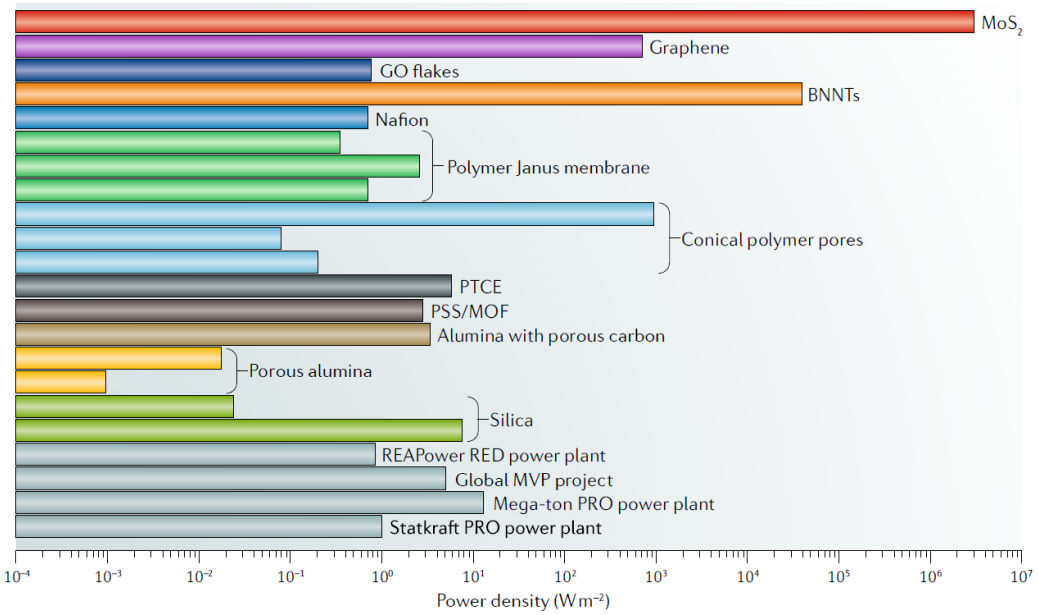

Figure 1.12: Power densities of various membrane or nanopore based technologies used for harvesting Blue Energy. Originally published by *Macha et al.* in 2019[63].

current which increases with the surface charge of the pore. The diffusio-osmotic flow is also found to be responsible for the water permeation through the nanotube and in theory, can aide in the elimination of concentration polarization in small reservoirs. Further research on the physical characteristics of nanopores led to experiments made of monolayers or few atomically thin layers of materials, in an attempt to reduce the length of pore (membrane thickness). In 2016 *Feng et al.* demonstrated a mammoth power density of 10^6 W/m^2 using a three-atom thick sheet of Molybdenum disulphide (MoS_2) with a pore diameter of 10 nms[64], along with demonstrating the effect of membrane thickness on the generated power using molecular dynamics simulations. Subsequently, other candidates of 2D materials that were studied included Graphene (producing 700 W/m^2[65]) and monolayer of Boron Nitride (BN), which resulted to a similar power density to that of Graphene[66]. Figure 1.12 gives an overview of the several technologies

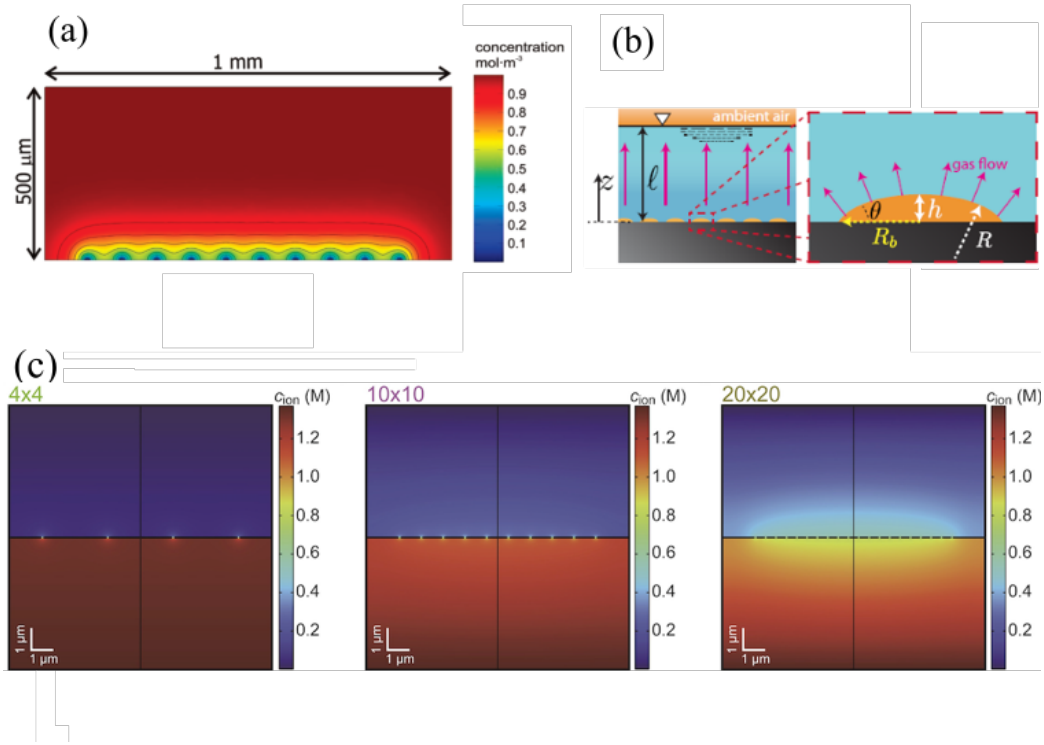

Figure 1.13: (a) Diffusive Boundary layer formation in an array of microelectrodes, taken from *Godino et al.*[67], (b) Schematic of critical lengths responsible for increased lifetimes of surface nanobubbles, taken from *Weijs et al.*[68]. (c) Diffusive Boundary layer formation in an array of nanopores, taken from *Tsutsui et al.*[69].

used for harvesting energy from salinity gradient along with their maximum generated/extrapolated power densities, taken from the work of *Macha et al.*[63]. The high powers from the nanopores shown in fig. 1.12 are not to be confused with their real potential as parallelization generally enhances the concentration polarization effect.

The most interesting aspect of concentration polarization is the fact that it arises only in multi-pore systems like membranes whereas individual nanopores have shown the ability to generate ultra-high powers from salinity gradients. Therefore any attempt at parallelization of nanopores needs to overcome this issue to suc-

ceed. The study of the boundary layer development leading to concentration polarization can be considered analogous to effects observed during the modelling of several diffusion based processes. Two such processes with characteristics similar to concentration polarization are observed in diffusion-domain approach in modelling nanoelectrodes[67] and stability of surface nanobubbles[68]. Fig. 1.13 provides a good basis to understand this analogy. Fig. 1.13(a) shows the development of depletion region near an array of individual electrodes, that reduces to a 1D diffusion layer. Fig. 1.13(b) illustrates the case of surface nanobubbles the long lifespan of which is explainable by the limited 1D diffusion of gas due to the proximity of individual bubbles. *Weijs and Lohse*[68] stipulated that this critical length is equal to the thickness of liquid (l) above the bubble arrays in case of surface bubbles and conversely, equal to bubble radius R_b for bulk nanobubbles. In case of ICP, the critical length responsible for boundary layer development in membranes is the length of reservoir feeding the membrane, whereas in case of a single nanopore it is the critical radius of the nanopore that limits this effect. In a similar manner a 1D concentration polarization layer appears with nanopores when increasing their spatial density as shown in Fig. 1.13(c).

1.5 Scope of this Manuscript

This manuscript furthers the concept of harvesting Blue energy using solid-state nanoslits organized around an architectured multi-scale flow, so as to minimize concentration polarization effects. This architecture is based on the parallelization of individual bricks named *Elemental Nanofluidic Exchanger*. This solid-state device combines the technological advances in the field of microfabrication of Silicon wafers and the existing literature on using nanoscale fluid dynamics to circumvent the issues which have been proved to be a bottleneck in membrane

based osmotic energy conversion. The active region of the elemental exchanger consists of two microtrenches of square cross-section, etched on the surface of a Silicon wafer. The two microtrenches run parallel to one another lengthwise and are separated by a thin nanoslit of a rectangular cross section. The nanoslit is made to be charge selective and serves as an equivalent of a solid state nanopore. The top surface of the Silicon wafer is then closed with a silicon cap using Direct Bonding technique, forming a Silicon-based microchip to be used for osmotic energy harvesting. This microchip, once parallelized, has the potential to extract the high energy generation capacity characteristic to a nanopore while minimizing the losses of concentration polarization. The manuscript focuses on the theoretical analyses of the dynamics of fluids at the nanometer scale, which is essential to describe and ascertain the parameters significant to such a system and also proposes a fabrication protocol for the realization of the device achievable using the available Silicon fabrication technologies. The manuscript consists of five chapters, including the introduction and has the following layout:

- **Chapter 2** introduces the concept of the Elemental Exchanger and focuses on understanding the essential parameters which describes the dynamics of ions within the exchanger. We work under the assumption that the flux through the nanoslit is directly proportional to the gradient of concentration across it and ignore the effects of diffusio-osmotic flow within the nanochannel. The goal of this chapter is to ascertain the role of three parameters *viz.* Peclét number (Pe), Sherwood number (Sh) and geometrical conductance ratio of the exchanger (J) in describing the state of the elemental exchanger.

- **Chapter 3** focuses completely on non-linear dynamics inside the nanochannel and we solve the Poisson - Nernst - Planck equation within the context of the exchanger, to arrive at the expression for the true nanochannel flux

traversing through the channel. Additionally, the effects of changing the parameters are analyzed and the condition of maximizing the selectivity whilst maintaining high ion flux through the channel is ascertained.

- **Chapter 4** combines the dynamics of fluids in the microscale with that of the non-linear dynamics at the nanoscale to develop a robust model associated with the working of the elemental exchanger. We use *COMSOL Multiphysics* software to model the continuum dynamics of ions inside the exchanger and quantify the power density that can be achieved using such system. We use *COMSOL* as it provides a convenient environment to perform finite element analysis along with providing the user with the ability to build on an existing model with additional physics, to eliminate approximations.

- **Chapter 5** is concerned with the fabrication protocol for the realization of the elemental exchanger along with the architecture for the parallelized Multiscale Exchanger. The various constraints associated with the fabrication and up-scaling of the exchanger are described here in detail. Lastly, we describe the maximum density of power that can be obtained from the device, culminating all the analyses described in the manuscript.

CHAPTER 2

A Multi-scale Flow Device for Harvesting Saline Gradient Energy

2.1 A Solid-State exchanger

The previous chapter outlined the advancements in the field of harvesting energy from salinity gradients and outlined the shortcomings inherent to membranes along with the untapped potential of individual nanopores to generate very high power densities from salinity gradients. As explained by *Wang et al.*[57], ultrahigh powers from salinity gradient can be generated from a single nanopore but any attempt at parallelization of this energy generation process leads to a buildup of a boundary layer inside the reservoirs, which is tremendously detrimental to the output energy generated by the device.

The remainder of this manuscript will focus on developing a design for a *Solid-state Exchanger* that aims to maximize the power generation capabilities of the nanopores, by using solid-state nanoslits organized around a multi-scale flow architecture, to circumvent concentration polarization effects. This solid-state exchanger is designed as a 2D array of microchannels separated by nanoslits running along their length, in between the microchannels. The microchannels will be circulated with two electrolytes of distinct concentrations alternatively, thereby exposing the nanoslits to a salinity gradient across its width. The circulation of fluids in the microchannel is carried out using a multi-scale architecture of *mesochannels* connected to microchannels using several feeding ports located at the bottom of

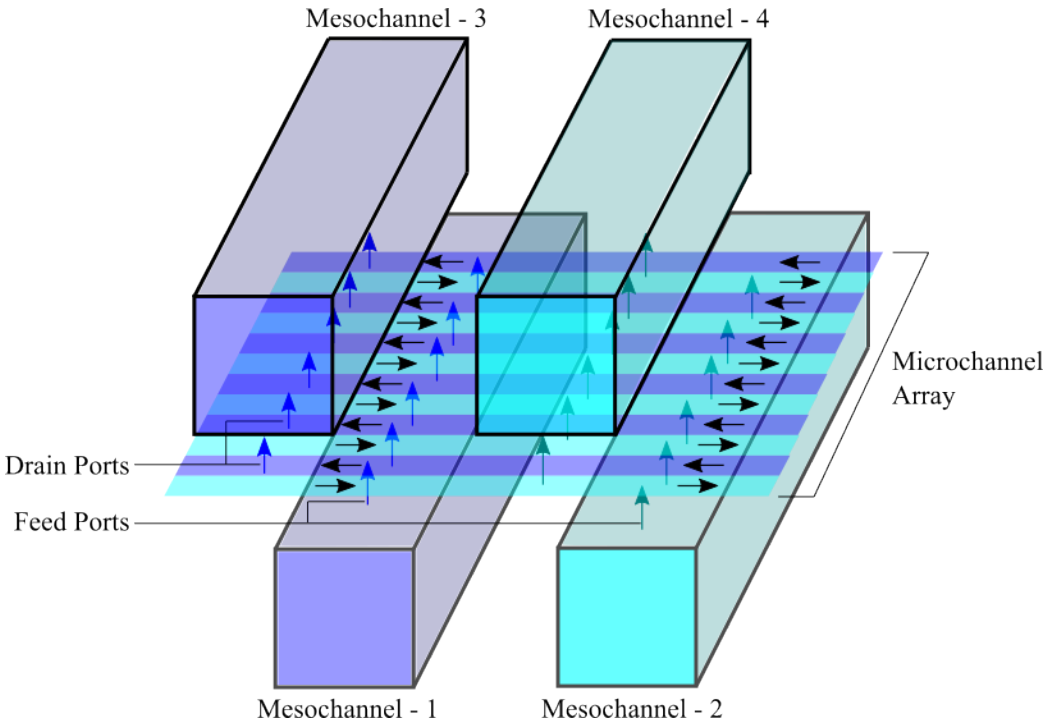

Figure 2.1: Feeding mechanism in the Solid-state exchanger. The mesochannels are used to feed/drain liquids in the microchannels and an individual mesochannel is capable of feeding numerous microchannels due to its larger size.

the exchanger. These mesochannels are aligned perpendicular to the microchannels, on a plane at the bottom/top of the microchannels. The cross-sectional areas and the lengths of the mesochannels are approximately a magnitude larger than that of microchannels, hence one mesochannel is capable of feeding numerous microchannels. As a result, the plane of feeding and draining the microchannels is separated from the region of ion-exchange, which facilitates the potential for parallelization of nanoslits. A schematic of the feeding system in the solid-state exchanger is given in fig. 2.1. The motivation of the feeding architecture is derived from the circulatory system in human beings. The hydrodynamic losses associated with providing fluid flow in minute geometries with a step-wise reduction in length scales are much lower compared to direct feeding from bulk to the nanoscale.

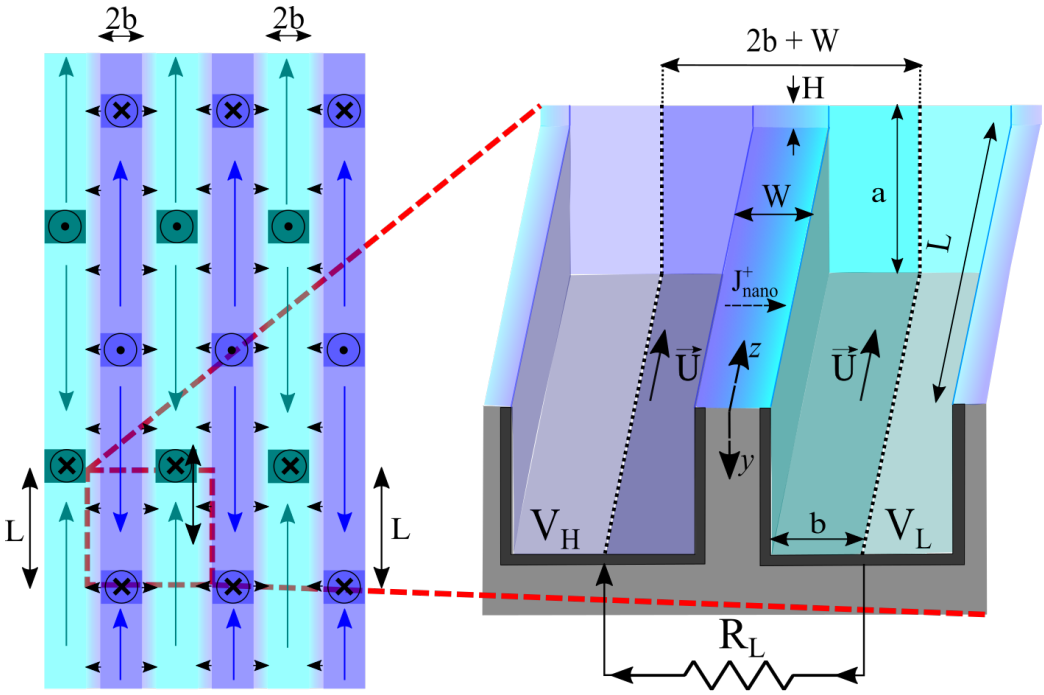

Figure 2.2: (Left) Top view of the Solid-state exchanger. Microchannels carrying high (purple) and low (blue) concentration liquids separated by a cation selective nanoslit. Microchannels have width $2b$ and depth a. The feed ports (box with solid circles) and the drain ports (box with crosses) circulate fluids inside the microchannels from the bottom of the exchanger. The blue and purple arrows indicate the convection velocity of respective microchannel liquids and the black arrows represent the salinity gradient flux. (Right) Isometric view of the Elemental Nanofluidic exchanger, defined in between the two black dashed lines. The width of each microchannel within the Elemental exchanger is b while the rest of the parameters remain the same as with the Solid-state exchanger. The microchannel liquids in the Elemental exchanger are assumed to undergo co-flow with velocity $\vec{U}$, along the length L of the channels and electrodes (dark grey microchannel faces) maintain constant potentials, V_H, V_L, corresponding to potential in the high and low concentration microchannels respectively. J^+_{nano} is the cation flux per unit nanoslit length and R_L is the load resistance.

The intention behind this design is to be able to limit the volume around the nanoslits and minimize concentration polarization in the microchannels. In other words, we constrain the size of boundary layer using a microchannel with a lim-

ited width. We replenish ions inside the microchannels by exposing the fluids to a pressure gradient (ΔP) along the microchannel length, which imposes a convection velocity ($\vec{U}$) on the fluids, leading to continuous feeding.

The microchannels and nanoslits will be carved on the surface of a Silicon substrate. The present developments in the Silicon fabrication industry enables the nanoslit height (H) to be tuned up to a minimum of 1 nm using e-beam lithography technique[70,71] and a width (W) down to 20 nm[72,73]. The microchannel depth (a) and the width ($2b$) can also be minimized (down to 500 nms) but have limitations relating to fabrication constraints, explained in Chapter - 5 of this manuscript. The nanoslit is functionalized to be selective to cations through the adsorption of polyelectrolytes as demonstrated by *Ko et al.*[74] or by electro-deposition of compounds with negative surface charge like Boron Nitride[75]. The low height of the nanoslit facilitates high cation selectivity after the functionalization and the minute cross-sectional area of the microchannels ensures high salinity gradients across it. The electrical current is harvested from the exchanger by coating the bottom surface of the microchannels with Ag/AgCl electrodes, that maintain the microchannels carrying high concentration electrolyte at a uniform potential (V_H) and the low concentration electrolyte at potential (V_L).

We study the coupled transport of ions inside the solid-state exchanger, to optimize its dimensions, by considering the exchanger as a 2D array comprising of fundamental repeating units called *Elemental Nanofluidic Exchangers*. The Elemental exchanger comprises of two halves of adjacent microchannels in the Solid-state exchanger, with the nanoslit running in between them. Each individual microchannel in the Elemental exchanger hence has a width of b, leading to a periodicity of $(2b + W)$ within the Solid-state exchanger. The length of the elemental exchanger is taken equal to L, and the elemental exchangers can also be arranged end-to-end along the transverse axis. The top-view schematic of the

Solid-state exchanger is given in fig. 2.2, along with the isometric schematic of the Elemental exchanger (defined by the black dotted lines) on the right. This elemental exchanger will be the fundamental building block which can be repeated in a 2D array to produce a functional multi-scale exchanger (elaborated in Chapter-5).

2.2 A Toy-Model for the Elemental Nanofluidic Exchanger

Prior to building a realistic model that describes the dynamics of fluids in the elemental exchanger, it is important to identify the parameters that can describe the state of the system, and get a first idea of its global behaviour.

Throughout this manuscript, it is considered that only one type of monovalent electrolyte is involved in power generation. This notion holds from the point of view of the electrolyte supply and transport, but also from the point of view of the redox reactions occurring at the electrodes which are responsible for the conversion of ionic charge flux into an electrical current through the circuit (Fig.2.2). In a sea/fresh water system the anion is predominantly Chloride ion (Cl^-), and hence the redox electrodes could be Ag/AgCl electrodes, with redox reactions written as follows:

$$\mathbf{Ag + Cl^- \longrightarrow AgCl + e^-} \quad \text{(Inside High Concentration Microchannel)}$$
$$\mathbf{AgCl + e^- \longrightarrow Ag + Cl^-} \quad \text{(Inside Low Concentration Microchannel)}$$

In the upcoming sections, we address only the ion transport, and do not model redox reactions at the electrodes as they are considered ideal and without losses.

2.2.1 Ion transport in the Toy-Model

We start our understanding of the dynamics of ions inside the Elemental exchanger by creating a "*toy model*" under the following assumptions:

- **1D approximation in the microchannels :** The mixing of ions inside the microchannel cross-section is assumed uniform and instantaneous. Therefore the respective high and low electrolyte concentration c_h and c_l in the microchannels ($c_{h,l}$ in [atoms/m^3]) depend only on the direction of the flow ($z-$axis in our study).
- **Uniform potential in the microchannels :** The electrodes placed along the microchannels length maintain the microchannels at a uniform potential V_H and V_L respectively, throughout the energy generation process.
- **Uniform velocity $\vec{U} = U\vec{e_z}$ in the microchannels :** The osmotic solvent flux through the nanoslit is neglected. Furthermore, the microchannel liquids are assumed to be in a co-flow configuration.
- **Linear exchange :** The nanoslit is assumed to be perfectly selective to cations ($J^-_{nano}(z) \equiv 0$), and the local electro-diffusive cation flux though the slit depends linearly on the concentrations $c_h(z)$ and $c_l(z)$ in the microchannels:

$$J^+_{nano}(z) = \underbrace{\frac{DH}{W}\big(c_h(z) - c_l(z)\big)}_{\text{Diffusive Flux}} - \underbrace{\frac{\mu_e H}{W}\left(\frac{c_H(z) + c_L(z)}{2}\right)\Delta V}_{\text{Electromigration Flux}} \tag{2.1a}$$

$$\Delta V = V_L - V_H \qquad \mu_e = \frac{De}{k_B T} \tag{2.1b}$$

where $J^+_{nano}(z)$ is the nanoslit flux of cations per unit length along the $z-$axis, leaving the high concentration microchannel and feeding the low

concentration microchannel. The nanoslit height, length and width are H, L and W respectively. The potential difference between the microchannels is denoted by ΔV, the diffusion coefficient of cations is D [m^2/s], and μ_e is the mobility of electron under an electric field given by Einstein Smoluchowski equation[76].

The electroneutrality in the microchannels is maintained by the redox electrodes placed along the microchannel length (bottom face of microchannels in Fig. 2.2). These electrodes compensate for the cation flux from the nanoslit by furnishing/receiving anions to/from the respective microchannels. Specifically, it is assumed that the cations do not react with the electrodes and that the electrochemical reactions are based on addition or removal of anion flux.

Under these conditions, a flux of cations across the nanoslit results to the creation of a number of anions in the high concentration microchannel equal to $-J^+_{nano}(z)$. An equivalent process occurs in the low concentration microchannel, that neutralizes any charge imbalance in the system. Hence the combined effect of charge flux from the nanoslit and the redox reactions at the electrodes result to a source flux per unit exchanger length of amplitude $J_s(z) = J^+_{nano}(z)$ in the low concentration microchannel and $J_s(z) = -J^+_{nano}(z)$ in the high concentration nanochannel.

Under the approximation mentioned above, the governing equation characterizing the change of concentration in each individual microchannel obey an advection - diffusion transport equation[77] written as:

$$\frac{d}{dz}(-D\frac{dc_{l,h}}{dz} + Uc_{l,h}) = \pm\frac{J^+_{nano}(z)}{S_M} = \pm\frac{J_s(z)}{S_M} \tag{2.2}$$

where $J^+_{nano}(z)$ (in [atom/m.s]) is given by eq. 2.1, and $S_M = ab$ is equal to the cross-section of one microchannel.

These transport equations have to be supplemented with boundary conditions at the inlet ($z = 0$) and outlet ($z = L$) of the exchanger. The boundary conditions are can either be formulated in terms of prescribed values of the 'fields' (microchannel concentrations in our case) to be solved, called Dirichlet-boundary conditions, or in terms of the prescribed values of the 'gradient of the fields' to be solved, called Neumann-boundary conditions.

Dirichlet-boundary conditions are not appropriate at the microchannel outlet ($z = L$) as we do not control the electrolyte concentrations downstream of the exchanger. Hence the appropriate boundary condition at the exit is to consider that the electrolyte concentration reached at this point is simply carried downstream using convection without further concentration change, corresponding to the Neumann-boundary condition, expressed below:

$$\frac{dc_{h,l}}{dz} = 0 \qquad z = L \tag{2.3}$$

The situation at the microchannels' entrance ($z = 0$) is different as we inject an electrolyte of high concentration c_H in the high concentration flow ducts and an electrolyte of low concentration c_L in the low concentration flow ducts. Therefore we have control over the value of the injected concentrations inside the device. However, a Dirichlet-boundary condition is still not appropriate at $z = 0$, as we do not have complete control over the inlet concentrations at the exact point of entry into the exchanger. The feeding of the microchannels is accomplished by organizing a feed-circuit that can flush the entrance of the microchannels along with injecting fluids inside them. This fluidic connection at the inlet hence corresponds to feeding of a concentration flux ($Uc_{H,L}$) as shown in the figure below:

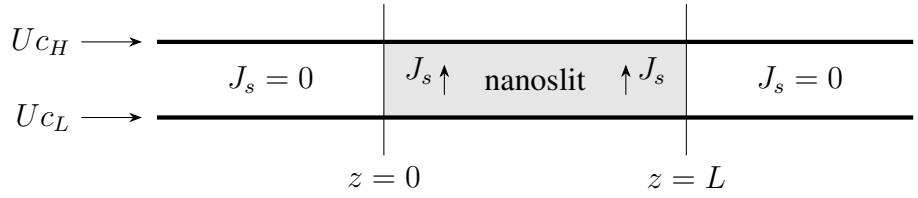

Hence the appropriate boundary condition at the microchannel entrance is a prescribed value of flux that is written as:

$$-D\frac{dc_{h,l}}{dz} + Uc_{h,l} = Uc_{H,L} \qquad \text{at } z = 0 \tag{2.4}$$

2.2.2 Non-Dimensional Equations and Parameters

We can express the transport equation (2.2) and the nanoslit flux (eq.2.1) , together and arrive at the following equations:

$$D\frac{\partial^2 c_l}{\partial z^2} - \vec{U}\frac{\partial c_l}{\partial z} + \frac{DH}{S_M W}\big(c_d(z) - \frac{e}{2k_B T}c_s(z)\Delta V\big) = 0 \tag{2.5a}$$

$$D\frac{\partial^2 c_h}{\partial z^2} - \vec{U}\frac{\partial c_h}{\partial z} - \frac{DH}{S_M W}\big(c_d(z) - \frac{e}{2k_B T}c_s(z)\Delta V\big) = 0 \tag{2.5b}$$

where $c_s = c_h + c_l$ and $c_d = c_h - c_l$ are respectively the sum and difference of the local ion concentration inside high and low concentration microchannel. S_M is the cross-sectional area of the microchannel.

In order to solve the above equations it is of interest to re-scale the length (z) by the length L of the microchannels and potential difference (ΔV) with respect to the thermal potential $k_B T/e$. We also introduce two non-dimensional parameters called *Péclet number* (Pe) and exchange ratio (J):

$$\boxed{\bar{z} = \frac{z}{L} \qquad \Delta\Psi = \frac{e\Delta V}{k_B T} \qquad Pe = \frac{UL}{D} \qquad J = \frac{HL^2}{WS_M}} \tag{2.6}$$

The equations (2.5a,2.5b) hence take the following form:

$$-\frac{\partial^2 c_h}{\partial \bar{z}^2} + Pe\frac{\partial c_h}{\partial \bar{z}} + J(c_d - \frac{c_s}{2}\Delta\psi) = 0 \tag{2.7a}$$

$$-\frac{\partial^2 c_l}{\partial \bar{z}^2} + Pe\frac{\partial c_l}{\partial \bar{z}} - J(c_d - \frac{c_s}{2}\Delta\psi) = 0 \tag{2.7b}$$

The *Péclet number* (Pe) compares the relative importance of the convection and the longitudinal diffusion over the length L of the microchannel and is defined as the ratio of the convection flux in a channel to its diffusive flux.

The exchange ratio (J) is a purely geometrical number gathering the dimensions of the nanoslit and the microchannels. It is equal to the ratio of the geometrical conductance HL/W of the nanochannel, to the geometrical conductance S_M/L of the microchannel. It characterizes the relative importance of the ion exchange through the nanoslit, to their longitudinal diffusion in the microchannel. We will elaborate further on it in the upcoming sections of this chapter.

Finally it is of interest to introduce the *Sherwood number* (Sh) defined as

$$Sh = \frac{Pe}{J}$$

The *Sherwood number* represents the ratio of longitudinal convection rate (z-direction) to the transverse diffusion rate through the nanoslit (x-direction). The work of *Lee et. al*[78] explains Sherwood number to be more appropriate in characterizing systems similar to the elemental exchanger, as opposed to relying solely on Péclet number as the latter does not provide the means to quantify diffusive flux through an ion exchange interface.

2.2.3 Electrolyte Concentration Inside the Microchannels

Solving equation 2.7a and 2.7b simultaneously, it is clear that the sum of the microchannel concentrations (c_s) at any point inside the exchanger is constant and equal to the sum of the entrance concentrations of microchannel liquids:

$$\boxed{c_s = c_S = c_L + c_H} \tag{2.8}$$

where $c_{L,H}$ are the entrance concentrations in the low and high concentration microchannels in [atoms/m^3] respectively.

The differential equation governing the difference in local microchannel concentrations $c_d = c_h - c_l$ is obtained by subtracting equation 2.7a from eq. 2.7b:

$$\frac{\partial^2 c_d}{\partial \bar{z}^2} - Pe\frac{\partial c_d}{\partial \bar{z}} - 2J\big(c_d(\bar{z}) - \frac{c_S}{2}\Delta\Psi\big) = 0 \tag{2.9}$$

The equation above is to be solved with the following boundary conditions:

$$Pec_D = Pec_d(0) - \frac{\partial c_d}{\partial \bar{z}}|_{\bar{z}=0} \qquad \text{and} \qquad \frac{\partial c_d}{\partial \bar{z}}|_{\bar{z}=1} = 0$$

The general solution for the equation 2.9 is written as:

$$c_d - \frac{c_S}{2}\Delta\psi = B_1 e^{m_1\bar{z}} + B_2 e^{m_2\bar{z}} \qquad m_{1,2} = \frac{Pe \pm \sqrt{Pe^2 + 8J}}{2} \tag{2.10}$$

where the constants B_1, B_2 satisfy the boundary conditions written below:

$$B_1 m_1 e^{m_1} + B_2 m_2 e^{m_2} = 0$$
$$B_1(Pe - m_1) + B_2(Pe - m_2) = Pe\big(c_D - \frac{c_S}{2}\Delta\psi\big)$$

Leading us to the following expressions for constants B_1 and B_2:

$$B_1 = -\frac{\left(c_D - \frac{c_S \Delta\psi}{2}\right) Pe m_2 e^{m_2}}{m_1^2 e^{m_1} - m_2^2 e^{m_2}} \qquad B_2 = \frac{\left(c_D - \frac{c_S \Delta\psi}{2}\right) Pe m_1 e^{m_1}}{m_1^2 e^{m_1} - m_2^2 e^{m_2}}$$

The resulting particular solution for the difference in local concentrations inside the microchannel within the range $0 \leq \bar{z} \leq 1$ is hence written as:

$$\boxed{c_d(\bar{z}) - \frac{c_S}{2}\Delta\psi} = \Big(c_D - \frac{c_S \Delta\Psi}{2}\Big)\mathcal{C}(z) \qquad c_D = c_H - c_L \tag{2.11a}$$

$$\mathcal{C}(z) = \frac{m_2 e^{m_2 + m_1 \bar{z}} - m_1 e^{m_1 + m_2 \bar{z}}}{m_2 e^{m_2} - m_1 e^{m_1} - 2(Sh)^{-1}(e^{m_1} - e^{m_2})} \tag{2.11b}$$

The expressions for the individual microchannel concentrations can be derived from the solution of the set of equations expressed in eqs. 2.11 as:

$$c_h(\bar{z}) = \frac{c_d(\bar{z}) + c_S}{2} \qquad c_l(\bar{z}) = \frac{c_S - c_d(\bar{z})}{2} \tag{2.12}$$

The function $\mathcal{C}$ is non-dimensional and its value is heavily dependant on the microchannel convection velocity. Hereafter, we analyse the variation of the microchannel concentration with respect to a variable convection velocity, for a given geometry of the elemental exchanger, that is for a given value of exchange parameter J. Figure 2.3 shows the microchannel concentration at the outlet of the elemental exchanger for convection velocities ranging from 1μm/s to 100m/s, plotted as a function of Sherwood number. The initial concentrations in the microchannels are equal to 1 M and 1 mM respectively, the microchannel has the dimensions 1μm$\times$2μm$\times$100μm, the nanoslit dimensions are 1nm$\times$100nm$\times$100μm. In this analysis we ignore the effect of electro-migration *i.e.* we assume that the

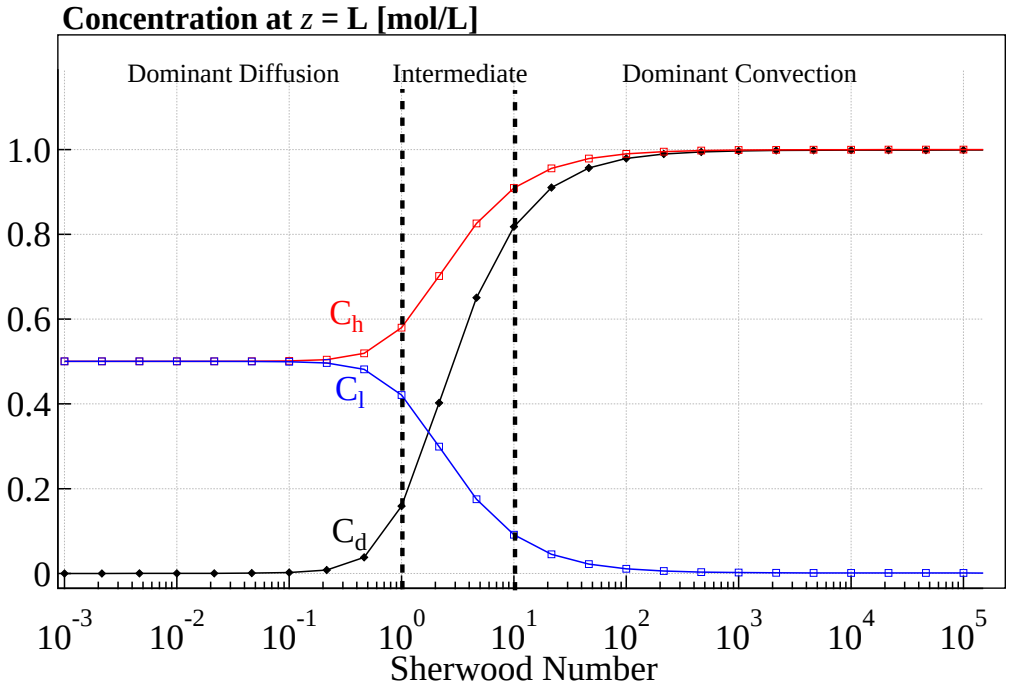

Figure 2.3: Microchannel concentrations at the outlet of the elemental exchanger as a function of Sherwood number, with the absence of electrode potential. The blue and red lines corresponds to the outlet concentration of low salinity and high salinity solutions respectively and the black line represents the concentration difference at the outlet. The initial concentrations were assumed to be 1 M and 1 mM in high and concentration microchannels respectively. The exchanger has a nanoslit of height 1 nm, width 20 nm and length 10 μm. The microchannels have a square cross section of side 500 nm and Sherwood number was varied from 10^{-3} to 10^5.

electrical potential difference is zero ($\Delta V = \Delta\Psi = 0$).

It is clear from figure 2.3 that we have three regimes of ion-exchange inside the microchannel as we increase the convection velocity:

- Low Sherwood regime ($Sh \leq 1$): In this regime the ion concentrations in the microchannels are equal by the time the fluids reach their respective outlet (0.5M in our example). This signifies that the process of transverse diffusion is dominant compared to the longitudinal convection. The

diffusive flux of cations from the high concentration microchannel results to the increase in the concentration of ions in the microchannel with low ionic concentration. This process continues till the equilibrium concentration is reached, after which the liquids flow across the exchanger without any transverse flux. Operating the exchanger in this regime is not beneficial as the transverse flux essential for the generation of electricity terminates before the outlet, leading to a dead length in the device where fluid consumes hydrodynamic energy to maintain velocity, without producing any electric current.

- Intermediate regime ($1 \leq Sh \leq 10$): As the convection velocity is increased, the transverse diffusion of ions starts to get compensated by the longitudinal convection in the microchannel. This convection ensures a supply of fresh ions inside the high concentration microchannel as the ions diffuse across the nanoslit. As a result, the microchannel concentration starts to stabilize whilst maintaining a significant amount of ion-flux across the nanoslit. It can be seen in fig. 2.3 at Sh = 10 that the change in microchannel concentrations is less than 10% of its initial value and hence this value of Sherwood number is treated as the limiting value for the intermediate regime.

  An important aspect of the toy model is the transition in the regime from diffusion dominant to convection dominant, which occurs within one decade of increasing the value of Sherwood number from 1 to 10. This sharp change is characteristic to the approximation of linear transport inside the nanoslit. In the upcoming chapters we will observe that under non-linear surface driven transport (Chapter - 4), this transition occurs over two or three decades of increase in Sherwood number.

- High Sherwood regime ($Sh \geq 10$): The high Sherwood regime is reached when the ion concentrations in both microchannels remains constant and equal to their input concentration. Here, the convection velocity is high enough to compensate for the transverse diffusion and the ions in the microchannel are rapidly replenished (in high concentration microchannel) or flushed (in low concentration microchannel) before there can be any appreciable change in their respective ion concentrations. As a result, the local difference in the concentrations in the exchanger stabilizes, resulting to a constant diffusive flux across the nanoslit. This regime produces the highest electrical power density (explained further in the next sections of this chapter). Operating the exchanger in this regime however, eventually requires high hydraulic power input which can diminish the net power obtained from the exchanger. Additionally, achieving high velocities in the microchannels has also its own practical implications regarding the ability of the device to sustain the required pressure. These aspects are further analyzed in Chapter - 4.

2.3 Elemental Exchanger as an Electrical Generator

2.3.1 Current-Voltage Characteristics

The elemental exchanger produces electricity by the exchange of cations similar to an electrochemical cell. The difference between this exchanger and an electrochemical cell is the lack of a chemical reaction at the electrodes. In the elemental exchanger, the difference in electroneutrality caused by the migration of cations is compensated by the electrodes that add or remove electrons from the microchan-

nels. This addition/removal of electrons acts as a source of electrical current as illustrated in fig.2.2. In this section, we evaluate the expression for the current produced by the elemental exchanger, under the approximations mentioned in section 2.2 of this chapter.

The electrode flux per unit length of the exchanger (J_{elec}) is defined as the flux of electrons released by the electrode to compensate for the difference in cation concentration in each microchannel. Hence, it is quantified as:

$$J_{elec}(z) = J^{+}_{nano}(z) - J^{-}_{nano}(z) = J^{+}_{nano}(z) \tag{2.13}$$

The toy-model nanoslit is considered perfectly selective and hence the anions flux per unit length in the nanoslit J^{-}_{nano} is considered equal to zero.

The expression for current can be found by integrating this electrode flux over the exchanger length L:

$$I = e\int_0^L J_{elec}\partial z = e\int_0^1 J_{elec}\partial \bar{z} \tag{2.14}$$

It is of interest to use the expression for J^{+}_{nano} given by the advection-diffusion equation (eq.2.9):

$$J^{+}_{nano} = \frac{S_M}{2}\frac{\partial}{\partial \bar{z}}\Big(D\frac{\partial c_d}{\partial \bar{z}} - \vec{U}c_d\Big) \tag{2.15}$$

This leads to the following expression for the current intensity:

$$\frac{I}{eS_M} = \frac{1}{2}\Big(D\Big[\frac{\partial c_d}{\partial \bar{z}}\Big]_0^1 - \vec{U}[c_d]_0^1\Big) \tag{2.16}$$

Evaluating the derivative of c_d from equation 2.11 and simplifying, the expression

for current is written as:

$$\boxed{I = \frac{eDHL}{2W}\Big(c_D - \frac{c_S \Delta\Psi}{2}) f_{toy}(Sh, J)} \tag{2.17}$$

where c_S and c_D are the sum and difference of the microchannel inlet concentrations respectively. The function f_{toy} is non dimensional and is expressed as follows:

$$f_{toy}(Sh, J) = Sh + \frac{Sh^2 e^{m_2}(m_2 - m_1)}{m_1 Sh + 2 - e^{m_2 - m_1}(m_2 Sh + 2)} \tag{2.18}$$

$$m_{1,2} = \frac{Sh \times J \pm \sqrt{Sh^2 J^2 + 8J}}{2} \tag{2.19}$$

It is evident that the $I - \Delta V$ characteristics given by eq. 2.17 corresponds to a linear current generator. Ohm's law describes the electromotive force as the potential drop across a circuit when the current flowing through the circuit drops to zero. Hence from equation 2.17, the electromotive force of the exchanger, E, and the internal resistance, r, are expressed as follows:

$$E = \frac{2k_B T}{e}\frac{c_D}{c_S} \qquad r = \frac{4k_B T}{c_S D e^2}\frac{W}{HL}\frac{1}{f_{toy}} \tag{2.20}$$

2.3.2 Maximum Power Generated by the Elemental Exchanger

The expression for power generated by a circuit connected to an external resistance, R_{ext} is found using Ohm's law and is written as:

$$P_{elec} = \frac{E^2 R_{ext}}{(r + R_{ext})^2} \tag{2.21}$$

This power is maximum when the external resistance of the circuit is equal to the internal resistance and the resulting equation for the maximum power is given as:

$$P_{elec}^{max} = \frac{E^2}{4r} \tag{2.22}$$

As the elemental exchanger is intended to be parallelized, evaluating the power produced per unit surface area of the global exchanger *i.e.*, its power density (Pd), provides a better metric of comparison with the current state of the art exchanger systems like Pressure Retarded Osmosis (PRO) and Reverse Electrodialysis (RED) systems. The elemental exchanger has a length 'L' and a total width of '$2b$' approximately, as the width of the nanoslit is considered very small to make an appreciable impact on the exchanger surface area. Hence the maximum power density (Pd_{elec}^{max}) the exchanger can provide is written as follows:

$$Pd_{elec}^{max} = \frac{1}{2bL}\frac{E^2}{4r} \tag{2.23}$$

where $2bL$ is the surface area of the exchanger.

Substituting the values for the electromotive force and the internal resistance from eq. 2.20:

$$Pd_{elec}^{max} = \frac{Dk_BT}{8}\frac{c_D^2}{c_S}\frac{H}{bW}f_{toy}(Sh, J) \tag{2.24}$$

The expression for f_{toy} is given in equation 2.18. We now introduce the contrast ratio (Cr) as the ratio of the inlet concentration in the high concentration microchannel to that of the low concentration microchannel *i.e.*:

$$Cr = \frac{c_H}{c_L} \tag{2.25}$$

where c_H and c_L are the inlet concentrations in the high and low concentration

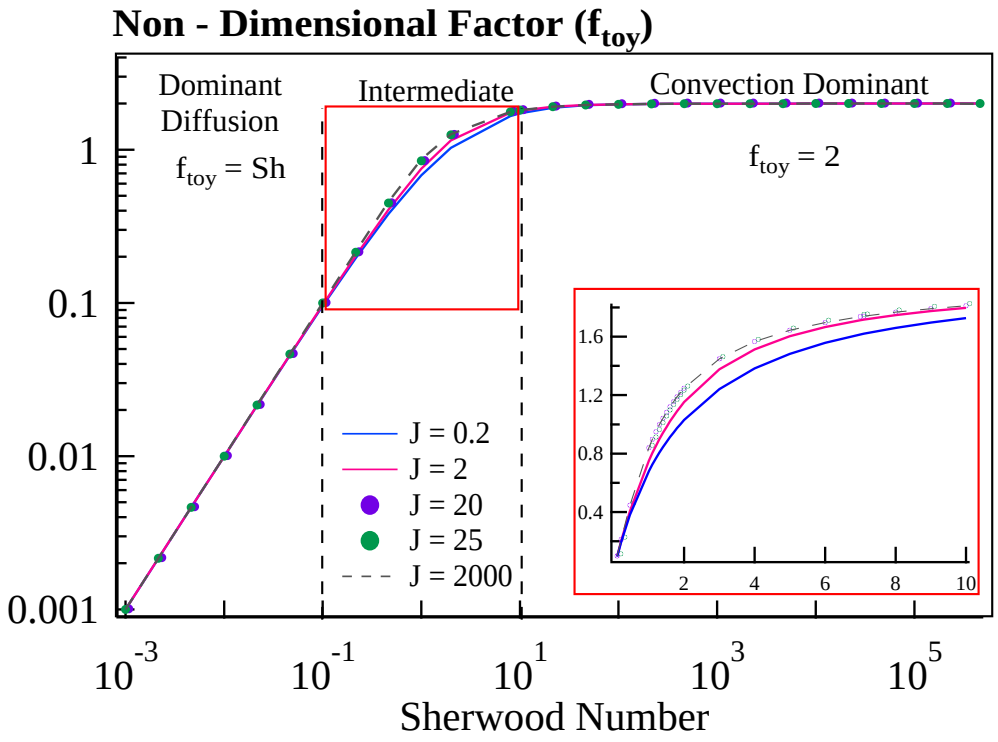

Figure 2.4: Variation of factor f_{toy} (eq. 2.18) with Sherwood Number for several values of conductance ratio J. The initial microchannel concentrations were 1 M and 1 mM. A linear increase of $f_{toy} = Sh$ is seen in the low Sherwood regime, and a saturation of f_{toy} at $Sh = 10$ to a value equal to 2. The transition between diffusion dominated regime to that of convection dominated is very sharp as it only spans two decades of increase in Sherwood number. The inset is the magnified plot of the intermediate regime in linear scale.

microchannels respectively, the power density can therefore be rewritten as:

$$Pd_{elec}^{max} = \frac{Dk_BTc_D}{8}\frac{Cr-1}{Cr+1}\frac{H}{bW}f_{toy}(Sh,J)$$

Figure 2.4 illustrates the change in the non-dimensional factor (f_{toy}) with varying Sherwood number for a fixed geometry *i.e.* fixed J, and fig. 2.5 is the same plot for the power density generated by the exchanger. Upon comparing the two figures, it is clearly seen that the non-dimensional factor (f_{toy}) (eq. 2.18), defines

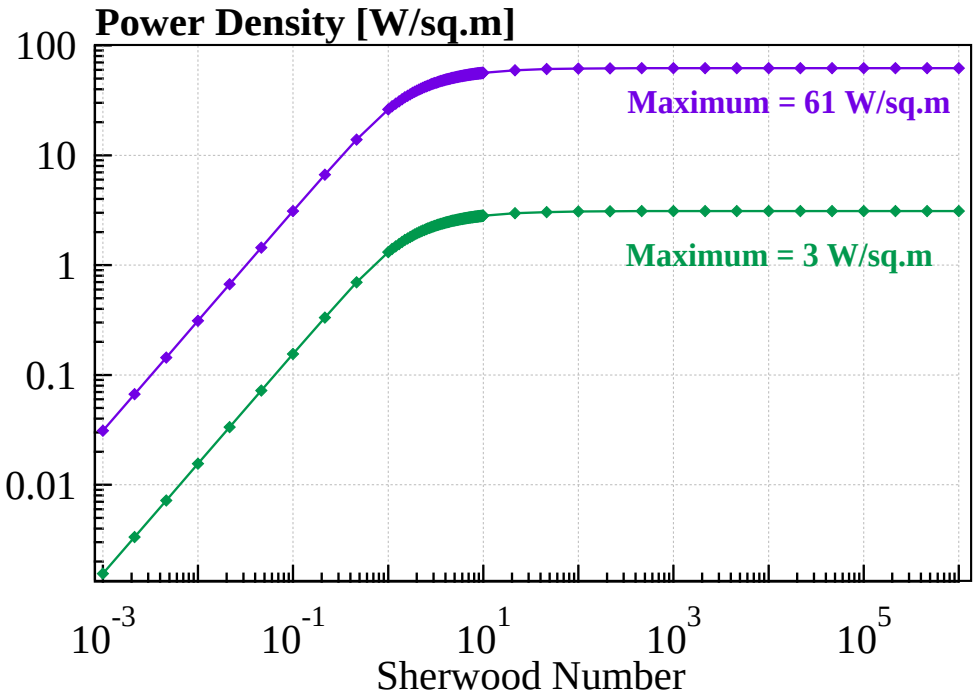

Figure 2.5: The variation of Power density generated by the exchanger with Sherwood number. The power density follows the same trend as factor f_{lin} and is multiplied with the coefficient expressed in eq. 2.24. The curves correspond to the two sets of dimensions discussed in eq. 2.26, resulting to a conductance ratio of $J = 20$ in purple and $J = 25$ in green. The two dimension sets conform to achievable dimensions given the current advancement in Silicon fabrication (green) and the ideal dimensions to maximise generated power (purple).

the state of the elemental exchanger.

We notice the remarkable result at the limiting high and low Sherwood regimes, as the limit values of $f_{toy}(Sh, J)$ do not depend on the exchange parameter (J). This shows that the Sherwood number is certainly more appropriate than the Péclet number to describe and understand the effect of the exchanger's replenishing rate on its power capability, with the effect of J being noticeable only in the intermediate Sh range. The high and low Sherwood limiting regimes can be calculated

by expanding eq. (2.18) as:

$$Sh \to 0 \qquad f_{toy}(Sh, J) \simeq Sh$$
$$Sh \to 2 \qquad f_{toy}(Sh, J) \simeq 2$$

In the low Sherwood regime, the power density increases linearly with the velocity as the Sherwood number increases. This linear increase of the power density with increasing convection velocity is due to the replenishment of ions inside the high concentration microchannel. Taking the limit value $f_{toy} = Sh$ at low Sherwood, we find that the power density can be simplified to:

$$P_{elec}^{max} = \frac{k_B T c_D}{4} \frac{c_D}{c_S} U S_M$$

The recovered power is essentially 1/4 of the osmotic power, $k_B T c_D U S_M$, fed into the exchanger and does not depends on its characteristics.

At high values of the Sherwood number, the non-dimensional power density saturates to a maximum value of 2. In this regime the concentration of electrolyte is maintained at the nominal inlet values c_H and c_L in the microchannels, and the recovered power is limited by the transport in the nanoslit:

$$P_{elec}^{max} = k_B T c_D \frac{c_D}{2 c_S} \frac{DHL}{W}$$

The numerical value of the power generated by the exchanger per unit surface is shown in fig 2.5 for two sets of dimensions (fixed conductance ratios, J) given

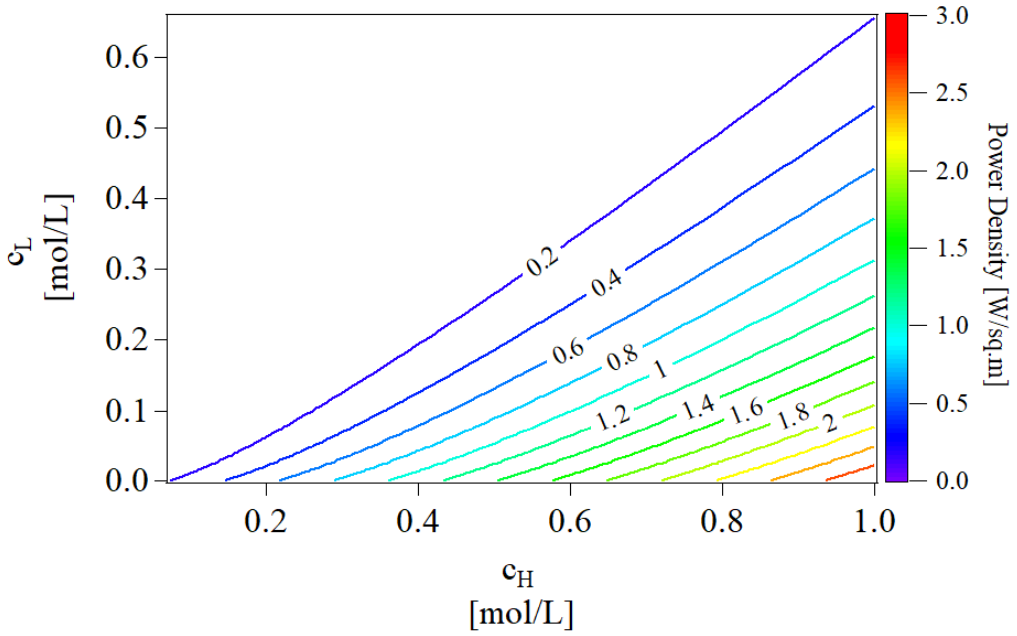

Figure 2.6: The maximum power density generated by exchanger for different microchannel concentrations, under linear approximation of nanoslit flux with perfect microchannel mixing. Exchanger dimensions are mentioned in eq.2.26a.

below:

$$L = 100\mu\text{m} \qquad a = 2b = 2\mu\text{m} \quad H = 1\text{nm} \quad W = 100\text{nm} \tag{2.26a}$$

$$L = 10\mu\text{m} \qquad a = 2b = 500\text{nm} \quad H = 1\text{nm} \quad W = 20\text{nm} \tag{2.26b}$$

The first set of dimensions are achievable using the existing *Silicon-on-insulator* technologies, whereas the second set of dimensions are the ideal case dimensions, capable of extracting the higher density of power from the exchanger. The Sherwood number is varied from 10^{-3} to 10^{5}. The inlet concentrations are assumed to be 1 M and 1 mM in the high and low concentration microchannels respectively.

The two sets of values generate respectively in a high Sherwood limit, a power density respectively equal to 3 W/m^2 and 61 W/m^2. Furthermore, figure 2.6 illus-

trates the maximum power density that could be achieved with the system corresponding to the dimensions (2.26a) when operated with various inlet concentrations. An interesting result from the fig.2.6 is that the theoretical power density that could be extracted from the mixing of sea water (600mM) with that of river water (1mM), is approximately 2 W/sq.m. These theoretical power densities are comparable to commercially available technologies for Blue energy extraction such as *Pressure Retarded Osmosis (PRO)* that provides a power density of 6.5 W/sq.m[79] whereas a full scale *Reverse Electrodialysis (RED)* system produces 1.6 W/sq.m[31]. Thus we could conclude from the analysis of our toy-model and from fig. 2.5, that the power densities of the elemental exchanger could be greatly enhanced by diminishing the width 'W' of the nanoslit and the width 'b' of the nanochannels, and could eventually reach much higher values than commercially available membranes. However we should keep in mind that the hypothesis of perfect selectivity and linear flux used in the toy model are not feasible in the real world, and the transport in the nanoslit has to be taken into account for its non-linear dynamics.

2.4 Conclusions and Perspectives

The key results of this chapter can be summarized as follows:

- We introduced the concept of an *Elemental Nanofluidic Exchanger*, which consists of a set of two microchannels separated by a thin nanoslit running in between, along the length of the channels.
- We established the governing equations controlling the ion concentration inside the microchannels, by approximating the nanoslit flux to be linearly varying with the local concentration difference across its width.

- We evaluated the variation of microchannel concentration with the change in fluid velocity and introduced a new parameter called *Sherwood number*. The analysis of the microchannel concentration revealed the three regimes in which the exchanger can operate, with each regime being characterized by the value of the Sherwood number.
- We calculated an analytical expression for the current generated and the density of power the exchanger is capable of producing under the linear approximation of nanoslit flux. Investigation of the power density with varying flow velocity of microchannel fluids revealed a direct correlation between the power produced and the regime of Sherwood number the exchanger is working under, with the maximum power reaching at the high Sherwood regime ($Sh \geq 10^2$).
- Lastly, the maximum density of power was found to be significantly impacted by the contrast ratio (Cr) between the inlet microchannel concentrations and the initial concentration difference (c_D) between the two microchannels. This analysis also revealed the elemental exchanger is theoretically capable of producing 2 W/sq.m of electrical power density when operated with sea water (600 mM) and river water (1 mM), which is expected to increase as we further characterize the dynamics of ions inside the nanoslit.

CHAPTER 3

Dynamics in the Nanoslit using 1D Poisson-Nerst-Planck Approximation

3.1 Introduction

This chapter focuses on the dynamics of fluids in a nanoslit of nanometric height. The previous chapter approximated the fluxes inside the nanoslit to have a linear response to the concentration gradient across its width and also assumed it to be perfectly selective to cations. We amend this approximation in the present chapter by solving the Poisson-Nerst-Planck (PNP) equations in the nanoslit, and calculate the non-linear expressions of the cations and anions fluxes J^{+}_{nano} and J^{-}_{nano} per unit length in the z-direction, crossing the nanoslit and acting as source/sink in the microchannels.

The nanoslit is considered locally in $z-$axis as a two-dimensional object, extending over a width 'W' in the x-direction normal to the microchannels axis, and of height 'H' in the y-direction. It bears a surface charge '$\sigma < 0$' to favour the transport of cations. Using PNP - equations averaged over the thickness H, neglecting osmotic volume fluxes and convection effects in the nanoslit, as well as all nanofluxes in the z-direction, we derive expressions for the nanoslit fluxes as a function of the local Dukhin numbers built on the high and low electrolyte concentrations in the neighbouring microchannels, and the potential difference $\Delta\Psi$ between them. It is found that the selectivity of the nanoslit is implicitly coupled to the non-dimensional parameters. The analysis in this chapter describes the piv-

otal role of the nanoslit selectivity and details the semi-analytical solution of the implicit equation.

The last section of this chapter studies the limit power density that could be obtained in the elemental exchanger at infinitely high velocity and maintaining the nominal electrolyte concentrations 'c_H' and 'c_L' at the entrance and outlet of the nanoslit.

3.2 Governing Equations for Ion transport in the Nanoslit

In this chapter, we address the dynamics of ions transport in the nanoslit by solving the Poisson-Nerst-Planck equation using the boundary conditions relevant to the elemental exchanger. The selectivity of the nanoslit to cations is achieved by coating it with a negative surface charge of density $\sigma < 0$ on its two faces that are exposed to ions.

The focus of this chapter is mainly on deriving a semi-analytical expression for the nanoslit fluxes, as a function of the local ion concentration in the microchannels at the entrance/outlet of the nanoslit, and as a function of the potential difference between the microchannels.

This chapter studies the fluxes in the nanoslit under the following approximations:

- **1D approximation:** At a given abscissa 'z' along the microchannel axis, the nanoslit is assumed to be one dimensional, extending along its length W in the *x*-direction. The cation and anion concentrations in the nanoslit are considered uniform along the y-direction; their flux J^+_{nano} and J^-_{nano} are integrated over the thickness and calculated per unit width dz of the

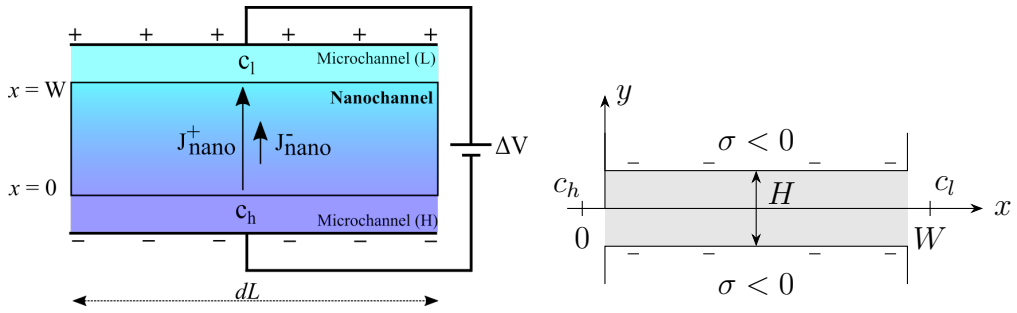

Figure 3.1: Schematic of nanoslit section of length *dz*. The nanoslit has width W, spanning from the high to the low concentration microchannel. Potential ΔV is applied across this width, with low concentration microchannel at a higher potential compared to the other. J^+_{nano} and J^-_{nano} are the cationic and the anionic flux per unit length dz respectively with $J^+_{nano} > J^-_{nano}$ due to surface charge "σ" on the two faces of the nanoslit exposed to the ions.

nanoslit. No fluxes along the z-direction are considered in the nanoslit. The schematic is shown in fig.3.1.

- **Poisson-Nernst-Planck equations without flow:** the flux of ions takes into account only their diffusion and migration along the electrostatic field, using the Poisson-Nernst-Planck equations. The convection component accounting for the osmotic flow of solvent as described in *Picallo et. al.*[80] has been omitted.

- **No dissipation at the nanoslit/microchannel junction:** the boundary conditions at the entrance and outlet of the nanoslit correspond to a continuous electro-chemical potential, and neglect further dissipation effects at the junction. The local electrolyte concentration in the microchannels are noted c_h and c_l.

- **Electroneutrality of the nanoslit:** the density of cations and anions in the nanoslit is assumed to equilibrate the surface charge at all location "x". The surface charge is considered constant and no charge regulation process is considered.

3.2.1 1D Poisson-Nernst-Planck Equations

The ions inside the nanoslit migrate from the region of high concentration to the low concentration region due to diffusion, as described by Fick's law[81] along with migrating under the effect of the electrostatic field. Under the above approximations, the nanoslit fluxes per unit length in the nanoslit are written as[82]:

$$J^{+}_{nano} = \underbrace{-D^{+}H\frac{dc^{+}}{dx}}_{\text{Diffusive Flux}} + \underbrace{\frac{D^{+}}{k_BT}Hc^{+}e\vec{E}_x}_{\text{Electromigration Flux}} \tag{3.1a}$$

$$J^{-}_{nano} = \underbrace{-D^{-}H\frac{dc^{-}}{dx}}_{\text{Diffusive Flux}} - \underbrace{\frac{D^{-}}{k_BT}Hc^{-}e\vec{E}_x}_{\text{Electromigration Flux}} \tag{3.1b}$$

Here $D^{\pm}$ and $c^{\pm}$ are the diffusion coefficient and concentration of the cations and anions, and *H* is the nanoslit height. The superscripts "+" and "−" correspond to cations and anions. $\vec{E}_x$ is the electric field across the nanoslit width.

Since the nanoslit remains electroneutral, the charges inside the nanoslit obey they following equation:

$$c^{+} - c^{-} = -\frac{2\sigma}{eH}$$

Expressing the electric field as the gradient of potential and introducing the normalized potential (Ψ) and normalized coordinate $\bar{x} = x/W$ leads to:

$$-\frac{J^{+}_{nano}W}{D^{+}H} = K^{+} = \left(\frac{\partial c^{+}}{\partial \bar{x}} + c^{+}\frac{\partial \Psi}{\partial \bar{x}}\right) \qquad \vec{E} = -\frac{\partial \vec{V}}{\partial x} \tag{3.2a}$$

$$-\frac{J^{-}_{nano}W}{D^{-}H} = K^{-} = \left(\frac{\partial c^{-}}{\partial \bar{x}} - c^{-}\frac{\partial \Psi}{\partial \bar{x}}\right) \qquad \partial\Psi = \frac{e}{k_BT}\partial V \tag{3.2b}$$

$$c^{+} - c^{-} = -\frac{2\sigma}{eH} \tag{3.2c}$$

Here K^{+} and K^{-} are reduced nanoslit fluxes.

The local selectivity of the nanoslit is usually defined as:

$$t = \frac{J^+_{nano} - J^-_{nano}}{J^+_{nano} + J^-_{nano}}$$

where J^+_{nano}, J^-_{nano} are the cationic and the anionic flux per unit length inside the nanoslit respectively. In this model we rather define the selectivity from the reduced ion fluxes:

$$t = \frac{K^+ - K^-}{K^+ + K^-} \tag{3.3}$$

When cations and anions have the same diffusivity, the two expressions for selectivity (t) overlap. If the nanoslit is considered perfectly selective, then $t = \pm 1$, with $t > 0$ for cation selective nanoslit and vice versa.

3.2.2 Boundary Conditions

We consider the points at $x = 0$ and $x = W$ as the boundaries of the nanoslit. The boundary conditions for the nanoslit hence involves the equality of the electrochemical potential of cations and anions at the boundary points, within the nanoslit on one side, and in the microchannels on the other side. These boundary conditions are written as follows:

$$k_B T \ln(c_h) + eV_H = k_B T \ln\left(c^+_{x=0}\right) + eV_{\bar{x}=0} \tag{3.4a}$$

$$k_B T \ln(c_h) - eV_H = k_B T \ln\left(c^-_{\bar{x}=0}\right) - eV_{\bar{x}=0} \tag{3.4b}$$

$$k_B T \ln(c_l) + eV_L = k_B T \ln\left(c^+_{\bar{x}=1}\right) + eV_{\bar{x}=1} \tag{3.4c}$$

$$k_B T \ln(c_l) - eV_L = k_B T \ln\left(c^-_{\bar{x}=1}\right) - eV_{\bar{x}=1} \tag{3.4d}$$

Left side of the equations correspond to entities in the microchannel and the right side to that of the nanoslit. The subscript on the right side provides the position inside the nanoslit with $\bar{x} = 0$ indicating the interface with high concentration mi-

crochannel and $\bar{x} = 1$ indicating the interface with low concentration microchannel.

Subtracting equation 3.4b from eq. 3.4a, and equation 3.4d from eq. 3.4c, we arrive at the continuity equations at the micro-nano interface.

$$\Psi_H - \frac{1}{2} ln(\frac{c^+_{\bar{x}=0}}{c^-_{x=0}}) = \Psi_{\bar{x}=0} \tag{3.5a}$$

$$\Psi_L - \frac{1}{2} ln(\frac{c^+_{\bar{x}=1}}{c^-_{\bar{x}=1}}) = \Psi_{\bar{x}=1} \qquad \Psi = \frac{eV}{k_B T} \tag{3.5b}$$

Similarly, adding equation 3.4a with eq. 3.4b, and eq. 3.4c with eq. 3.4d, reveals a relation between the local microchannel concentration and the concentration of ions at the interface inside the nanoslit:

$$c_h^2 = (c^+ c^-)_{\bar{x}=0} \qquad c_l^2 = (c^+ c^-)_{\bar{x}=1} \tag{3.6}$$

The microchannel concentrations can be normalized to a non-dimensional parameter by introducing Dukhin number which is defined as follows:

$$Du_h = -\frac{\sigma}{eHc_h} \qquad Du_l = -\frac{\sigma}{eHc_l} \tag{3.7}$$

where c_h and c_l are the local microchannel concentrations in the units ions per cubic meter.

Hence using the electroneutrality condition in eq. 3.2c and eq. 3.6, the ion concentration in the two interfaces where the nanoslit meets the microchannels are expressed as:

$$\frac{c^+_{\bar{x}=0}}{c_h} = \sqrt{1+Du_h^2} + Du_h \qquad \frac{c^-_{\bar{x}=0}}{c_h} = \sqrt{1+Du_h^2} - Du_h \tag{3.8a}$$

$$\frac{c^+_{\bar{x}=1}}{c_l} = \sqrt{1+Du_l^2} + Du_l \qquad \frac{c^-_{\bar{x}=1}}{c_l} = \sqrt{1+Du_l^2} - Du_l \tag{3.8b}$$

From equations 3.5 and 3.8, we have an expression of the potential difference and concentration difference at the micro-nano interface inside the nanoslit:

$$\Psi_{\bar{x}=1} - \Psi_{\bar{x}=0} = \Delta\Psi - \ln\left(\frac{c_h(t_l+1)}{c_l(t_h+1)}\right) \tag{3.9}$$

$$(c^+ + c^-)_{\bar{x}=1} - (c^+ + c^-)_{\bar{x}=0} = -\frac{2\sigma}{eH}(t_l - t_h) \tag{3.10}$$

where

$$\Delta\Psi = \Psi_L - \Psi_H \qquad t_{l/h} = \sqrt{1+\frac{1}{Du_{l/h}^2}} \tag{3.11}$$

The logarithm function in eq. 3.9 is the ratio of the cation to the anion concentration inside the nanoslit, with $c_{l/h}$ holding their original notation describing microchannel concentrations.

3.3 Expressions for the Nanoslit Fluxes and Selectivity

3.3.1 The Total Reduced Flux

The general solution for nanoslit fluxes is found using the expressions for the reduced nanoslit fluxes K^+ and K^- given by equation 3.2.

Subtracting equation 3.2b from equation 3.2a and using the electroneutrality con-

dition (eq.3.2c), we get:

$$\frac{\partial \Psi}{\partial \bar{x}} = \frac{K^+ - K^-}{c^+ + c^-} \quad \text{as} \quad \frac{\partial}{\partial \bar{x}}(c^+ - c^-) = 0 \tag{3.12}$$

Adding equations 3.2a and 3.2b:

$$\frac{\partial}{\partial \bar{x}}(c^+ + c^-) - \frac{2\sigma}{eH}\frac{\partial \Psi}{\partial \bar{x}} = K^+ + K^- \quad \text{as} \quad c^+ - c^- = -\frac{2\sigma}{eH} \tag{3.13}$$

Upon integrating the above equation with respect to *x*, we get the first general solution to the nanoslit fluxes with K_0 being the integration constant.

$$(c^+ + c^-) - \frac{2\sigma}{eH}\Psi = (K^+ + K^-)\bar{x} + K_0 \tag{3.14}$$

Using the boundary conditions (3.9) and (3.10) we eliminate K_0 and get the expression of the total normalized flux $K^+ + K^-$:

$$K^+ + K^- = -\frac{2\sigma}{eH}\left(t_l - t_h + \Delta\Psi - \ln\frac{c_h(1+t_l)}{c_l(1+t_h)}\right) \qquad t_{l/h} = \sqrt{1 + \frac{1}{Du_{l/h}^2}} \tag{3.15}$$

This expression gives the reduced flux $K^+ + K^-$ as an explicit function of the concentration and potential conditions in the microchannels.

Introducing a constant parameter "$\mathcal{E}$" defined as:

$$\mathcal{E} = t_h - t_l + \ln\left(\frac{c_h(t_l+1)}{c_l(t_h+1)}\right) \qquad t_{l/h} = \sqrt{1 + \frac{1}{Du_{l/h}^2}} \tag{3.16}$$

simplifies the expression of the total reduced flux:

$$\boxed{K^+ + K^- = -\frac{2\sigma}{eH}\left(\Delta\Psi - \mathcal{E}\right)} \tag{3.17}$$

3.3.2 Implicit Relation for the Nanoslit Selectivity

The second general equation for the nanoslit fluxes is found by substituting the value of $\partial\Psi/\partial\bar{x}$ from equation 3.12 and simplifying it with a function 'ξ' that includes the selectivity of the nanoslit:

$$(c^+ + c^-)\frac{d(c^+ + c^-)}{dx} - \frac{2\sigma t}{eH}(K^+ + K^-) = (K^+ + K^-)(c^+ + c^-)$$

$$(\xi - \frac{2\sigma}{eH}t)\frac{\partial\xi}{\partial\bar{x}} - (K^+ + K^-)(\xi) = 0 \quad \text{with} \quad \xi = (c^+ + c^-) + \frac{2\sigma}{eH}t \tag{3.18}$$

When $\xi \neq 0$, integrating the above equation with respect to *x* reveals the second general equation for the nanoslit fluxes:

$$\xi - \frac{2\sigma}{eH}t\ln(\xi) = (K^+ + K^-)\bar{x} + K_1 \quad \text{when} \quad Du_l \neq Du_h \tag{3.19}$$

From the boundary conditions (3.10), we get the boundary values of ξ as follows:

$$\xi(\bar{x} = 0) = -\frac{2\sigma}{eH}(t_h - t) \qquad \xi(\bar{x} = 1) = -\frac{2\sigma}{eH}(t_l - t)$$

We can now eliminate K_1 and get a second relation given below:

$$K^+ + K^- = -\frac{2\sigma}{eH}\left(t_l - t_h + t\ln\frac{t_l - t}{t_h - t}\right) \tag{3.20}$$

Upon analyzing the equations 3.17 and 3.20 together, we get the following implicit equation for the reduced selectivity of the nanoslit:

$$\boxed{t\ln\left(\frac{t - t_l}{t - t_h}\right) = \Delta\Psi - \ln\left(\frac{c_h(t_l + 1)}{c_l(t_h + 1)}\right)} \tag{3.21}$$

It is evident that equation 3.19 diverges when both the microchannels carry fluids with same ionic concentration ($Du_L = Du_h$) because the function "ξ" becomes equal to zero, leading to an undefined logarithm. Hence substituting ξ=0 in equation 3.18 and expressing the nanoslit concentrations in terms of Dukhin numbers from eq. 3.8 reveals the nanoslit selectivity for equal microchannel concentrations as:

$$t = \frac{\sqrt{1+Du^2}}{Du} \quad \text{when} \quad Du_l = Du_h = Du, \sigma < 0 \tag{3.22}$$

3.3.3 Expressions for the Nanoslit Fluxes

The expressions for the nanoslit fluxes can be found by reorganizing equation 3.17 using the definition of nanoslit selectivity (eq. 3.3).

The equations for the reduced nanoslit fluxes are given as:

$$K^+ = \frac{1+t}{2}(K^+ + K^-) \qquad K^- = \frac{1-t}{2}(K^+ + K^-) \tag{3.23}$$

Expressing the total reduced flux ($J^{\pm}_{nano}$) from equations 3.17 and 3.16, we arrive at the final expressions for the nanoslit fluxes:

$$\boxed{J^+_{nano} = -\frac{D^+\sigma}{eW}(1+t)(\mathcal{E} - \Delta\Psi)} \qquad \boxed{Du_h \neq Du_l} \tag{3.24a}$$

$$\boxed{J^-_{nano} = -\frac{D^-\sigma}{eW}(1-t)(\mathcal{E} - \Delta\Psi)} \qquad \boxed{\sigma < 0} \tag{3.24b}$$

These fluxes are expressed in the units ions per meter second [$m^{-1}s^{-1}$] with the

parameter $\mathcal{E}$ and the selectivity given from equations 3.21 and 3.16:

$$\boxed{\mathcal{E} = t_h - t_l + \ln\left(\frac{c_h(t_l+1)}{c_l(t_h+1)}\right)} \tag{3.25a}$$

$$\boxed{t\ln\left(\frac{t-t_l}{t-t_h}\right) = \Delta\Psi - \mathcal{E} + (t_h - t_l)} \tag{3.25b}$$

When the concentration in both microchannels are equal, *i.e.* $\mathcal{E} = 0$, and the selectivity is given by eq. 3.22, that leads to the following expression:

$$\boxed{J^+_{nano} = \frac{D^+|\sigma|}{eW}\Delta\Psi(1 + \frac{\sqrt{1+Du^2}}{Du})} \qquad \boxed{Du_h = Du_l = Du} \tag{3.26a}$$

$$\boxed{J^-_{nano} = \frac{D^-|\sigma|}{eW}\Delta\Psi(1 - \frac{\sqrt{1+Du^2}}{Du})} \tag{3.26b}$$

Ultimately, the electrical current per unit length dz of the nanoslit is written as:

$$I = e(J^+_{nano} - J^-_{nano}) = \frac{(-\sigma)}{W}\left[D^+ - D^- + t(D^+ + D^-)\right](\mathcal{E} - \Delta\Psi)$$

In the following, without loss of generality with restrict to the case $D^+ = D^-$ and the current intensity per unit nanoslit length is expressed as follows:

$$\boxed{I = \frac{(-2\sigma)D}{W}t(\mathcal{E} - \Delta\Psi)} \tag{3.27}$$

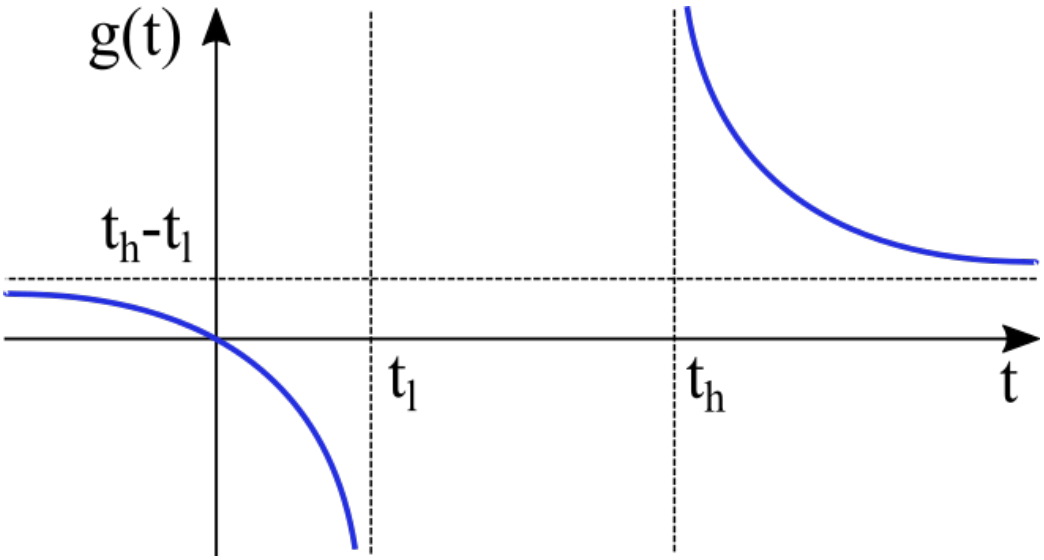

Figure 3.2: Function $g(t)$ in traced by the blue line with respect to nanoslit selectivity (t).

3.4 Non-linear Transport in the Nanoslit

The nanoslit selectivity expressed in equation 3.21 depends on the concentration gradient across the nanoslit and the potential difference that develops as a consequence of the nanoslit flux. This implicit coupling between the selectivity and the potential difference gives rise to the non-linear transport characteristic that is observed when dealing with liquids at the nanoscale. Understanding the evolution of the selectivity with respect to the parameters in eq. 3.21 provides us with the framework to optimize the nanofluidic exchanger.

We first note that the equation 3.25 determining the selectivity has a well-defined root for all values of c_h, c_l and $\Delta\Psi$. This is shown by plotting the function $g(t) = t\dfrac{t-t_l}{t-t_h}$ as a function of t in figure 3.2.

This function has the following properties:

- The function $g(t)$ passes through the origin as $g(t) = 0$ when $t = 0$.

As a consequence, the current delivered by the nanoslit vanishes for $\Delta\Psi = \mathcal{E} - (t_h - t_l)$. The interval in electrical potential useful for the slit to act as a power generator will thus be $\Delta\Psi \in [0, \mathcal{E} - (t_h - t_l)]$.

- As $\sigma < 0$ and $c_h > c_l$, $Du_l > Du_h$ and $t_l < t_h$. The function $g(t)$ is not defined in the interval $t \in [t_l, t_h]$, therefore selectivities in this interval are never obtained.

  More specifically, when the Dukhin numbers are high $Du_l > Du_h \gg 1$ (in practice $Du_h > 5$ is enough), we have $t_h \simeq t_l \simeq 1$. In this case, if $t \neq 1$ the logarithm term in eq (3.25) vanishes, which does not accommodate the right side of the equation if the latter is not zero. Therefore, at high Dukhin numbers the selectivity is close to perfect $t \simeq 1$, except in the cases where $\Delta\Psi \simeq \mathcal{E}$.

- When $t \to t_l^-$, $g(t) \to -\infty$ and when $t \to t_h^+$, $g(t) \to \infty$.

  This reflects the rectification property of the nanoslit under a difference of salinity gradient. For $\Delta\Psi \ll \mathcal{E} - (t_h + t_l)$ the $IV-$characteristics of the nanoslit is linear as $I \propto t_l(\mathcal{E} - \Delta\Psi)$, whereas for $\Delta\Psi \gg \mathcal{E} - (t_h + t_l)$ it has a different slope $I \propto t_h(\mathcal{E} - \Delta\Psi)$. Figure (3.3) plots a typical characteristics I versus $\Delta\Psi$.

- The value of $g(t)$ when $t \to \pm\infty$ is found, by performing a Taylor expansion of equation 3.25, to correspond to $\Delta\Psi = \mathcal{E}$.

  This value of $\Delta\Psi$ lies close to the interval of interest for using the slit as a power generator. At this value, the equation 3.27 giving the current intensity takes a undetermined form. Expanding 3.25 to the second order gives the

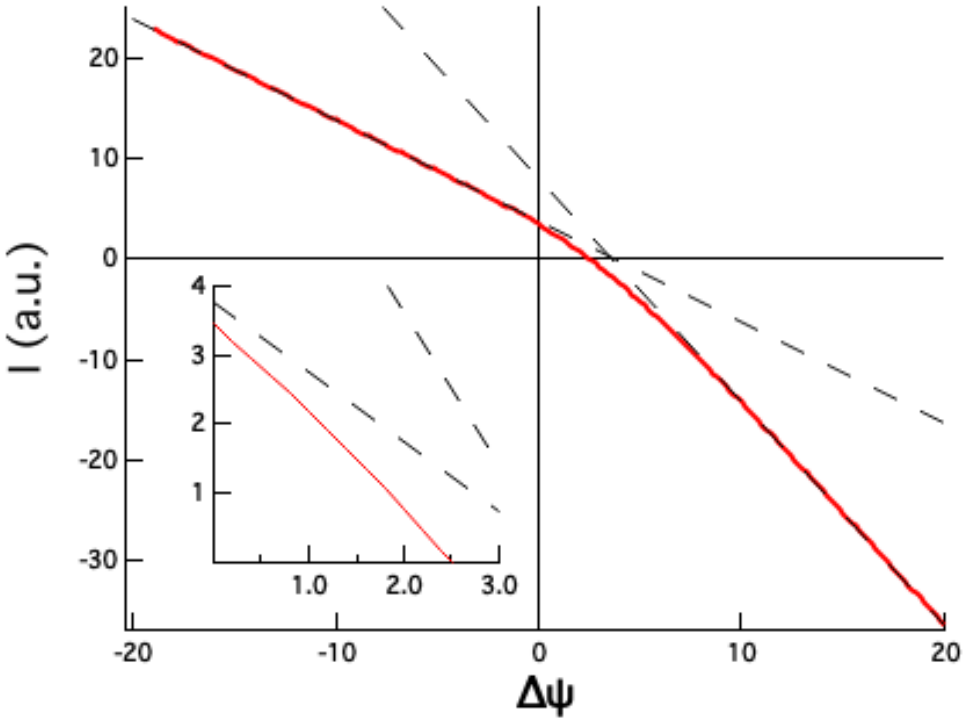

Figure 3.3: I-$\Delta\Psi$ characteristics for the Dukhin numbers $Du_h = 0.5$ and $Du_l = 10$. The inset is an enlargement of the $I > 0$ and $\Delta\Psi > 0$ portion of interest for power generation. The value of the parameter $\mathcal{E}$ is 2.88.

following value for the current generated per unit length of the slit:

$$I = -\frac{De^2H^2}{W(-\sigma)}(c_h^2 - c_l^2)$$

Numerically when the value of $\Delta\Psi - \mathcal{E}$ is small, it is of interest to use an alternative variable v to quantify the nanochannel selectivity. This variable is defined by the following expressions:

$$v = \frac{1}{2}\ln\frac{t - t_l}{t - t_h} \qquad 2t = \left(\frac{t_h - t_l}{\tanh(v)} + t_h + t_l\right) \qquad 2tv = \Delta\Psi - \mathcal{E} + (t_h - t_l)$$

The implicit equation in the variable v is hence written as:

$$(t_h - t_l)\left(\frac{v}{\tanh(v)} - 1\right) + v(t_h + t_l) = \Delta\Psi - \mathcal{E}$$

Using the expansion $\left(\frac{v}{\tanh(v)} - 1 = v^2/3 - v^4/45\right)$, we arrive at the expression for generated current and nanochannel fluxes, per unit nanoslit length:

$$I = \frac{(-2\sigma)D}{W}\left(\frac{\mathcal{E} - \Delta\Psi - (t_h - t_l)}{2}\right)\left(t_h + t_l + (t_h - t_l)(\frac{v}{3} - \frac{v^3}{45})\right)$$
$$J^+_{nano} = \frac{(-\sigma)D}{W}\left(\frac{\mathcal{E} - \Delta\Psi - (t_h - t_l) - 2v}{2}\right)\left(t_h + t_l + (t_h - t_l)(\frac{v}{3} - \frac{v^3}{45})\right)$$

It is worth noting that the variables t_h and t_l may vary along the length of the nanoslit. However, when the convection velocity in the microchannel is very high, the microchannel concentrations are conserved equal to its inlet values, which is the regime when Sherwood number is considered infinite and we find the limiting power produced by the elemental exchanger. The upcoming section is dedicated to the quantification of this limiting power density produced by the elemental exchanger.

3.5 Limiting Power Density of the Elemental Exchanger

When the exchanger is operating in the high Sherwood regime ($Sh > 10^5$), the convection velocity of microchannel is significantly high and results to conservation of ionic microchannel concentration, equal to their inlet values. The current (I^{lim}) generated by an exchanger of length (L) at this the high Sherwood regime

is calculated from eq. 3.27 as follows:

$$I^{lim} = -\frac{2\sigma D}{W} t \int_0^L (\mathcal{E} - \Delta\Psi)\partial L = -\frac{2\sigma D L}{W} t(\mathcal{E} - \Delta\Psi) \qquad \sigma < 0 \qquad (3.28)$$

We can now derive the expression for the power (P_{elec}^{lim}) and density of power per unit surface area of the elemental exchanger (Pd_{elec}^{lim}) as follows:

$$P_{elec}^{lim} = I^{lim}\Delta V = \frac{2|\sigma|DL}{W}\frac{k_B T}{e} t\Delta\Psi(\mathcal{E} - \Delta\Psi) \qquad Du_h \neq Du_l \qquad (3.29a)$$

$$Pd_{elec}^{lim} = \frac{P_{elec}^{lim}}{2bL} = \frac{D|\sigma|}{bW}\frac{k_B T}{e} t\Delta\Psi(\mathcal{E} - \Delta\Psi) \qquad Du_h \neq Du_l \qquad (3.29b)$$

The factor $2bL$ in the above equation is the surface area of the elemental exchanger with individual microchannel width b and length L, assuming that the width of the nanoslit W is quite small compared to the microchannel width.

We can simplify the expression for the limiting power density of the exchanger by splitting it into a non-dimensional function $\mathcal{F}(c_H, c_L)$ along with a dimensional pre-factor:

$$\boxed{Pd_{elec}^{lim} = \frac{D|\sigma|}{bW}\frac{k_B T}{e}\mathcal{F}(c_H, c_L)} \qquad (3.30)$$

$$\mathcal{F}(c_H, c_L) = t\Delta\Psi(\mathcal{E} - \Delta\Psi)$$

The advantage of expressing the power density with a non-dimensional function is because the function varies only as a function of inlet microchannel concentrations and is constant for all dimensions of the exchanger. Furthermore the function $\mathcal{F}(c_H, c_L)$ can be approximated empirically as follows upto a certain value of c_H:

$$\boxed{\mathcal{F} = \frac{1}{4}\left(\ln\left(\frac{c_H}{c_L}\right)\right)^2} \qquad c_H < 5\ [\mathrm{M}] \qquad (3.31)$$

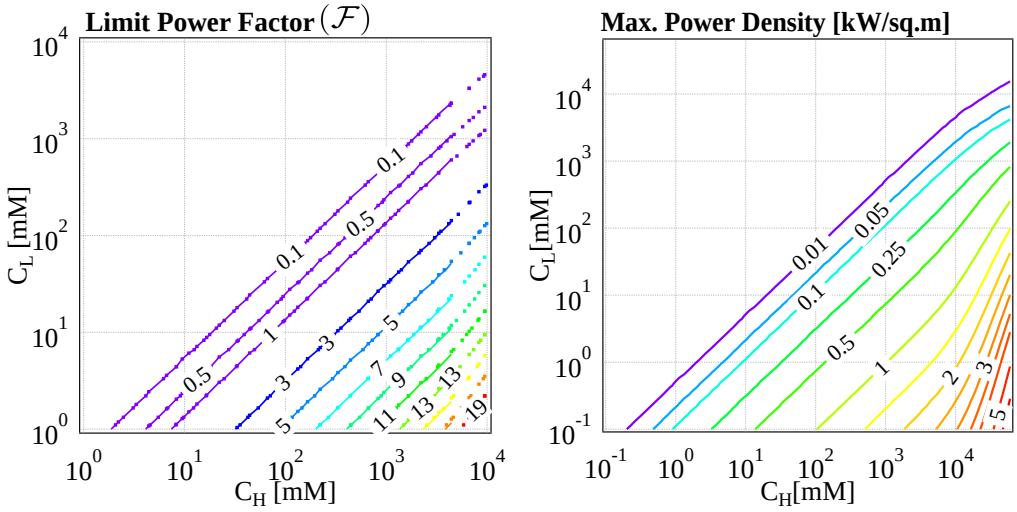

(a) (b)

Figure 3.4: (a) Value of the non-dimensional factor $\mathcal{F}$ giving the maximum power extractable from the elemental exchanger, as a function of the entrance microchannel concentrations c_H and c_L, from eq. 3.31. The straight lines are approximated value $(\ln c_H/c_L)^2/4$. (b) Maximum power density generated by the elemental exchanger, when uniform electrolyte concentrations c_H and c_L are maintained through the whole microchannels. The surface charge of the nanochannel is $\sigma = -0.64\text{Cm}^{-2}$, its height is $H = 1\text{nm}$ and width $W = 100\text{nm}$. The microchannels have a square cross-section $a = b = 2\mu\text{m}$ and the exchanger length is equal $L = 100\mu\text{m}$.

where c_H and c_L are the inlet concentrations in the microchannels. Figure 3.4a describes the variation of function $\mathcal{F}$ for different values of Dukhin numbers at the inlet of the microchannel. The straight lines in fig. 3.4a are the approximated values using the eq 3.31. Figure. 3.4 is the dimensional power per unit exchanger surface, which is capable of reaching several kilowatts per square meter of area it occupies.

Figure 3.4a allows us to estimate the limit energy generation capacity of the exchanger for any given dimension. We discussed two sets of dimensions in the previous chapter, first set achievable from the current development in the silicon fabrication technology and the second being the ideal dimensions for the elemen-

tal exchanger. The dimensions were the following:

$$L = 100\mu\text{m} \qquad a = b = 2\mu\text{m} \quad H = 1\text{nm} \quad W = 100\text{nm} \tag{3.32a}$$

$$L = 10\mu\text{m} \qquad a = b = 500\text{nm} \quad H = 1\text{nm} \quad W = 20\text{nm} \tag{3.32b}$$

For the first set of "achievable" dimensions, we find that the dimensional pre-factor takes a value of 82.7 W.m^{-2}. Taking the concentration of seawater to be equal to 600 mM and the river water concentration as 1 mM, from figure 3.4a we get $\mathcal{F} = 9$. This equates to a limit power of 745 W.m^{-2}, which is higher than any theoretical model to date. Similarly with the ideal case dimensions, we find that the pre-factor takes a value equal to 1.65kW.m^{-2} that equates to the limiting power density of 15 kW.m^{-2}.

Achieving this high density of power, however, is subject to the optimization of feeding the liquids into the exchanger. Running the exchanger with such high microchannel convection velocities will require a tremendous amount of hydrodynamic energy which will result to a very low net power gain from the system. Hence it is essential to analyze the net generated of electrical power which is equal to the difference in the electrical power generated by the exchanger to the hydraulic power dissipated in running fluids inside the exchanger, which is elaborated in the next chapter of this manuscript.

3.6 Conclusions and Perspectives

The results from this chapter indicate the source of non-linear dynamics observed at the nanometric length scales. In the context of the elemental exchanger, the surface charge over the nanoslit σ plays a vital role in the determination of the nanoslit selectivity (t), which in-turn decides the magnitude of the diffusive flux

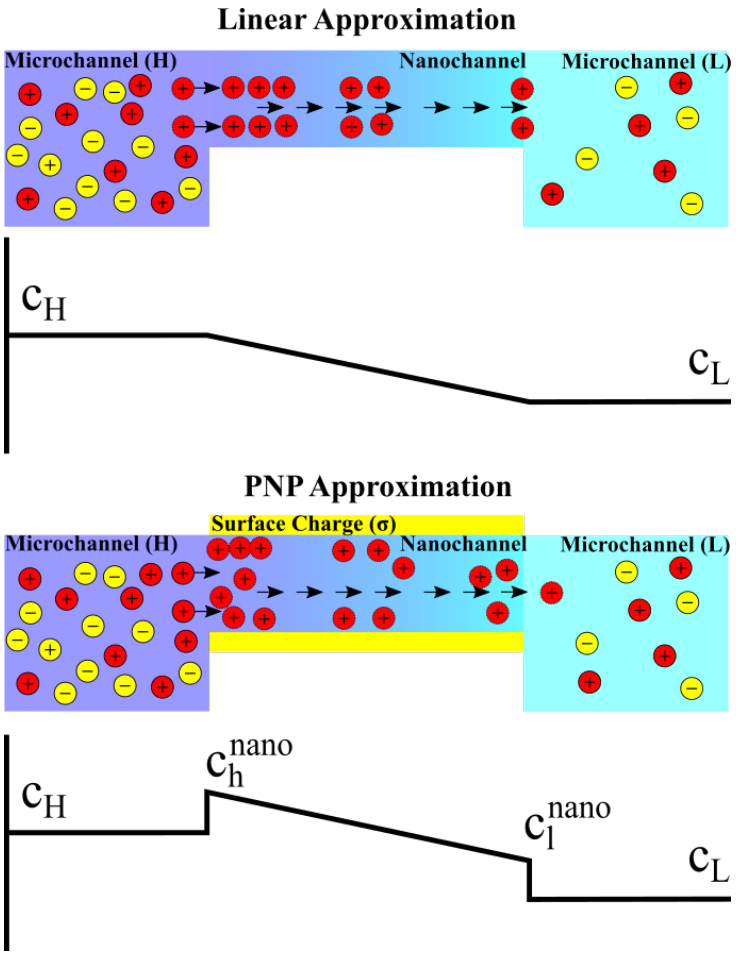

Figure 3.5: Comparison of the concentration profile in the nanoslit as cations pass through it.

($J^{\pm}_{nano}$) passing through the nanoslit. It is also observed that the driving potential inside the exchanger ($\Delta\Psi$) is implicitly coupled with the nanoslit selectivity and is governed by equation 3.21. Hence it can be concluded that the presence of surface charge over the nanoslit surface is the root of the non-linear dynamics occurring in the system and its coupling with the driving potential leads to the amplification of the diffusive flux we observe when compared to the linear model.

Fig. 3.5 compares the transport inside the nanoslit under linear approximation we used in the previous chapter with the PNP approximation. Under linear approx-

imation the concentration drops linearly across the nanoslit bridging the concentrations between microchannels. Under PNP approximation, the concentration of charges is highest at the nanoslit entrance and drops to its lowest instantaneously as it enters the low concentration microchannel.

The most encouraging result of this chapter is the estimation of the limit power density that can be generated by the elemental exchanger. We obtained a power density of 745 W/sq.m for an exchanger has the 'achievable' dimensions and can be fabricated given the development of silicon fabrication industry to date. This result is the highest density of power obtained for any technology focusing on Blue energy harvesting and may prove to be a paradigm shift in the technology. Achieving such high power however is not optimal as an immense amount of hydrodynamic cost has to be spent to operate the exchanger at such high regimes of Sherwood number. Therefore, the next chapter focuses on selecting an intermediate Sherwood regime to extract maximum net energy form the exchanger, and optimize the exchanger dimensions to maximize this net power.

CHAPTER 4

Multi-Scale Dynamics inside the Elemental Exchanger

4.1 Introduction

This chapter focuses on the quantisation the electrical power the elemental exchanger (Chapter-2, section 2.2) generates per unit surface it occupies. In Chapter 3, we showed that the maximum power density that could be theoretically achieved in the silicon-based elemental exchanger is in the order of several hundred watts per square meter, which is substantially higher than the state of the art of various membrane based processes focusing on harvesting of Blue energy like Pressure Retarded Osmosis (PRO - 6.5 W/sq.m[79]) and Reverse Electro-dialysis (RED - 6.7 W/sq.m[83]). However this estimation neglected the effect of convection in the microchannels, the boundary layers inside them, as well as the hydraulic energy cost to operate the device. This chapter introduces these effects with an increasing degree of complexity. We aim to elaborate and extend our understanding toward the first realization of a silicon-based exchanger with an optimized geometry and operating conditions for the recovery of saline gradient energy.

The calculation of the electrical power is performed by modelling the continuum dynamics in the microchannels with an advection-diffusion equation (eq. 2.2), while feeding these microchannels with a cation and anion 'line-source' using the expressions of nanoslit fluxes derived in Chapter - 3 (eq. 3.24). This is performed using the *COMSOL Multiphysics* software.

COMSOL uses a finite element solver and provides a convenient platform for simulation of this system as it allows the development of the model from 1D to 3D with a step-wise increase in complexity. Hence moving from a simple model to a robust full-scale module of exchanger is facilitated easily through the intuitive user-interface of the software. However, since *COMSOL* doesn't have a module for nanofluidics developed yet, we rely on the so-called "equation-based modelling" to develop our exchanger. This chapter elaborates on the methodology used in the development of our model, supported by *COMSOL*. We then present the study of a 1D model, based on the approximation that the mixing in the microchannels is perfect, and quantify the effect of the replenishing velocity on the maximum power density harvested by the elemental exchanger.

A section of this chapter is dedicated to the calculation of net electrical power output of the exchanger per unit surface. The net power is equal to the difference in the output power of the exchanger and the power consumed by the exchanger as a consequence of running fluids inside the microchannels. This section proposes an optimization scheme for the geometrical sizes of the microchannels and the nanoslit, and establishes the convection velocity (Sherwood number) required for the efficient functioning of the exchanger, which serve as the basis for the designing of 3D architecture of the parallelized exchanger, elaborated in the last chapter of this thesis.

The final section of this chapter presents first results of the 3D model of the elemental exchanger, also simulated using *COMSOL*.

4.2 Governing Equation for the Elemental Exchanger

4.2.1 Advection-Diffusion in the Microchannels

Figure 4.1 illustrates the schematic of the elemental exchanger, which consists of two microchannels carrying fluids of different ion concentrations, separated by a cation selective nanoslit that runs in between the microchannels.

We present here the three-dimensional governing equations used to model the concentration fields $c_h(x, y, z)$ and $c_l(x, y, z)$ in the high-concentration and low-concentration microchannels. The transport in the nanoslit is not resolved spatially, we use the expressions for the fluxes derived in Chapter 3 as a line-source/sink in the microchannels.

As the microchannels have the same geometry (see figure 4.1), with a plane of symmetry lying in their middle along their axis, we restrict our domain to half of a microchannel, of width b and heigth a. The z-direction lies along the axis of the microchannel, the x-direction is transverse to the microchannels, and the y direction is normal to the microchannels cover. For the sake of simplicity, we use a different x-axis in each microchannel, with an origin located at the micronanoslit junction, and a direction oriented away from this junction. Thus, the cation flux received in each microchannel from the nanoslit is written as $\pm J^+_{nano}(z)\delta(x, y)$ where J^+_{nano} is a flux per unit length, $\delta(x, y)$ is the 2D Dirac function, and the sign "$+$" holds for the low-concentration microchannel while the sign "$-$" holds for the high-concentration microchannel. The anion flux has a similar expression.

As discussed in Chapter 2, we consider that the electrodes are ideal, maintain a uniform potential respectively V_H and V_L in each microchannel, and exchange

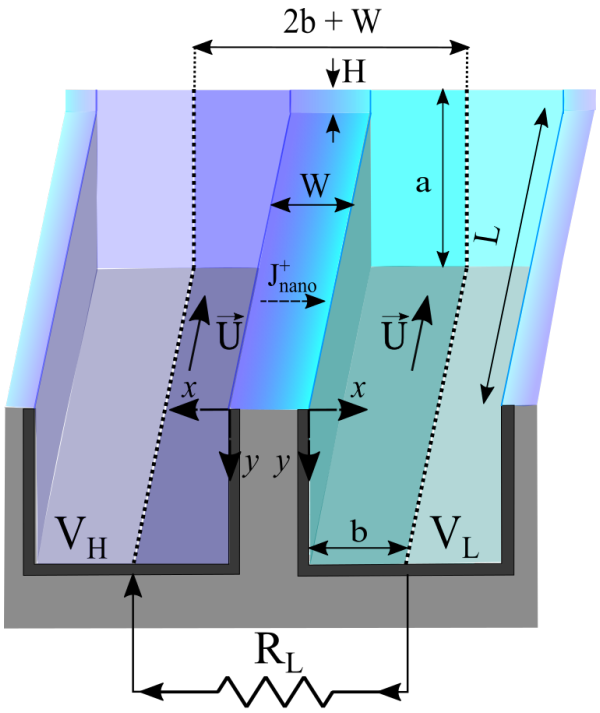

Figure 4.1: Isometric view of the elemental exchanger (represented by dotted lines). Microchannels have a cross-section of $a \times b$ and length L. They carry fluids with a convection velocity $\vec{U}$ along their length, which defines the z-axis. The faces of the microchannels are covered with electrode materials which maintain the potential of V_H, V_L in the high and low concentration microchannels respectively. The nanoslit runs along the length of the microchannel and has a height H in the y direction. The nanoslit is made cation-selective by coating its top and the bottom face with a negative surface charge with density σ per unit nanoslit surface. J^+_{nano} and J^-_{nano} are the ionic fluxes per unit length that pass through the nanoslit in the x direction, defined locally starting at the corner of the microchannels.

only anions. Under these conditions the transport of ions inside the microchannels satisfies the advection-diffusion (eq. 2.2):

$$D\Delta c_l - \vec{U} \cdot \vec{\nabla} c_l = -J_S(z)\delta(x, y) \tag{4.1a}$$

$$D\Delta c_h - \vec{U} \cdot \vec{\nabla} c_h = J_S(z)\delta(x, y) \tag{4.1b}$$

where J_S is the salt flux per unit length through the nanoslit and the rest of the parameters hold their original definition. Following the analysis in Chapter- 3, we write the expression for the salt flux as:

$$J_S(z) = J^+_{nano}(z) = -\frac{D\sigma}{eW}(1 + t(z))(\mathcal{E}(z) - \Delta\Psi) \tag{4.2}$$

where $t(z)$ and $\mathcal{E}(z)$ are the nanoslit selectivity and electro-motive force given by the equations 3.21, 3.16:

$$\mathcal{E} = \ln \frac{c_h(0,0,z)(1 + t_l(z))}{c_l(0,0,z)\big(1 + t_h(z)\big)} + t_h(z) - t_l(z) \tag{4.3a}$$

$$t_{h,l}(z) = \sqrt{1 + \frac{c^2_{h,l}(0,0,z)e^2H^2}{4\sigma^2}} \tag{4.3b}$$

$$t \ln\left(\frac{t - t_l(z)}{t - t_h(z)}\right) = \Delta\Psi - \mathcal{E} + (t_h(z) - t_l(z)) \text{ if } \quad c_l(0,0,z) \neq c_h(0,0,z) \tag{4.3c}$$

$$t = t_l(z) = t_h(z) \text{ if } \quad c_l(0,0,z) = c_h(0,0,z) \tag{4.3d}$$

where $\Delta\Psi = e(V_L - V_H)/k_BT$ is the normalized potential difference. It is assumed here that the diffusivity of the cations and the anions is equal to their average diffusivity (*D*) for the sake of simplicity of the expression.

We have not considered the effect osmotic volume flux through the nanoslit in the present analysis, hence the velocity field $\vec{U}$ in the microchannels is only due to the driving pressure, and the average velocity through the section is invariant along the z-axis. We do not take the entrance effects through the fluidic feeding ports into consideration either, and therefore the convection velocity is written as $\vec{U} = u(x,y)\vec{e}_z$.

The equations are made non-dimensional by changing the variables as follows, as done previously in Chapter - 2:

$$U = \frac{\iint u(x,y)dxdy}{ab} \qquad Pe = \frac{UL}{D} \qquad J = \frac{HL^2}{Wab}$$
$$\bar{c}_{h,l} = c_{h,l}\frac{eH}{(-\sigma)} \qquad Sh = \frac{Pe}{J}$$

The equations expressed in eq. 4.1 hence take the following form:

$$\frac{L^2}{Pe}\Delta\bar{c}_l - L\frac{u(x,y)}{U}\frac{\partial\bar{c}_l}{\partial z} = -\frac{(1+t(z))(\mathcal{E}(z)-\Delta\psi)}{Sh}ab\delta(x,y) \tag{4.4a}$$
$$\frac{L^2}{Pe}\Delta\bar{c}_h - L\frac{u(x,y)}{U}\frac{\partial\bar{c}_h}{\partial z} = \frac{(1+t(z))(\mathcal{E}(z)-\Delta\psi)}{Sh}ab\delta(x,y) \tag{4.4b}$$

Note that the term '$ab\delta(x,y)$' has no dimension as the two-dimensional Dirac function has the dimension [length]$^{-2}$.

4.2.2 Boundary Conditions

The boundary conditions on the faces of the microchannels parallel to the $z-$direction correspond clearly to a zero-flux of concentration on the faces $x = 0$, $y = 0$ and $y = a$. Since the velocity also vanishes on these faces, we can write:

$$\vec{\nabla}\bar{c}_{h,l}\cdot\vec{e}_x = 0 \quad \text{at } x = 0$$
$$\vec{\nabla}\bar{c}_{h,l}\cdot\vec{e}_y = 0 \quad \text{at } y = 0 \text{ and } y = a$$

The condition of symmetry on the face $x = b$ is written as:

$$\vec{\nabla}\bar{c}_{h,l}\cdot\vec{e}_x = 0 \quad \text{at } x = b$$

The conditions developed in Chapter - 2 for the boundary conditions on the faces

$z = 0$ and $z = L$ are not modified by the non-linear character of the exchange through the nanoslit. Therefore, we have a condition of purely convective flux in $z = L$:

$$\vec{\nabla}\bar{c}_{h,l} \cdot \vec{e}_z = 0 \quad \text{at } z = L$$

Additionally to account for the condition of global imposed flux at $z = 0$, we have:

$$\int_0^a \int_0^b \left(u(x,y)\bar{c}_{h,l}(x,y,0) - D\vec{\nabla}\bar{c}_{h,l} \cdot e_z \right) dxdy = Uc_{H,L} \qquad \text{at } z = 0$$

4.2.3 Electrical Power and Power Density

The current generated in the elemental exchanger is quantified as:

$$I = e \int_0^L (J_{nano}^+ - J_{nano}^-)\partial z \tag{4.5}$$

Substituting the value of the nanoslit fluxes from the previous chapter (eq. 3.27), we get:

$$I = -\frac{2D\sigma}{W} \int_0^L t(z)(\mathcal{E}(z) - \Delta\Psi)\partial z \tag{4.6}$$

with the parameters $t(z)$ and $\mathcal{E}(z)$ defined in equation 4.3.

The expression for the harvested electrical power (P_{elec}) is hence:

$$P_{elec} = I\Delta V = -\frac{2D\sigma}{W}\frac{k_B T}{e}\Delta\Psi \int_0^L t(\mathcal{E} - \Delta\Psi)\partial z \tag{4.7}$$

The surface area of the elemental exchanger is approximately equal to product of the width of two microchannels ($2b$) and the length of the exchanger (L), considering that the width of the nanoslit is very small compared to that of the microchannel. Therefore the electrical power generated by the exchanger per unit

surface (Pd_{elec}) is calculated as:

$$Pd_{elec} = \frac{P_{elec}}{2bL} = -\frac{D\sigma}{bLW}\frac{k_B T}{e}\Delta\Psi \int_0^L t(\mathcal{E} - \Delta\Psi)\partial z \tag{4.8}$$

The maximum generated power density, obtained for an appropriate value of the load resistance R_L, is calculated using the following expression:

$$Pd_{elec}^{max} = -\frac{D\sigma}{bLW}\frac{k_B T}{e}\max_{\Delta\Psi}\{\Delta\Psi \int_0^L t(\mathcal{E} - \Delta\Psi)\partial z\} \tag{4.9}$$

For convenience, we split the expression of the the maximum power density into a dimension part and a non-dimensional part as follows:

$$\boxed{Pd_{elec}^{max} = \frac{D|\sigma|}{bLW}\frac{k_B T}{e} f(Sh, J, Du_H, Du_L)} \tag{4.10}$$

$$f = \max_{\Delta\Psi}\left(\Delta\Psi \int_0^L t(\mathcal{E} - \Delta\Psi)\partial z\right) \tag{4.11}$$

It is expected that at infinitely high driving velocity, the nominal injected electrolyte concentrations c_H and c_L fill the microchannels completely, so that the limit value of the factor f at infinite Sherwood should meet the factor $\mathcal{F}(Du_H, Du_L)$ studied in Chapter 3:

$$\lim_{Sh\to\infty} f(Sh, J, Du_H, Du_L) = \mathcal{F}(Du_H, Du_L)$$

The objective of this chapter is to study the convergence of the factor f to its limiting value $\mathcal{F}$, to optimize the elemental exchanger geometry as well as the regime of fluid velocity inside the microchannels, to obtain the highest realistic value of the harvested power density. However, the implicit relationship between the nanoslit selectivity and the concentration gradient obstructs the development

of a purely analytical solution for the maximum power density. Hence we rely on finite element simulations to quantify them.

4.3 One-Dimensional Approximation of the Elemental Exchanger

We first implement the non-linear elemental exchanger assuming a perfect mixing of electrolyte concentration across the microchannel sections. We do not justify this approximation and consider it only as a first step toward the full scale modelling of the system.

The equations of transport in this 1D approximation are obtained by averaging the 3D equations presented in eq.4.4, on section ab of the microchannels. We introduced parameters called *Dukhin numbers* in the previous chapter to represent the normalized concentrations in the microchannel as:

$$\bar{c}_{l/h} = -\frac{eH}{\sigma} \qquad c_{l/h} = \frac{1}{Du_{l/h}} \tag{4.12}$$

The governing equation for the elemental exchanger is hence written as:

$$-\frac{1}{Pe}\frac{\partial^2 \bar{c}_l}{\partial z^2} + \frac{1}{L}\frac{\partial \bar{c}_l}{\partial z} = +\frac{1}{L^2 Sh}(1+t)(\mathcal{E} - \Delta\Psi) \tag{4.13a}$$

$$-\frac{1}{Pe}\frac{\partial^2 \bar{c}_h}{\partial z^2} + \frac{1}{L}\frac{\partial \bar{c}_h}{\partial z} = -\frac{1}{L^2 Sh}(1+t)(\mathcal{E} - \Delta\Psi) \tag{4.13b}$$

The boundary conditions for the governing equations are exactly the same as in Chapter - 2:

$$\frac{\partial \bar{c}_{h,l}}{\partial z}|_{z=L} = 0 \qquad \bar{c}_{h,l}(z=0) - \frac{L}{Pe} \qquad \frac{\partial \bar{c}_{h,l}}{\partial z}|_{z=0} = \bar{c}_{H,L} \tag{4.14}$$

This governing equation is solved with some minor simplifications (detailed later in this chapter) using *COMSOL Multiphysics* software to find the local ion concentration along the each microchannel, for a given geometry and prescribed values of injected concentrations (c_H and c_L), potential difference, and Sherwood number. Once the concentration fields are obtained, the power density is calculated using eq. 4.8.

4.3.1 Implementation in *COMSOL*

COMSOL Multiphysics is a Finite Element Solver for Partial Differential equations (PDEs), which relies on the simulation geometry to be split into numerous “nodes". These nodes are geometrical domain elements where the field(s) to be solved are approximated using piece-wise function sets (linear, quadratic or polynomial) leading to solutions of the linearized PDEs. The continuity of the approximated fields has to be ensured between the adjacent nodes such that the PDE is turned into a set of linear equations relating the coefficients describing the approximate solution.

COMSOL does not have a developed nanofluidics module yet, therefore, we rely on the so-called "equation based modelling" to solve the partial differential equations (eq. 4.13) with their boundary conditions similar to the ones formulated earlier in the chapter. For the sake of reproducibility we give the full details of the *COMSOL* implementation in the appendix chapter - A, and present only the main lines of the numerical resolution in this section.

General Form Partial Differential Equation

The simulation geometry for our 1D model is just a straight line of length L. As *COMSOL* describes domains in real space, we choose $L = 20\mu$m, without loss

of generality as our equations are homonenegous in z/L and the properties of the system depend only on the non-dimensional numbers Sh, J, Du_H, Du_L.

The governing equations (eq.4.13) are entered using the *COMSOL* feature *General Form PDE* which is focused to solve equations of the following form:

$$\nabla.\vec{\Gamma} = s \tag{4.15}$$

Simply put, the divergence of a flux 'Γ' equal to a source 's'. This is well-suited for a diffusion-convection equation. We solve for the two concentration fields $\bar{c}_h$ and $\bar{c}_l$ with a two component flux (in 1D) Γ equal to the flux in the microchannels:

$$\Gamma = \begin{bmatrix} -(\frac{1}{Pe})(\frac{\partial \bar{c}_h}{\partial x}) + \frac{1}{L}\bar{c}_h \\ -(\frac{1}{Pe})(\frac{\partial \bar{c}_l}{\partial x}) + \frac{1}{L}\bar{c}_l \end{bmatrix} \qquad s = \begin{bmatrix} -\frac{nanoj}{2L^2.Sh} \\ \frac{nanoj}{2L^2.Sh} \end{bmatrix} \tag{4.16}$$

using the boundary conditions expressed in eq. 4.14 directly.

The two-component source $s = \pm nanoj/(2L^2 Sh)$, with $nanoj$ being the implicit function $(1+t)(\mathcal{E} - \Delta\Psi)$, corresponds to the right hand side of eq. 4.13. It is calculated separately using the feature *Domain Algebraic Equations* of *COMSOL* which allows to calculate additional fields in the resolution domain from explicit or implicit algebraic equations. However, the implicit equation for the selectivity (eq. 4.3) is too singular to be solved smoothly. Hence, we use the variable 'v' as developed in Chapter 3, which we introduce and solve as a field:

$$(t_h - t_l)\left(\frac{v}{\tanh(v)} - 1\right) + v(t_h + t_l) = \Delta\psi - \mathcal{E} \qquad t_{h,l} = \sqrt{1 + \bar{c}_{h,l}^2}$$

The field v is related to the selectivity by the expression $2t = \dfrac{t_h - t_l}{\tanh(v)} + t_h + t_l$. Therefore the nanochannel flux $nanoj$ is expressed as follows for all values of

$v > 0.1$:

$$nanoj = \left(2 + t_h + t_l + \frac{t_h - t_l}{\tanh(v)}\right)\left((t_h - t_l)\left(\frac{v}{\tanh(v)} - 1\right) + v(t_h + t_l)\right)$$

When $v \leq 0.1$ the above expressions are a bit troublesome, hence we rectify it using Taylor expansion to approximate the value of the hyperbolic tangent:

$$\frac{1}{\tanh(v)} = \frac{1}{v} + \frac{v}{3} - \frac{v^3}{45} \quad ; \quad \frac{v}{\tanh(v)} - 1 = \frac{v^2}{3} - \frac{v^4}{45} \qquad v \leq 0.1 \qquad (4.17)$$

In this case $nanoj$ for $v \leq 0.1$ is expressed as:

$$nanoj = \left(1 + \frac{v^2}{3} - \frac{v^4}{45}\right)\left(t_h - t_l + (t_h + t_l + 2)\tanh(v)\right)\left((t_h - t_l)\left(\frac{v}{3} - \frac{v^3}{45}\right) + t_h + t_l\right)$$

Meshing

It is found that the concentrations vary extremely quickly at the entrance in the microchannel, at $z = 0$. Therefore it is important to ensure a very fine meshing at this location. The fore we enforce *COMSOL* to have 100 elements between $z = 0$ and $z = 0.1$, and choose a predefined "finer" mesh for the remaining geometry. The detailed procedure for achieving this is given in the appendix.

Result Evaluations

Once the simulation is completed, the resulting values of the concentration fields and other calculated variables are stored as *Data Sets*, and the current intensity and power density can be calculated by integrating the appropriate expressions (4.5) and (4.10) over the domain $[0, L]$.

We aim at discussing the maximum power density harvested as a function of the

replenishing velocity (represented by the Sherwood number) as a function of the geometrical sizes of the Exchanger (represented by J), and the chemical characteristics of the simulation (represented by Du_H and Du_L). We obtain these results by performing a parametric sweep over two parameters $\Delta\psi$ and Sh. For a given value of Sherwood, the maximum power density as a function of $\Delta\psi$ is extracted using the feature *Operation - Maximum* of the *Data Series Operation* in the *Evaluation Group* node of *COMSOL* (see appendix chapter - A).

4.3.2 Maximum Harvested Power Density as a function of Sherwood Number

Figure 4.2 illustrates the maximum non-dimensional power density f (from eq. 4.11) as a function of the Sherwood number obtained from *COMSOL* simulations of the elemental exchanger. Figure 4.2a specifically shows the variation of $f(Sh)$ for different inlet concentration ratios $C_r = c_H/c_L \in [10, 10^5]$, an entrance Dukhin number equal to unity $Du_H = 1$, and three values of conductance ratio ($J = 1, 10, 100$).

The geometrical and chemical parameters used to generate these values of the non-dimensional numbers are given below:

$c_H = 663, 66.3, 6.63$mM	$\sigma = -0.64$C/m^2	$L = 20\mu$m
$H = 1$nm	$W = 20$nm	$b = 1\mu$m
$a = \dfrac{HL^2}{JbW}$	$U = \dfrac{DHLSh}{Wab}$	$Pe = JSh$

Figure 4.2b reports the influence of the entrance Dukhin number and plots $f(Sh)$ for $Du_H = 1, 10, 100$ and $J = 10$.

The most significant findings from the simulations can be summarized as follows:

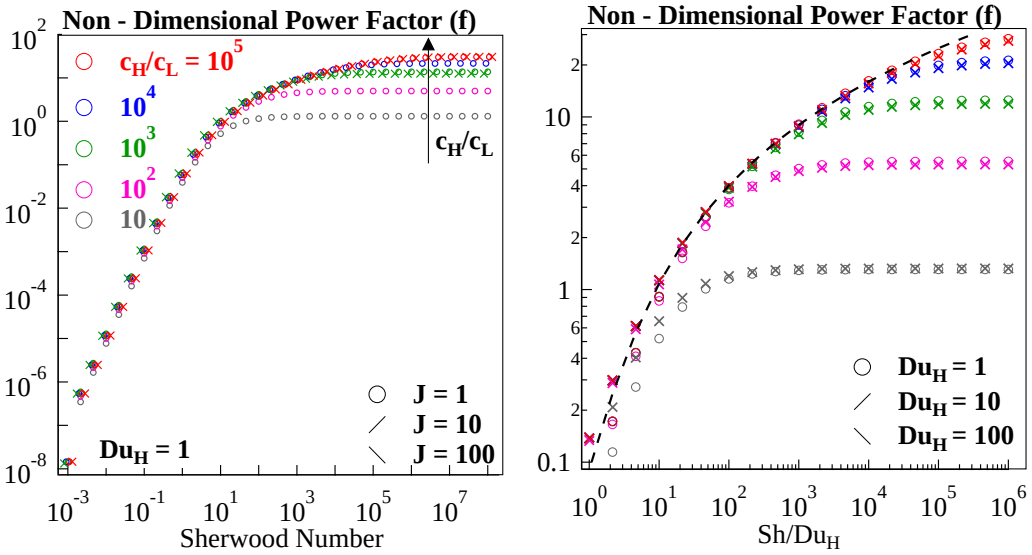

(a) (b)

Figure 4.2: (a) Non-dimensional electrical power density f (eq. 4.11) plotted as a function of Sherwood number for entrance Dukhin number $Du_H = 1$. Concentration ratios $Cr = 10, 10^2, 10^3, 10^4, 10^5$ are plotted for conductance ratio $J = 1$. For $J = 10, 100$ function f is plotted for concentration ratio $Cr = 10^3, 10^5$. (b) Non-dimensional electrical power density f plotted as a function of Sh/Du_H for five concentration ratios and $Du_H = 1, 10, 100$ and $J = 10$. The black dashed line is the master curve shown in eq. 4.18.

- **The three distinct regimes in Sherwood**: The three regimes in Sherwood seen under the linear approximation of nanoslit flux in Chapter - 2 (fig. 2.4) are visible here as well.

- **Limit power density**: The factor f converges to the value $\mathcal{F}$ studied in Chapter 3. In contrast to the linear exchanger studied in Chapter 2, this maximum depends on the concentration ratio, most often as $(\ln Cr)^2/4$, as shown in Chapter 3.

- **Conductance ratio J does not play a major role in the value of f**: As observed in Chapter 2, we find that the role of J is very limited in the determination of the power density. It does not impact the transition to the

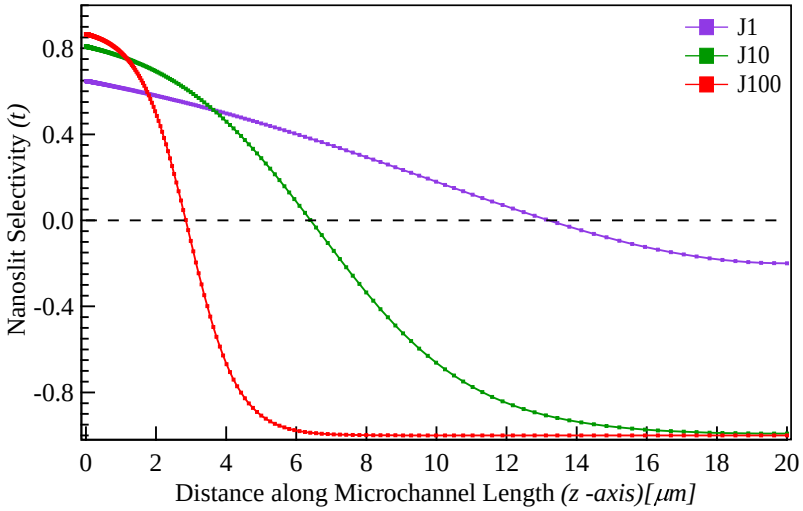

Figure 4.3: Nanoslit selectivity (t) varies along the microchannel length (μm)considerably at low Sherwood numbers. The plot corresponds to an entrance $Du_H = 1$, $Cr = 10^3$, $J = 1, 10, 100$, $L = 20\mu$m and $Sh = 0.01$. The data is plotted at $\Delta V = 0.25$mV, which is the potential difference at which the maximum value of f is obtained for all three values of parameters J. This variation is responsible for the difference in scaling in observed between the linear toy-model (f_{toy}) and the realistic model (f) at low Sherwood regime.

infinite Sherwood (see below), neither the very low Sherwood regime.

- **The function f scales as $f \approx (Sh^2/8)$ in the low Sherwood regime**: This is found empirically from the data and does not depend on the value of parameter J.

  The low Sherwood behaviour in the linear toy-model of Chapter 2 was also found to be independent of J, however the scaling in Sherwood was different, in $Sh/8$. The low Sherwood behaviour found here is thus due to the non-linear character of the ion exchange in the nanoslit. More specifically, this scaling is due to the fact that the value of the selectivity is not enforced to $t = 1$ as in the toy model, but is determined by more realistic characteristics of ion transport between charged solid surfaces. At very low Sherwood

we find that the value of t in a significant part of the exchanger reaches the value -1, corresponding to a vanishing concentration flux through the nanoslit. This is consistent with a spatially uniform value of the concentration fields $c_h(z)$ and $c_l(z)$ expected far from the entrance of the exchanger under very low convection velocity. However the value $t = -1$ corresponds also to an counter-flux of anions through the nanoslit, and thus a negative value of the electrical current, and of the harvested power. Therefore, the condition for maximizing the power is a balance between the power generation at the entrance in the exchanger, and the power loss in the rest of the exchanger, leading to a significantly lower performance of the non-linear exchanger at low Sherwood than the toy-model. Figure 4.3 illustrates the variation of nanoslit selectivity t for entrance $Du_H = 1$ at $Sh = 0.01$ and $\Delta V = 0.25$mV, which is the potential where the power density is maximum. The remaining geometrical and chemical parameters remain the same as mentioned in the beginning of this section.

- **Extended transition region**: We notice that the value of the Sherwood number required to reach the plateau of maximum power, is much larger than in the linear exchanger of Chapter 2, and increases with the inlet concentration ratio. For instance a value $Sh = 10^4$ is needed to reach the plateau value of f at a concentration ratio $C = 1000$.

  This regime in Sherwood number is the one of interest for maximizing the capability of the elemental exchanger as a high power density generator. Figure 4.2b gathers all the data obtained at $Sh \geq 1$ for various values of the concentration ratios $Cr \geq 20$, entrance Dukhin $Du_H \geq 1$ and conductance ratio $J = 10$. In this figure the power density is plotted as a function of Sh/Du_H. We find that all the data in the transition region gather on a single master curve, and they essentially leave this master curve only when

reaching the plateau value $\mathcal{F} \simeq (\ln Cr)^2/4$ corresponding to the concentration ratio.

Empirically we find that this master law is well described by the expression

$$\boxed{f \simeq \left[\log\left(1 + \frac{Sh}{Du_H}\right)\right]^2} \tag{4.18}$$

which is plotted in dashed line on figure 4.2b.

4.4 Maximum Net Power Density generated by the 1D Exchanger

4.4.1 Hydraulic Dissipation in the Exchanger

Since the exchanger cannot be operated at an infinitely high Sherwood number in order to reach the limiting power density, and it is of importance to consider the hydraulic losses needed to replenish the electrolyte concentrations in the microchannels.

The hydraulic power dissipated by the exchanger per unit surface (Pd_{hyd}) can be calculated as the product of the pressure drop in the microchannels (ΔP_μ) and with the microchannel flow rate in the two microchannels (Q_μ). The pressure drop in microchannel is given by Plane - Poiseuille equation[77] as:

$$Pd_{hyd} = \Delta P_\mu Q_\mu \qquad \Delta P_\mu = \frac{K\eta LU}{4}\frac{(a+2b)^2}{a^2b^2} \qquad Q_\mu = (2ab)U \tag{4.19}$$

The symbols "a, b" are the depth and the width of a single microchannel in the elemental exchanger, η is the dynamic viscosity and K is the friction factor that

varies with the aspect ratio (b/a) of the microchannel:

$$K\left(\frac{2b}{a} < 0.7\right) = \frac{12}{(1+2b/a)^2(1-0.63b/a)} \qquad K\left(\frac{2b}{a} = 1\right) = 7.11 \quad (4.20)$$

Expressing the convection velocity in terms for Sherwood number (eq. 2.6), the hydraulic power density take the following expression:

$$Pd_{hyd} = \frac{D^2H^2L^2(a+2b)^2K\eta}{4W^2a^3b^4}Sh^2 \quad (4.21)$$

Hence from equations 4.10 and 4.21, we find the expression of net power generated from the elemental exchanger as follows:

$$\boxed{Pd_{net} = \frac{Dk_BT|\sigma|}{ebW}\left(f - \frac{KD\eta eH^2L^2(a+2b)^2}{4k_BT|\sigma|Wa^3b^3}Sh^2\right)} \quad (4.22)$$

4.4.2 Optimization of the Net power Density Extracted

It can be seen from the equation 4.21 that the dissipated power grows with the square of Sherwood number and whereas the function f varies depending on the regime of convection velocities. It can also be seen from fig. 4.2 that the net power density is expected to produce a maximum at the intermediate Sherwood regime, as the electrical power is too low at low Sherwood numbers and the hydraulic dissipation is massive at high Sherwood numbers. This section is dedicated to the maximization of the net power produced by the exchanger for a given values of nanoslit surface charge and inlet concentration using the empirical function of f (eq. 4.18).

If we consider the microchannels to have a square cross section *i.e* $a = 2b$ with

$K = 7$, the expression for the net power density reduces to:

$$Pd_{net} = \frac{Dk_BT|\sigma|}{ebW}\left(f - \frac{7D\eta eH^2L^2}{2k_BT|\sigma|Wb^4}Sh^2\right) \tag{4.23}$$

The geometry of the exchanger is optimized by keeping the ratio of the microchannel length (L) to its width (b) constant and equal to "λ". The height of the nanoslit can also be expressed as a function of the initial concentration (c_H) and Dukhin number (Du_H):

$$L/b = \lambda \qquad H = \frac{|\sigma|}{ec_HDu_H} \tag{4.24}$$

At this point, to further reduced the expression for the net power, we introduce a volume $\mathcal{V}$ and coefficient $\bar{P}$:

$$\mathcal{V} = \frac{7D\eta|\sigma|}{k_BTec_H^2} \qquad \bar{P} = \frac{k_BTD|\sigma|}{e} \tag{4.25}$$

The net density of power now takes the form:

$$Pd_{net} = \frac{\bar{P}}{Wb}\left(f - \frac{\mathcal{V}\lambda^2}{2Wb^2}\left(\frac{Sh}{Du_H}\right)^2\right) \tag{4.26}$$

the coefficient $\bar{P}$ is equal to 16 pW considering a nanoslit surface charge of 0.64 C/m^2 at room temperature.

The reduced expression for the net density of power (eq. 4.26) is used to determine the optimum width of the microchannel (b_{opt}) as at this width the derivative of the net power density with respect to the width "b" is equal to zero.

$$\frac{\partial Pd_{net}}{\partial b} = 0 \quad \text{at} \quad b_{opt} = \frac{Sh}{Du_H}\sqrt{\frac{3\mathcal{V}\lambda^2}{2Wf}} \tag{4.27}$$

Substituting $b = b_{opt}$ in equation 4.26:

$$Pd_{net} = \frac{2\sqrt{2}}{3\sqrt{3}} \frac{\bar{P}}{\sqrt{W\mathcal{V}\lambda^2}} \frac{Du_H}{Sh} f^{3/2} \tag{4.28}$$

At this optimum microchannel width, the electrical power produced by the exchanger is thrice as much as the hydraulic power dissipated in operating the exchanger.

The net density of power can be maximized by maximising the factor $f^{3/2}Du_H/Sh$ using the equation 4.18. Upon analysing, it seen that the maxima of the function f is reached when Sh/Du_H = 15.8 corresponding to $f_{max} = 1.5$. Hence the optimum microchannel width for maximum net power and its corresponding maximum net power is written as:

$$b_{opt} = 15.8\lambda\sqrt{\frac{\mathcal{V}}{W}} \qquad Pd_{net}^{max} = 0.063\frac{\bar{P}}{\lambda\sqrt{W\mathcal{V}}} \tag{4.29}$$

The pre-factors 15.8 and 0.063 in the expressions above are solely fixed by the value of Sh/Du_H. Replacing the factors $\mathcal{V}$ and $\bar{P}$ from eq. 4.25, we get:

$$\boxed{b_{opt} = 15.8\frac{\lambda}{c_H}\sqrt{\frac{KD\eta|\sigma|}{eWk_BT}} \qquad Pd_{net}^{max} = 0.063\frac{c_H}{\lambda}\sqrt{\frac{D|\sigma|(k_BT)^3}{7e\eta W}}} \tag{4.30}$$

The optimal value of the microchannel convection velocity can be extracted from the definition of the Sherwood number (eq. 2.6) and assuming a square cross sectional area, $S_M = 2b^2$:

$$U_{opt} = \frac{DHL}{2Wb_{opt}^2}Sh = \frac{D\lambda|\sigma|}{2eWb_{opt}Du_H} = \frac{1}{2}\sqrt{\frac{D|\sigma|k_BT}{7e\eta W}} \tag{4.31}$$

It is worth noting that the only geometrical variable which impacts the optimal

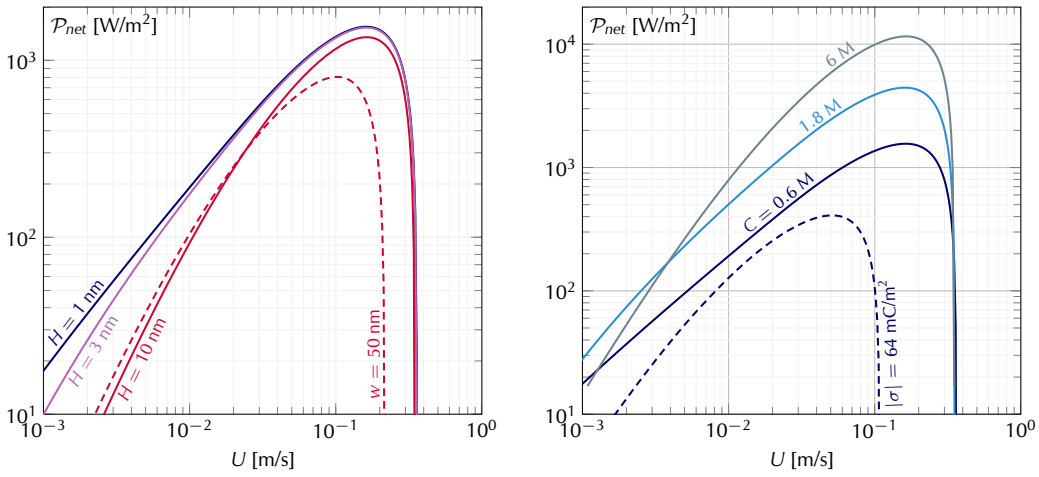

(a) (b)

Figure 4.4: Net extractable power density $\mathcal{P}_{net}$ calculated from equation 4.23, and plotted as a function of the flow velocity U in the microchannels. The diffusion coefficient is $D = 10^{-9}\mathrm{m}^2/\mathrm{s}$ and the solutions viscosity is $\eta = 1$ mPa.s. Microchannels have an optimized square section of width $2b_{opt}$ (eq. 4.30) and a length $L = 20b_{opt}$. (a) Case of sea water C_H =600 mM and fresh water C_L =1 mM. Continuous lines correspond to $W = 20$ nm (b_{opt} =500 nm) and H={1,3,10} nm. The dashed line corresponds to $H = 10$ nm and W=50 nm (b_{opt}=300 nm). (b) Case of a brine with a concentration ratio $C_H/C_L = 600$, $W = 20$ nm, and $H = 1$ nm. Continuous lines correspond to $|\sigma| = 0.64$ C/m^2 and $C_H = \{0.6M, 1.8M, 6M\}$, associated to $b_{opt} = \{500, 157, 50\}$ nm). The dashed line corresponds to $|\sigma| = 64$ mC/m^2 and $C_H = 0.6$ M ($b_{opt} = 270$ nm).

microchannel velocity is the width 'W' of the nanoslit. The pressure difference between the microchannel inlet and the outlet is hence expressed as:

$$\Delta P_{opt} = 7\eta \frac{U_{opt}\lambda}{b_{opt}} = 0.031 k_B T c_H \tag{4.32}$$

4.4.3 Analysis of Optimum Net - Power

The figure 4.4 plots the net density of power than can be extracted from the exchanger against varying convection velocity in the microchannel. The width of the microchannel (b_{opt}) is optimized to have a square cross section and the length

of the microchannel (L) is taken as 20 times the microchannel width ($L = 20b_{opt}$).

Upon analysis of the equation 4.30, it can be concluded that the main geometrical parameter in the exchanger is the nanoslit width W, which needs to be as short as possible as the maximum net power scales as with $W^{-1/2}$. This length has a significant impact on the intensity of gradients for a given difference in the salinity. The width of the nanoslit for the simulations in fig. 4.4 is chosen to be equal to 20nm and 50nm, on the basis of the state of the art in the silicon lithography industry. The dashed lines in fig. 4.4 corresponding to $W = 50$nm illustrates the drop in the power density by a factor of $1/\sqrt{W}$. In contrast to the nanoslit width, the nanoslit height (H) seems to only play a marginal role in affecting the net power for $Du_H > 1$. This limited effect of the nanoslit height can be attributed to the approximations considered in the model, with the neglecting of osmotic convection and diffusion-osmotic effects in the nanoslit. As these effects are expected to contribute positively to the generated power density, increasing the nanoslit height may lead to appreciation of the net power, once these effect are integrated in the model.

The microchannel length (L) is must also me minimized as the net power is calculated to be inversely proportional to it (eq. 4.30), but the this length is limited by the bonding requirement needed to externally feed the exchanger (elaborated in the next chapter). Hence for the simulation the factor λ (eq. 4.24) was chosen to be equal to 20.

Given the above conditions for the simulations, nanoslit width of 20 nm corresponds to an optimum microchannel width (b_{opt}) equal to 500 nm, leading to a square microchannel cross-section with a side of 1 μm and length 10 μm. The maximum net power density under these conditions reaches 1.4 kW/m^2, which is more than 100 times larger than the theoretical predictions of Yale's team[57] for the

maximum output of membranes made of nanopores of same surface charge and height, operated under same conditions of salinity.

It is noteworthy that the net power density of the optimized elemental exchanger is around 10 times less than its nominal electrical power density (fig. 3.4), which ignores hydraulic dissipation effects. This loss factor of 10 is much lower than the losses induced by concentration polarization effects in 2D membranes, estimated to be as large as 10^5 in the works of *Wang et al.*[57]. Therefore, even if the geometrical arrangement of nanopores is less favorable in microfluidic exchanger than in 2D membranes, the elemental exchanger has a higher power recovery due to the microfluidic circulation. It is also worth mentioning that the pressure head required to operate the elemental exchanger in optimal conditions depends on the osmotic pressure of the high concentration fluid (eq. 4.32). When operating with sea water with a concentration of 600 mM, the optimum pressure head is found equal to 0.5 atm, which does not raise specific operational problems in silicon based fluidic systems.

4.4.4 Feeding the Microchannels using Mesochannels

The fluids in the microchannels are fed through a multi-scale flow architecture, that is detailed in the next chapter of this manuscript. We know already from the design of the elemental exchanger that the fluid enters the microchannels from the bottom of the exchanger. The fluids are fed into the microchannel using *Mesochannels*, which have a very large sections compared to that of the microchannels. The intention is to be able to design the mesochannels such that they run perpendicular to the length of the microchannels, in the bottom plane of the exchanger, with the ability to feed multiple microchannels using one mesochannel. Figure 2.1 illustrates the positioning of the mesochannels with respect to the microchannels and also gives us an estimate of the relative size difference between

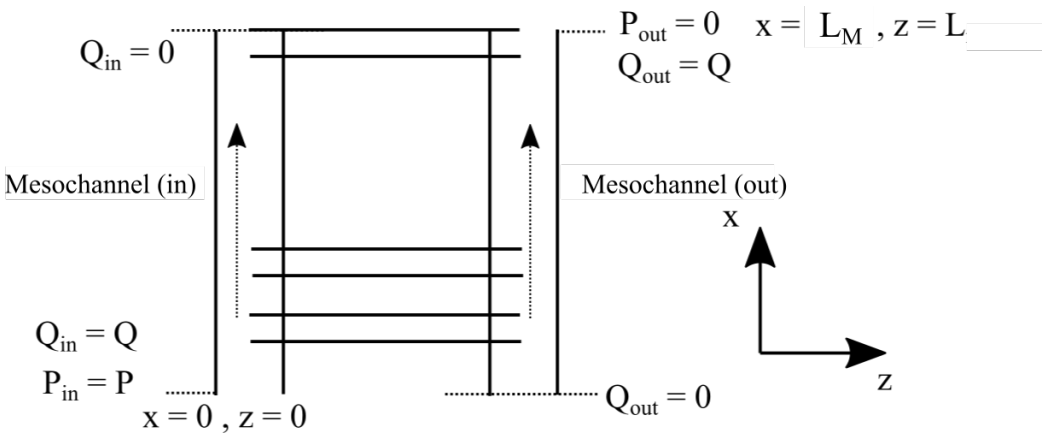

Figure 4.5: Schematic of mesochannel pressures (P_{in}, P_{out}) and flow rates (Q_{in}, Q_{out}) feeding the elemental exchanger. L_M is the total length of the mesochannel and L is the length of the elemental exchanger.

them.

The design of the mesochannel hence needs to be optimized to have a dense arrangement, avoiding hydrodynamic losses. We start this optimization by considering a flow rate ($Q_{in}(x)$) in the source-mesochannel and $Q_{out}(x)$ for the drain-mesochannel along their lengths. A schematic of the mesochannel setup is given in fig. 4.5, with the appropriate axes in the system. Considering the width of the mesochannel as b_m the flow rate in the mesochannels can be expressed as a function of the pressure drop inside them using the Hagen-Poiseuille equation[77]:

$$Q_{in} = -\mathcal{A}_M \frac{dP_{in}}{dx} \tag{4.33a}$$

$$Q_{out} = -\mathcal{A}_M \frac{dP_{out}}{dx} \qquad \mathcal{A}_M = \frac{1}{K_M \eta} \frac{(a_M b_M)^3}{(a_M + b_M)^2} \tag{4.33b}$$

here a_M, b_M are depth and width of millichannel, K_M is the mesochannel friction factor and η is the dynamic viscosity. We know that the inlet and outlet mesochannels are connected through a series of parallel microchannels. The flow rate in the mesochannel per unit mesochannel length is assumed to be constant and equal to

the microchannel flow rate per unit microchannel width (b).Hence:

$$\frac{dQ_{in}}{dx} = -\frac{dQ_{out}}{dx} = \frac{Q_\mu}{b} = -\frac{\mathcal{A}_\mu}{Lb}\big(P_{in}(x) - P_{out}(x)\big) \tag{4.34}$$

$$\mathcal{A}_\mu = \frac{1}{K_\mu \eta}\frac{(ab)^3}{a+b}$$

where K_μ is the microchannel friction factor, Q_μ is the microchannel flow rate and a, b are the microchannel depth and width respectively.

From the equations 4.33,4.34 we arrive at the following expressions:

$$Q_{in} + Q_{out} = -\mathcal{A}_M \frac{d(P_{in} + P_{out})}{dx} = Q \quad \text{[Constant]} \tag{4.35a}$$

$$\frac{d(Q_{in} - Q_{out})}{dx} = -\mathcal{A}_M \frac{d^2\Delta P}{dx^2} = -\frac{2\mathcal{A}_\mu}{Lb}\underbrace{\big(P_{in}(x) - P_{out}(x)\big)}_{\Delta P(x)} \tag{4.35b}$$

As a result we have a second order differential equation terms of $\Delta P(x)$:

$$\Delta P - \lambda^2 \frac{d^2\Delta P}{dx^2} = 0 \tag{4.36}$$

with

$$\lambda = \sqrt{\frac{\mathcal{A}_M Lb}{2\mathcal{A}_\mu}} = \sqrt{Lb\frac{K_\mu}{2K_M}\left(\frac{a_M b_M}{ab}\right)^3\left(\frac{a+b}{a_M + b_M}\right)^2} \tag{4.37}$$

We consider a square cross section for microchannel and the mesochannel and assume that the length L_M comprises of two mesochannels with a wall that is half the width of the mesochannel between them *i.e.* $L_M = 1.5b_M$. Hence the expression for lambda is written as:

$$\lambda = \frac{9}{4\sqrt{2}} L k^{3/2} \qquad k = \frac{L}{b} \tag{4.38}$$

The general solution for then differential equation (eq. 4.36) is written as:

$$\Delta P = C_1 e^{-\frac{x}{\lambda}} + C_2 e^{\frac{x}{\lambda}}$$

with C_1, C_2 being integration constants which are eqaluated using the following boundary conditions:

- At $x = 0$, $Q_{in} = Q$ and $Q_{out} = 0$. From eqs. 4.33 and 4.4.4 we can write

$$-\frac{d\Delta P}{dx}\bigg|_0 = \frac{1}{\lambda}(C_1 - C_2) = \frac{Q}{\mathcal{A}_M} \tag{4.39}$$

- At $x = L_M$, $Q_{out} = -Q$ Hence,

$$-\frac{d\Delta P}{dx}\bigg|_{L_M} = \frac{1}{\lambda}(C_1 e^{-L_M/\lambda} - C_2 e^{L_M/\lambda}) = -\frac{Q}{\mathcal{A}_M} \tag{4.40}$$

From the above boundary conditions, we can express the local pressure drop in the mesochannel in terms of the flow rate (Q):

$$\Delta P(x) = \frac{\lambda Q}{\mathcal{A}_M \sinh\left(\frac{L_M}{\lambda}\right)}\left(\cosh\frac{L_M - x}{\lambda} + \cosh\frac{x}{\lambda}\right) \tag{4.41}$$

Evaluation of mesochannel flow rate (Q)

We express the mesochannel flow rate in terms of the local pressures in source and drain mesochannel by integrating eq. 4.35a:

$$P_{in}(x) + P_{out}(x) = -\frac{Qx}{\mathcal{A}_M} + C_3$$

The integration constant C_3 is evaluated by considering the pressures at point $x = 0$, that leads to:

$$C_3 = P + P_{out}(0) \qquad P = P_{in}(0) - P_{out}(L_M) \tag{4.42}$$

We know that at $P_{out}(L_M) = 0$, hence the above equation at $x = L_M$ is written as:

$$P_{in}(L_M) = -\frac{QL_M}{\mathcal{A}_M} + P + P_{out}(0) \tag{4.43}$$

From equation 4.41:

$$\Delta P(L_M) = P_{in}(L_M) = \frac{\lambda Q}{\mathcal{A}_M \sinh\left(\frac{L_M}{\lambda}\right)}\left(1+\cosh\frac{x}{\lambda}\right) = -\frac{QL_M}{\mathcal{A}_M}+P+P_{out}(0) \tag{4.44}$$

Evaluating eq. 4.41 at $x = 0$, we get:

$$P - P_{out}(0) = \frac{\lambda Q}{\mathcal{A}_M \sinh\left(\frac{L_M}{\lambda}\right)}\left(1 + \cosh\frac{x}{\lambda}\right) \tag{4.45}$$

Solving the two equations above simultaneously, we arrive at the expression of flow rate (Q) in the mesochannel as:

$$Q = \frac{\mathcal{A}_M P}{\lambda}\left(\frac{\cosh\left(L_M/\lambda\right)+1}{\sinh\left(L_M/\lambda\right)} + \frac{L_M}{2\lambda}\right)^{-1} \tag{4.46}$$

Substituting the value of Q in eq. 4.41, we get the expression for mesochannel pressure drop (ΔP):

$$\Delta P(x) = P\left(\cosh\left(\frac{L_M}{\lambda}\right)+1+\frac{L}{2\lambda}\sinh\left(\frac{L_M}{\lambda}\right)\right)^{-1}\left(\cosh\left(\frac{L_M-x}{\lambda}\right)+\cosh\left(\frac{x}{\lambda}\right)\right)$$

This expression can be further simplified by defining a length $\chi = x - L_M/2$ as:

$$\cosh\frac{L_M - x}{\lambda} + \cosh\frac{x}{\lambda} = \cosh\frac{L_M/2 - \chi}{\lambda} + \cosh\frac{L_M/2 + \chi}{\lambda} = 2\cosh\frac{L}{2\lambda}\cosh\frac{\chi}{\lambda}$$

The final expression for mesochannel pressure drop (ΔP) is hence:

$$\boxed{\Delta P(x) = 2P\left(\cosh\left(\frac{L_M}{\lambda}\right) + 1 + \frac{L}{2\lambda}\sinh\left(\frac{L_M}{\lambda}\right)\right)^{-1}\cosh\frac{L}{2\lambda}\cosh\frac{\chi}{\lambda}} \quad (4.47)$$

This pressure reaches a minimum when $\chi = 0$ that is a factor $\cosh L/2\lambda$ smaller than the pressure difference at the extremities ($\chi = \pm L/2$) of the mesochannel. As we wish to maintain a similar flow rate in all the microchannels, we need to limit the variations in the pressure drop (ΔP) by using a limit threshold (ϵ) such that $\cosh L_M/2\lambda - 1 < \epsilon$. For example, $L_M/2\lambda < 0.5$ corresponds to $\epsilon < 0.12$.

If we consider that the length L_M of the mesochannel feeds N microchannels then we know $L_M = 2Nb$ as the distance between two microchannels carrying the same fluid is equal to $2b$, with b being the width of an individual microchannel. The factor L_M/λ is written as:

$$\frac{L_M}{\lambda} = \frac{8\sqrt{2}Nb}{9L}k^{-3/2} = \frac{8\sqrt{2}N}{9}k^{-5/2} \qquad k = \frac{L}{b}$$

The threshold above corresponds to:

$$\frac{L_M}{2\lambda} < 0.5 \quad \frac{4\sqrt{2}}{9}Nk^{-2.5} \quad (4.48)$$

Hence if we consider a value of $k = 10$, that gives the ability to feed a maximum of 500 microchannels from an individual mesochannel. Moreover, considering an non-square cross section for the mesochannel with depth greater than its width can

further improve the maintenance of uniform pressure across microchannel whilst increasing its ability to feed more microchannels.

4.5 Three-dimensional Elemental Exchanger: First Results

We now present the first results of the three-dimensional numerical model of the Elemental Exchanger with the assumptions developed in Chapter 3 and at the beginning of this chapter.

In a 3D geometry, the equations of transport (eq. 4.4) show that the geometrical sizes characterizing the exchanger are not fully taken into account by the conductance ratio J, and additional aspect ratios b/a and b/L also play a role. For coherence with the assumptions and results of the optimization on the exchanger in the 1D approximation, we restrict here our study to the case $a = 2b$ and $L/b = \lambda = 20$. Within these settings, the value of the non-dimensional power density is once again fully determined by the same non-dimensional numbers (Sh, J, Du_H and Cr) that were considered for the 1D approximation.

Furthermore, we focus our study on the actual maximum power density harvested by the exchanger in prescribed chemical conditions of operation, in order to compare it with the optimized 1D approximation, rather than on the various regimes of variation of the non-dimensional power density f. The prescribed chemical conditions are representative of sea/fresh water sodium chloride concentration $c_H = 660$ mM and $c_L = 1$ mM, and the reference surface charge consider in the Yale's team analysis $\sigma = -0.64$ C/sq.m[57]. The *COMSOL* implementation follows the similar steps as described beofre, adapted for the 3D case as follows:

Convection velocity: We do not take into account hydrodynamic entrance/outlet

effects in the microchannels and consider a well-established velocity profile uniform along the z-direction. For this purpose a 2D-velocity template $\vec{u}_{temp}$ is calculated separately, in an additional *COMSOL Component*, and "extruded" (using the *COMSOL* terminology) in the three-dimensional microchannel to be available at all values of z.

The 2D template is a non-dimensional velocity field obeying the Stokes equation of low-Reynolds number flow (as the Reynolds number does not play any role in the well-established flow profile in a duct of uniform section):

$$\frac{\partial^2 u_{temp,x}}{\partial x^2} + \frac{\partial^2 u_{temp,y}}{\partial y^2} = \frac{1}{ab} \tag{4.49}$$

with boundary conditions of zero-velocity on the three solid boundaries of the microchannel section and a symmetry property at $x = b$ (see figure (4.6)). It is then normalized by its average over the section so that $< u_{temp} >= 1$. The convection velocity in the transport equation (4.4) is thus $\frac{u(x,y)}{U} = u_{temp}(x,y)$.

Flux and Sources: Under the 3D geometry, the flux implemented in the *General Form PDE* eq. (A.1) is now a 6-dimension diffusion-convection flux, corresponding to the l.h.s of equation (4.4), that is

$$\vec{\Gamma} = \begin{bmatrix} -\vec{\nabla}\tilde{c}_h + (Pe/L)u_{temp}(x,y)\frac{\partial \tilde{c}_h}{\partial z} \\ -\vec{\nabla}\tilde{c}_l + (Pe/L)u_{temp}(x,y)\frac{\partial \tilde{c}_l}{\partial z} \end{bmatrix}$$

The bulk source is $s = \vec{0}$, and the r.h.s of the transport equation is implemented by an *Edge Source* feature, the calculation of the selectivity t entering in the expression of the line source being performed as explained in section 3.

Meshing: The mesh of the microchannel is based on a mesh of the section which is reproduced ("*Swept*") along of the z-direction with finer steps close to the chan-

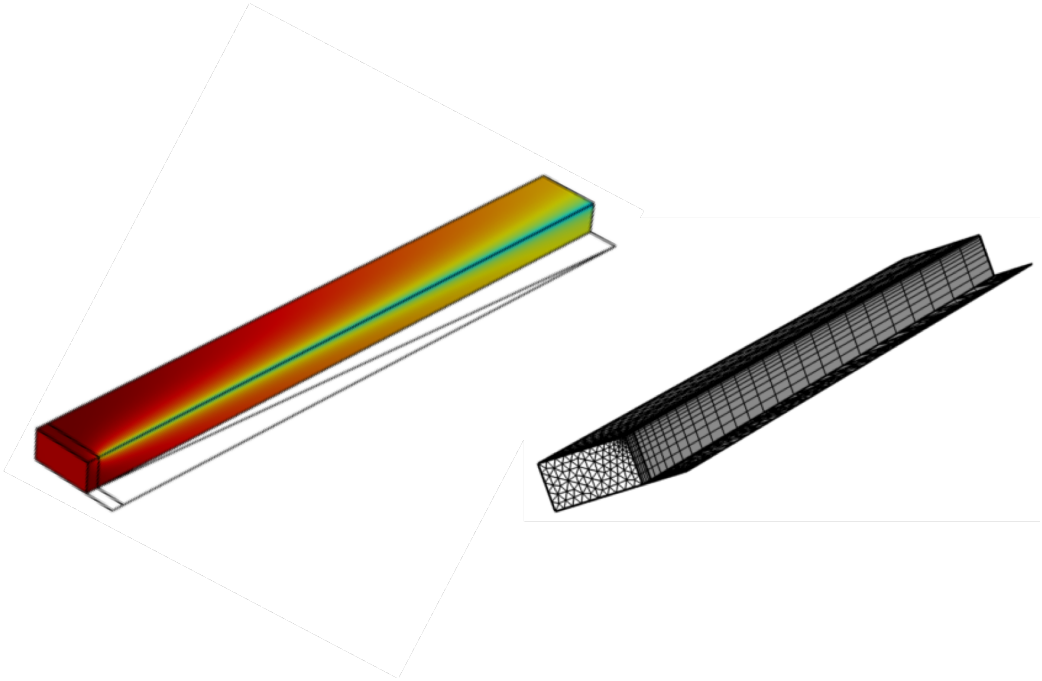

Figure 4.6: Left: two-dimensional velocity template in the microchannel section of section ab with $a = 2b$ (arbitrary units). Right: mesh of the 3D microchannel. The mesh of the section is the same as the one used to calculate the two-dimensional velocity template.

nel entrance. The section mesh is the same as the one used to calculate the 2D velocity template, and the mesh size is made finer close to the vertex corresponding to the junction with the nanochannel.

Power Density: Figure 4.7(left) shows the power density obtained from the 3D simulation of the elemental exchanger for two different widths of the microchannel ($b = 150, 250$nms). It is seen that the results obtained in the 3D simulation is lower than in the 1D simulation. One possible explanation for this reduction is power is attributed to the low velocities at the edge of the microchannel evident from the velocity profile in fig. 4.6. The source of the power generated by the exchanger corresponds to the nanochannel flux, represented by the velocity profile.

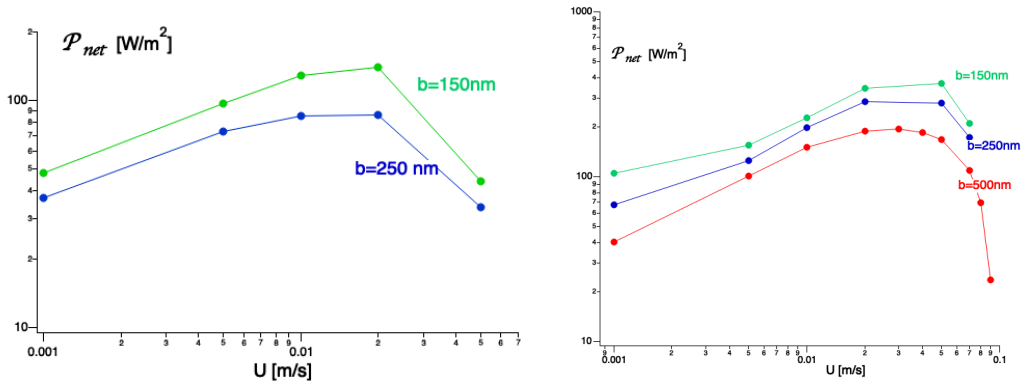

Figure 4.7: Left: Power density generated from the 3D simulation of the Elemental Exchanger plotted against microchannel convection velocity for microchannel width $b = 250, 150$nm. The velocity profile for the exchanger is shown in fig. 4.6. Right: Same plot for an exchanger with a velocity source in the middle of the microchannel, instead of the edge. It can be seen that is configuration of the exchanger produces approximated 2.5 times more power compared to the other configuration.

The deficit in the power density can however be overcome by imposing a velocity source at the middle of microchannel. The geometry of the elemental exchanger remains similar to the design proposed in the manuscript, but instead of closing the exchanger on top with a silicon cover, we flip one elemental exchanger on top of the other. This technique is similar to *flip-chip*[84] geometry, commonly used in microelectronic industry.

The flip-chip architecture results to the nanoslit being aligned in the middle of the microchannel cross-section, resulting to a larger shear on the microchannel walls and resulting to a higher density of power generated, as seen in the fig. 4.7(right).

It is also worth noting that the effect of osmotic volumetric flux through the nanochannel has not been considered for any of the simulations. This flux is expected to enchance the mixing in the microchannel, particularly in the case of 3D elemental exchanger with nanoslit at the corner of the microchannel, resulting to power densities comparable to its 1D counterpart.

4.6 Conclusion and Perspectives

This chapter illustrates the advantage of tailoring fluid flow at intermediate microchannel convection velocities as a promising route toward nanopore based energy harvesting from salinity gradients. The 1D model of the elemental exchanger described here demonstrates the possibility of harvesting net power density up to 1 kW/m^2 for an exchanger of length 20 μm. Not only is this result significantly higher than the current PRO and RED systems, but also hundred times larger than the theoretical predictions for the maximum output of membranes made of best available nanopores. The fabrication of a device of such minute length may present some difficulties, especially with bonding the exchanger to mesochannels, but is still achievable using the current development in Silicon fabrication industry.

We showed the first results of the 3D simulation of the elemental exchanger, which indicated a power lower than it's 1D counterpart (≈ 300 W/sq.m). This result underlines the importance of the velocity profile in the microchannel and the mixing of fluids within it. This low power-density of the 3D exchanger is still highly motivating as even the most pessimistic approach toward the realization of the exchanger, the neglecting of osmotic flux through the nanochannel, yields higher power than existing Blue energy technologies.

This chapter can a bed-rock in the development of silicon based nanofabricated architectures for Blue energy harvesting. The following are the perspectives of advancing beyond the elemental exchanger using the advancement in silicon lithography techniques:

- 3D piling of elemental exchanger is a straightforward possibility.
- Further research in incorporating osmotic effects may extend the extractable

power beyond the current limits.

- There is scope of developing ionic exchangers like RED in the nanoscale with alternating surface charge coatings on the nanoslit.

CHAPTER 5

Architecture of the Multi-Scale Exchanger

5.1 Introduction

The analyses in the previous chapters provides us a foundation to expand our study beyond theory and work towards the fabrication of an exchanger capable of efficiently extracting electrical energy from the salinity gradient between two distinct sources of water. This chapter is concerned with the design and the implementation of the 3D architecture of a parallelized nanofluidic exchanger. The design of this exchanger is intended to be a proof of concept for the viability of multi-scale exchangers. We focus on the determination of dimensions of such an exchanger and the constraints associated with its design. The results from the preceding chapter outline that maximum power can be extracted from the exchanger at an intermediate regime of convection velocity in the microtrenches, leading to reduced hydrodynamic losses. This chapter aims at demonstrating such a behavior with a simple composite approach which combines hard and soft lithography. It accounts for and describes the constraints in design imposed by the fabrication processes. As a first experimental prototype, silicon lithography is minimized and complemented by the use of PDMS which in return imposes size constraints.

The dense nature of the exchanger design necessitates the study of short-circuits which might occur within the exchanger, dictating the positioning of electrodes and playing a vital role in the final design. The accounting of all the constraints results to a three-component chip made by sandwiching a thin Silicon wafer in between two PDMS microchips, hereby referred to as *The Sandwich Exchanger*.

The Silicon chip within the Sandwich consists of parallel microtrenches separated by the nanotrenches which run between them. The micro/nanotrenches are hollowed out using lithography on a Silicon substrate. These trenches constitute the *active region* on the face of the Silicon wafer. The axis normal to the wafer, *z-axis* in this study, is used to feed liquids into the active region using the two PDMS microchips.

We defined the elemental exchanger previously in chapter - 2 as a set of two microchannels with a rectangular cross-section, separated by a nanoslit that runs between them. The microchannel/nanoslits are carved out from their substrate using lithography, therefore for clarity, the channels will be referred to as "*microtrenches*" and "*nanotrenches*" for the remainder of this chapter. We optimized the dimensions of the elemental exchanger to be able to extract maximum electrical energy from it (Chapter - 4, section - 4.4), however the final design of the parallelized exchanger has to account for the connections to the macroscopic world. The realization of such an exchanger requires the construction of a three-dimensional system, where ion exchange occurs on a two-dimensional plane, while the third dimension is used to supply, collect, and recirculate the respective liquids.

5.2 PDMS-Silicon Sandwich Exchanger

The Sandwich Exchanger consists of three microchips, meshed together to allow smooth exchange of fluids between them. The bottom and the top segments of the exchanger are made from Polydimethylsiloxane (PDMS) polymer and the middle segment, which houses the microtrenches and the nanotrenches, is fabricated on a Silicon wafer. The region where the exchange of ions takes place is termed as the *active region* and is situated on the top face of the Silicon wafer. The active region

consists of multiple elemental exchangers forming a grid, optimized to increase the electrical energy generated and simultaneously reducing the hydraulic power required to run fluids inside the exchanger.

The bottom-PDMS (bPDMS) chip houses two reservoirs that hold solutions of different ion concentrations. The reservoir feeds the solutions into mesotrenches etched on the top surface of the bPDMS chip, and these mesotrenches consequently feed the active region through drill-holes (or meso-pores) present on the bottom of the Silicon wafer. After the fluids traverse through the active region, they are fall back into the bottom PDMS chip, into the waste-mesotrenches. The waste water is then transported away from the active region and moved to the top-PDMS (tPDMS) chip, through exit-holes drilled across the thickness of the Silicon wafer. The Silicon wafer is fabricated using *Silicon-on-Insulator (SoI)* technology as it provides a high resolution for lithography, but restricts the machining of the top-side of the wafer. As the drill-holes for inlets and outlets can only be machined from the top, it forces us to drain the active region into the bPDMS chip, segregating the high/low concentration fluids to opposite ends of active region, then pushing it up to the waste reservoir on tPDMS. The spatial segregation of fluids is important to position the electrodes on either side of the active region. The electrodes can then be applied with two different potentials, with low concentration liquids at high potential and vice versa. The schematic of the sandwich exchanger is illustrated in figure 5.1.

We first list the constraints in the fabrication processes, which will set a premise for the design and the dimensions chosen for the Sandwich exchanger, before detailing the components of the Sandwich exchanger.

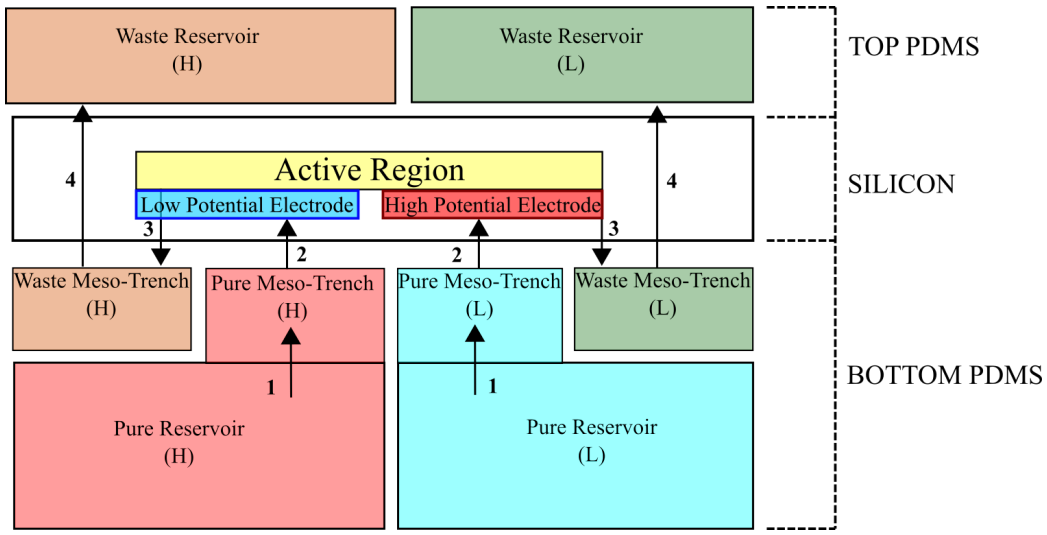

Figure 5.1: Schematic of fluid flow inside the Sandwich Exchanger. “H” and “L” correspond to fluids with high and low ion concentrations respectively. The numbers indicate the sequence of fluid flow inside the exchanger. The active region is an array of microchannels separated where exchange of ions takes place. Electrodes are deposited on the bottom face of the Silicon wafer such that the liquids are in contact with the electrodes as they enter the active region.

5.3 Constraints in Device Design

This section lists and expands on the limitations leading to the design of the exchanger illustrated in the previous sections. Constraints that dictate the dimensions and the architecture of the nanofluidic exchanger are categorized into the following three categories, which will be elaborated later in this section:

- Fabrication constraints - These are the constraints that arise due to the several fabrication processes involved in the design of the exchanger. These constraints include the SoI fabrication of the silicon wafer, free length required for plasma bonding the silicon to the PDMS chip, the etching process of the top cover of the Silicon wafer, the stability of the nanoslit cantilever against bending stress and the limitations with the functionalization of the

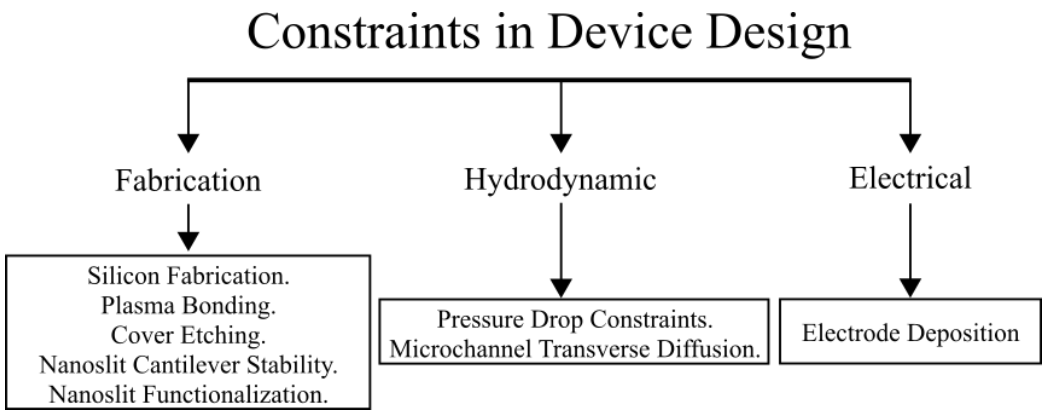

Figure 5.2: Categorization of Constraints in Exchanger Design.

nanoslit.

- Hydrodynamic constraints - These constraints include the consideration of pressure drop inside the various mesotrenches and the microtrenches in the exchanger and the transverse diffusion inside the microtrenches perpendicular to the convection velocity of fluids.
- Electrical constraints - The constraints that affect the electrical characteristics of the exchanger are categorized here. These include the placement of electrodes and the electrical short circuits arising due to the dense design of the active region.

5.3.1 Fabrication Constraints

PDMS Constraints

As described in the beginning of the chapter, this prototype of the exchanger minimizes the use of Silicon lithography in the fabrication process. The use of PDMS, in turn, limits the width of the mesochannels to a maximum of 25μm, due to the in-house fabrication capabilities available in $LiPhy$, Grenoble. This width of the mesochannel leads to the determination of the microchannel length to be

equal to 100μm. This microchannel length frees a length of 25μm in between the mesochannels, which will be available for surface bonding with the silicon wafer. We know from the previous chapter that the length of the microchannel is sixes the microchannel width 'b', from the analyses in section - 4.4.2. Hence the width b of the microchannel is fixed at 2μm for $L = 100\mu$m.

Silicon Wafer Fabrication

As the Silicon wafer will be fabricated at CEA-Leti, Grenoble using Silicon-on-Insulator wafer elaborated in section 5.5.1 of this chapter. The buried oxide and the substrate underneath is removed during the final step of the fabrication and hence all the lithography associated with the wafer is limited to its top face, before bonding it to the thick wafer cover. The thickness of the silicon wafer is in the range of 10μm to 50μm^3, therefore considering the mechanical strength of the wafer, the depth of the microchannels is restricted to a maximum of 2μm.

Plasma Bonding

The PDMS chips and the Silicon wafer are subjected to an air plasma under a chamber pressure of 900mTorr for 40s to create a sealed microfluidic system which can withstand a pressure up to 5 bars before leaking[85]. The plasma bonding is done step-wise; first the bottom face of silicon wafer is exposed to the plasma along with the bottom-PDMS (bPDMS) chip (top face oriented to plasma). These chips are then aligned together under a optical microscope and bonded together. The bonded chips are then kept in a 65°C over for 2 hours to allow the danging bonds to stabilise and adhere to the bonded surfaces. This procedure is repeated again for the top-PDMS (tPDMS) chip, which is exposed to the plasma on bottom-face, along with the bPDMS-Silicon assembly, leading to a fully bonded *Sandwich exchanger*.

Surface roughness plays a vital role in ensuring the bond strength of two plasma bonded surfaces. The presence of inlet and outlet holes in the bottom of the Silicon wafer affects the surface available for plasma bonding with the bPDMS chip. This creates a constraint affecting the minimum length of the active region. Therefore to ensure no leakage of fluids between the bPDMS and the Silicon wafer, the active region is fixed at a length of 10mm, with each inlet and outlet holes spaced out by a distance of 10μm between them. Explain 10mm in context of pdms constraint.

Cover Etching

The etching protocol for the Silicon cover has been elaborated in section 5.4.2 of this chapter. The protocol for etching results to two pyramidal trenches with width of 1.3mm and length of 10mm on the top face of the cover as illustrated in fig.5.5b. As the tPDMS chip is to be meshed with this etched trench in the cover, it limits the size of the waster reservoirs to a maximum width of 1.3mm with a distance of 1mm between them. This results to a section as illustrated in fig.5.7a.

Nanoslit Cantilever Stability

The stability of the nanoslit depends on the modulus of elasticity of the silicon cantilever beam that runs in between the two microtrenches. When fluids of different concentrations flow in the microtrenches, it results to a diffusive flux across the nanoslit. This diffusive flux exerts a force on the nanoslit support beam, which may lead to bending of the nanoslit cantilever. This bending can change the cross section of the nanoslit from straight to a conical cross section. Studies done on conical nanopores have shown that the electrical and the transport properties are significantly different from that of a straight nanopore[86,87,88]. Hence, the stability of the nanoslit cantilever is vital to avoid undesirable rectification effects inside the active region.

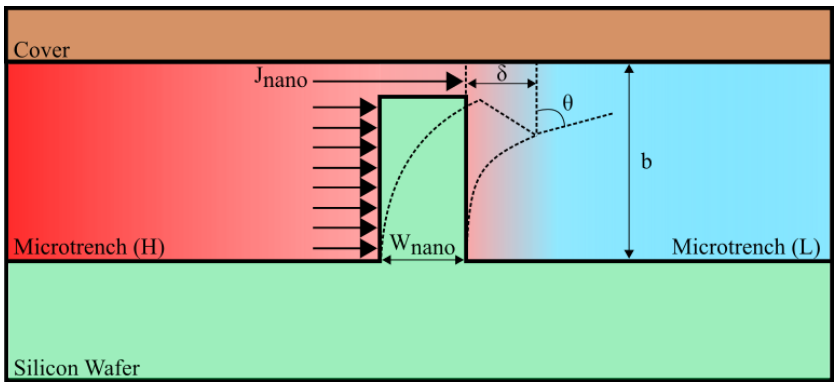

Figure 5.3: Bending of the nanoslit cantilever changes the entry and exit area of the fluids, leading to variable electrical characteristics. The depth of the microtrench is b, δ and θ are the deflection and the bending angle of the cantilever respectively. J_{nano} is the flux through the nanoslit per unit nanoslit length and W_{nano} is the width of the nanochanel.

Figure 5.3 above illustrates the forces acting on the nanoslit cantilever. The nanoslit flux coming from the microtrench carrying fluid with high concentration pushes against the nanoslit beam at all points below the nanoslit entry. As the origin of the flux is majorly due to the pressure applied to maintain fluid flow in the microtrench, this setup can be considered as a cantilever beam under a uniformly distributed load. Therefore the deflection δ and the angle of bending θ for a cantilever beam is found to be a function of its elastic modulus (E) and area moment of inertia (I)[89]:

$$\delta = \frac{-qh_{canti}^4}{8EI} = \frac{-3\Delta p\, h_{canti}^4}{2EW_{nano}^3} \qquad \theta = \frac{qh_{canti}^3}{6EI} = \frac{2\Delta p\, h_{canti}^3}{EW_{nano}^3} \tag{5.1}$$

where h_{canti} is the cantilever height, $q = L\Delta P$ is the force per unit length exerted by the fluid on the nanoslit, $I = LW_{nano}^3/12$ is the area moment of inertia and W_{nano} is the width of the nanoslit. This angle of bending changes the nanoslit

height. This change in height is calculated as:

$$\Delta H_{nano} = \theta W_{nano} = \frac{2\Delta p\, h_{canti}^3}{E W_{nano}^2} \tag{5.2}$$

Nanoslit Functionalization

The exchanger described in this manuscript relies heavily on the selective permeability of the nanoslit. The electric potential develops in the exchanger due to the migration of cations from the region of high concentration to the low concentration. Therefore, it is of paramount importance to discuss the viability of functionalizing such channel, whilst retaining a constant height throughout the nanoslit cross-section. A viable solution to functionalizing the nanoslit is hence coating it with an ultra-thin layer of negatively charged species like Boron Nitride. The deposition can be performed at a temperature range of 600°C to 800°C, leading to a thin film of 10Å to 20Å[90]. Alternatively, ionic liquids under an external electric field can be used to adsorb negatively charged ions on the surface of the nanoslit cantilever, creating a negatively charged cation selective nanoslit.

5.3.2 Hydrodynamic Constraints

Pressure Drop Considerations

The fluids in the microtrenches need to flow through them continuously, for the ions in the active region to be replenished as they generate electricity. The conditions leading to the determination of the Sherwood number is elaborated in chapter - 4 (section - 4.4). To maintain structural integrity of the exchanger the pressure drop in the microtrenches and the mesotrenches cannot exceed a maximum of 1 bar. This pressure drop dictates the size of the cross-section of the microtrenches and mesotrenches. The size optimizations leading to the maximum net power in

the exchanger were elaborated in Chapter - 4, sections - 4.4.2,4.4, therefore the constraints mentioned get carried over to designing the Sandwich exchanger as well.

Transverse Diffusion in the Microtrench

The calculations of electrical power and current inside the exchanger are performed under the assumption that the ion concentration remain constant in the direction perpendicular to the flow of liquids inside the microtrenches. This assumption only holds true when ions arriving/leaving the microtrenches diffuse instantaneously across its cross section, before travelling along its length. Low transverse diffusion in the microchannel leads to the problem of concentration polarization in the exchanger, as described by *Wang et. al*[57]. Concentration polarization significantly deteriorates the efficiency of the exchanger as it leads to the development of a boundary layer inside the microtrenches, greatly reducing the ability of ions to diffuse across the nanoslit. This problem can be prevented by choosing appropriate dimension of the microtrench cross-section that minimizes the time take for the ion to diffuse through it after arriving from high concentration region.

5.3.3 Electrical Constraints

The electrodes, as mentioned in the previous sections of this chapter, are to be deposited on the bottom face of the Silicon wafer, on either side of the active region. As the fluids of high concentration and low concentration have to be applied with different potentials, it is of paramount importance to have a strict spatial segregation of these fluids on either side of the active region. As the bottom face of Silicon is in direct contact with the fluids in the mesotrenches, it allows the respective electrode potential to be applied to them before they enter the active

region. It should also be noted that the placement of electrodes must not be too far away from the active region, to reduce the possibility of screening of the electrical potential particularly in the low concentration fluid. Therefore, the electrodes are to be deposited in the area between the mesopore array and the active region, spanning through the length of the Silicon wafer.

5.4 Components of the Sandwich Exchanger

5.4.1 Silicon Chip

The Silicon chip is the core component of the device. It houses the active region, where the exchange of ions occurs. The chip is fabricated using *Silicon-on-Insulator* (SOI) technology which enables it to be up to 10μm in thickness. The Silicon chip is approximately 2.5mm in breadth and 12mm in length, however these distances only approximate the clearance distance required during the cleaving step of chip fabrication. The active region contains 75 selectively permeable nanotrenches, which are 1nm in depth and run across a length of 10mm. As each elemental exchanger is defined by a single nanoslit, this prototype comprises of 75 elemental exchangers stacked parallel to each other. The exchangers are also arranged end-to-end over 10mm and as the maximum length of the elemental exchanger is a maximum of 100μm, it results to a combination of 100 exchangers in the end-to-end arrangement. The resulting active region is hence a two dimensional array of 75$\times$100 elemental exchangers arranged over the Silicon surface. The schematic of the Silicon chip along with the active region is shown in figure 5.4.

The cross-section of the microtrench is 2μm wide, 2μm deep and the nanotrench has a section of 200nm$\times$1nm, both spanning over a length of 100μm. The dimen-

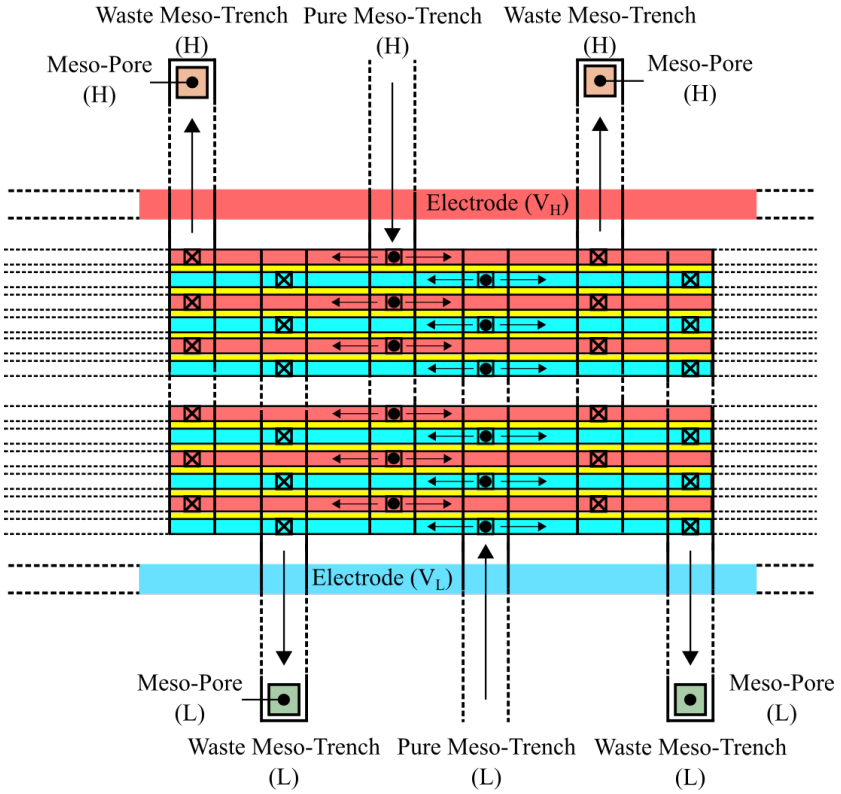

Figure 5.4: Schematic of the active region. The red, blue colors represent the high and low concentration microtrenches (2μm$\times100\mu$m$\times2\mu$m) respectively. The nanoslit (200nm$\times100\mu$m$\times$1nm), selective to cations, is illustrated in yellow. The inlets (dots) and outlets (crosses) have a cross section of 2μm$\times2\mu$m and are separated by a distance of 100 μm corresponding to the length of the elemental exchanger. The sandwich exchanger is a combination of co-flow and counter-flow. The fluids inside the active regions are circulated through the meso-trenches on the bottom-PDMS chip. The waste fluid is transported from the bottom PDMS chip to the top through the mesopores (20μm$\times20\mu$m) that are drilled 1mm away from the active region on either side.

sions of the trenches are a consequence of the various constraints that are elaborated in the section 5.3 of this chapter. The inlets and outlets are drilled through the Silicon wafer and mesh with the meso-trenches present in the bottom-PDMS chip. The drill holes in the microtrenches have a square cross-section side 2μm.

Ag/AgCl electrodes are deposited on the bottom face of the Silicon wafer on either

side of the active region. This arrangement enables the application of different potentials on the high and low concentration fluids, essential to energy generation process. The waste mesotrenches carry the fluids away from the active region towards meso-pores drilled through the wafer, situated 1mm away from each side of the active region. Spatial segregation of the high and low concentration fluids aides the re-circulation of fluids, if required. The mesopores have a square cross section of 20μm, carry the waste liquids from the bottom-PDMS to the waste reservoir on the top-PDMS through an etched silicon cover above the wafer.

The nanoslit is functionalized to preferentially allow cations to pass through it. This functionalization is achieved by the deposition of a negatively charged species on the surface of the nanoslit, resulting to a electrostatic repulsion of anions, whilst allowing a free passage to the cation. The process of nanoslit functionalization is detailed in section 5.3.1 of this chapter.

5.4.2 Silicon Cover

A cover made of Silicon in (100) orientation sits on top of the Silicon wafer. This cover is 700μm thick, including thickness includes two layers of silica thermally grown on the top and bottom face of the cover. This technique of silica growth on Silicon wafer is demonstrated by *Sharma et. al.*[91]. It is achieved by exposing the Silicon wafer to steam at a temperature of 950°C followed by annealing at 1100°C resulted in 1.5μm thick silica layer on the exposed surface of the wafer. The silicon-cover will be aligned with the active region and the top surface of the cover will bare markings indicating the positions of meso-pores and the active region. The cover is then etched layer-by-layer precisely at the position of the mesopores, using Hydrogen Fluoride (HF) to remove the top layer of Silica, followed by the etching of the bulk Silicon in the cover using Tetramethylammonium Hydroxide (TMAH). The presence of silica layer at the bottom of the cover

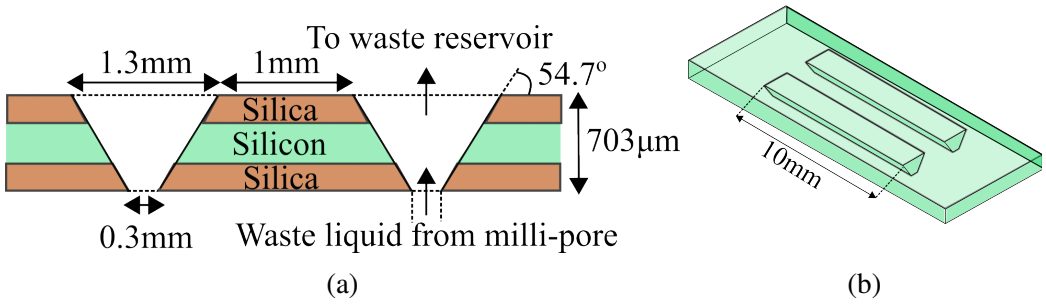

Figure 5.5: (a) Sectional and (b) Isometric schematic of the Silicon cover after etching.

ensures the protection of the active region from the effects of TMAH. The final step of the silicon-cover fabrication is the etching of the bottom silica layer using HF.

The type of etching employed here is called anisotropic wet etching. In an anisotropic etching process, a sample is etched preferentially in one crystallographic plane compared to the others. The bonding energy of Silicon atoms in (100) plane is lower than the atoms in (111) plane, therefore the atoms in the (100) plane etch at a higher rate. This results to a pyramidal structure as shown in fig.5.5, with sidewalls at an angle of 54.7°from the (100) plane. It is recommended to use 25% TMAH at 80°C to etch the bulk Silicon in the cover as it is 6000 times more selective towards Silicon, compared to silica[92]. HF is used in the cleaning of silica layer as its properties are well studied to be aggressive while being selective in removing native oxide layers from wafer substrates[93,94,95].

5.4.3 Bottom-PDMS chip

The main function of the bottom-PDMS (bPDMS) chip is to provide fresh fluid to the active region and circulate the waste liquid to its respective reservoir on the top-PDMS chip. The architecture of this microchip is designed to provide a spatial segregation between high and low concentration fluids whilst increasing the

working length scale gradually to macroscopic lengths. It consists of two reservoirs (15mm$\times$3mm$\times$3mm) placed 4mm away from the edge of the active region on both sides. The reservoirs contain liquids of different concentrations, which will be pumped into the active region using mesotrenches. The mesotrenches extend from the top of the reservoirs towards the active region and have a cross-section 25μm wide and 25μm deep. The mesotrenches are separated by a distance of 200μm from their respective centres and run down to the end of active region covering a distance of 5mm while meshing with respective inlet holes in the microtrenches. This leads to an inter-digitized arrangement of the mesotrenches and hence establishing the circulation of pure fluids into the active region.

The waste liquids from the exchanger drain into the bPDMS chip and transported to the mesopore array. This flow of waste liquid is achieved by the mesotrenches which are 2mm long, spanning from the mesopores till the end of the active region. These waste-mesotrenches have the same cross-section as their pure counterpart and mesh with the outlet drill holes in the microtrenches. As the microtrenches drain themselves into the waste-mesotrench, the fluid is carried toward their respective mesopore and pushed up to the tPDMS reservoir, passing through the etched Silicon cover.

The dimensions of the mesotrenches are chosen considering that the ratio of the pressure drop in the mesotrenches is less than 1% of that in the microtrenches. The calculation of the pressure drops and their effect on the dimensions of the mesotrenches are elaborated in the section 5.3 of this chapter. The bPDMS chip is sealed to the Silicon chip using Plasma bonding technique[96]. We intend to use air-plasma at a chamber pressure of 900 mTorr with an exposure time of 40s during this bonding procedure. This technique creates a bond strength of 5 bars between the surfaces of PDMS and Silicon[85].

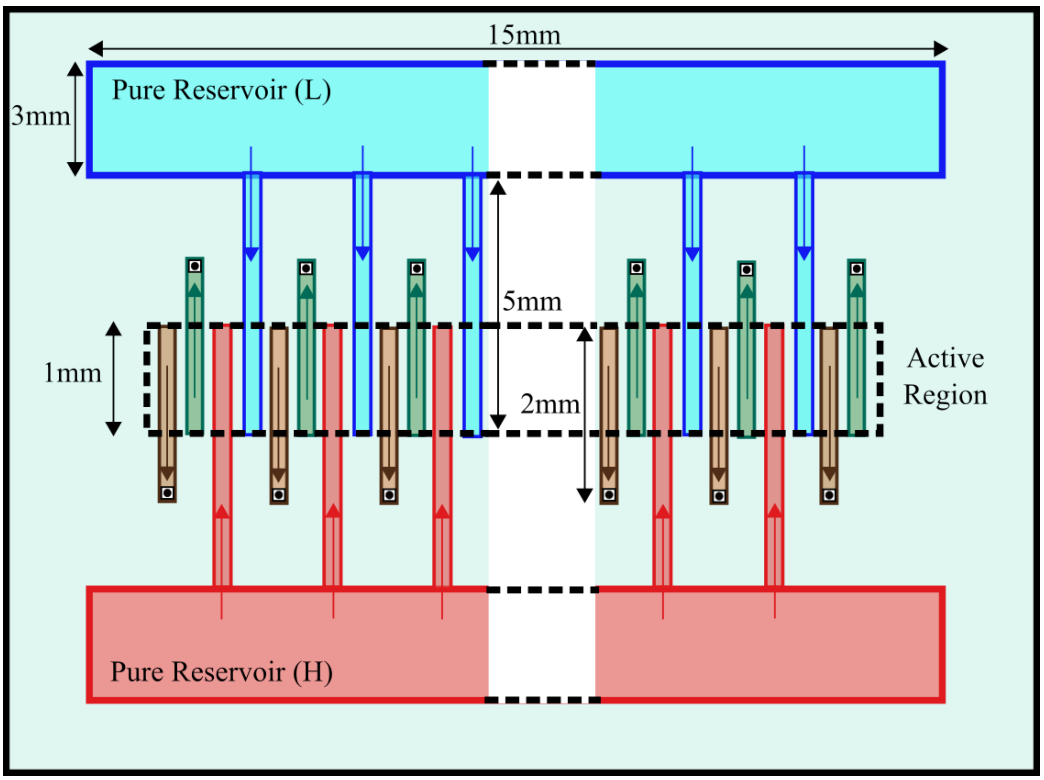

Figure 5.6: Top view schematic of bPDMS chip. The pure mesotrenches are shown in red, blue for high and low concentration fluids respectively. The waste mesotrenches are depicted in brown for high concentration fluid and green for low concentration fluid. The waste mesotrenches extend till the mesopores, shown here as white square with a dot, extending upwards towards the Silicon wafer. The dotted rectangle in the middle shows the position of active region in the Silicon wafer and the colored arrows indicate the fluid flow in each trench. The reservoir is 15mm wide, with a cross-section of 3mm$\times$3mm. The mesochannels are 50μm deep and 25μm in width. The length of pure mesotrenches is 5mm, whereas the waste mesotrenches are 2mm long.

5.4.4 Top PDMS chip

The top-PDMS (tPDMS) chip has a relatively simple architecture. This chip has reservoirs for waste liquids exclusively, which enter from the Silicon cover on either side of the active region. The reservoirs are situated just above the etched hole in the Silicon cover and have a square cross section of width and depth equal

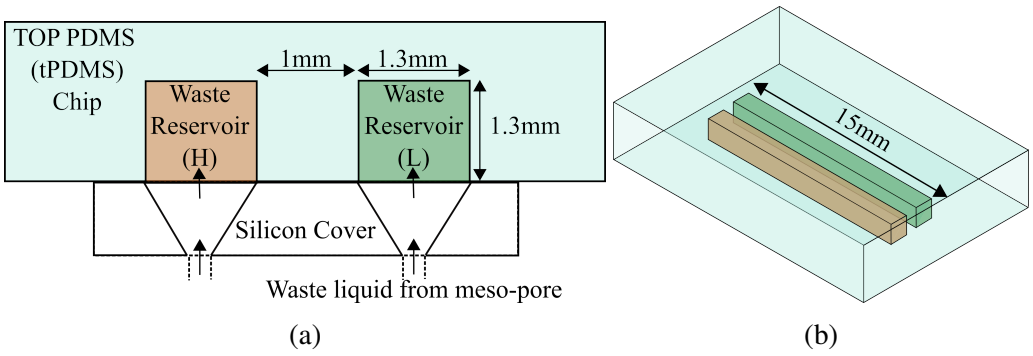

Figure 5.7: (a) Sectional and (b) Isometric schematic of the top-PDMS microchip.

to 1.3mm. The reservoirs are 15mm long and are separated from each other by a distance of 1mm. These reservoirs are also bonded to Silicon and the bPDMS by plasma bonding technique, described in the previous sub-section.

5.5 Fabrication of the Sandwich Exchanger

5.5.1 Overview of Silicon-on-Insulator (SoI) fabrication

Silicon-on-Insulator (SOI) method has been extensively used in the fabrication of transistors, tunnelling devices since the late 1990s. This type of fabrication involves the use of a single crystalline layer of Silicon, separated from its bulk substrate by a layer of Silicon Oxide (SiO_2)[97]. This SiO_2 layer, termed as *buried oxide* layer, is grown inside a Silicon substrate and removed after the features on the crystalline Silicon have been successfully printed on the face of the wafer. The oxide layer is grown inside the a Silicon substrate by mainly using two processes, *separation by implanted oxygen (SIMOX)* and *Smart Cut*^{TM} technology[3]. SIMOX method employs the synthesizing the oxide layer by directly implanting oxygen atoms into the Silicon substrate at a temperature of 600°C, followed by annealing it at a high temperature (>1300°C)[98]. The annealing temperature following the implantation is an important parameter to be controlled as it directly influences

the sharpness of the interfaces between the crystalline Silicon and the buried oxide layers. Currently, the SIMOX wafers are annealed at a temperature of 1350°C for most SOI applications as it provides atomically planar interfaces in the wafer block[99]. Alternatively, smart cut™ technology uses hydrogen implantation as an "atomic scalpel" to remove a thin layer of Silicon from the wafer[100]. This method uses two Silicon wafers, called "seed wafer" and "handle" wafer, both with a layer of thermally grown oxide on their top face. The seed wafer is then implanted with hydrogen through the oxide layer into the Silicon, creating a hydrogen-rich zone in the substrate. The implantation of hydrogen creates micro-cavities inside the Silicon substrate, which will be useful during the final step of cleaving the wafer. The handle wafer is then flipped on top of the seed wafer such that the two oxide layers are in contact with one another. This step is followed by wafer bonding between the seed and the handle wafer. Once the wafers are bonded, the wafer pairs are heated to a temperature of 600°C, leading to the expansion of implanted hydrogen and the cleaving along the hydrogen implanted plane. A schematic of the smart-cut process is illustrated in fig.5.8. This buried SoI wafer is then subjected to lithography to print the required pattern on the crystalline face of the wafer, followed by the removal of the substrate and the oxide layer through mechanical grinding and polishing.

This process of fabrication allows the scaling of wafer thickness below 100μm which optimum for applications involving nanofluidics as it helps reducing the hydrodynamic losses to a great extent. The parallelized sandwich-exchanger employs the use of a Silicon chip that is 10μm in thickness hence, given the state of the art in the Silicon lithography, is achievable using SoI fabrication of Silicon wafers.

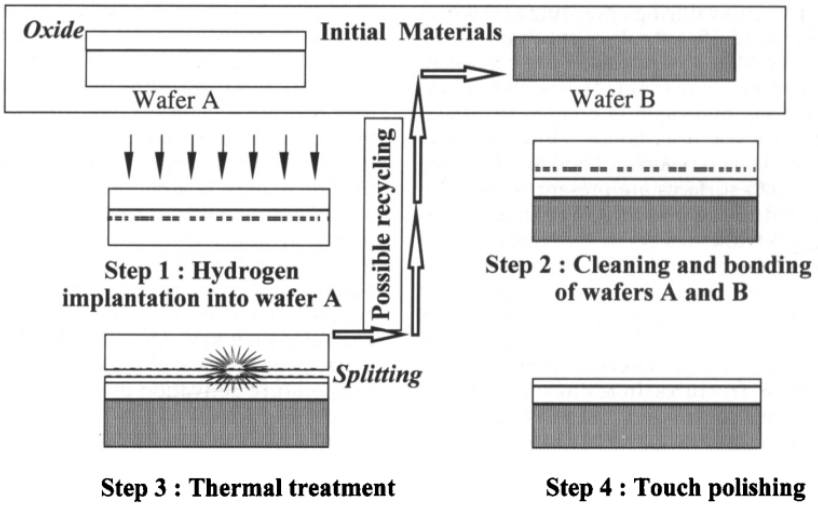

Figure 5.8: Schematic of Smart Cut^{TM} SoI fabrication[100]. Wafer "A" is the seed wafer and Wafer "B" is the handle wafer.

5.5.2 Fabrication Protocol for Silicon Wafer

The fabrication of Silicon wafer starts with a Silicon-on-insulator wafer with a buried oxide layer 1μm thick, with a crystalline top of 10μm thickness. The first step involves the definition of the microtrenches on the top face of the wafer. As previously mentioned, the microtrenches are 1μm deep and 2μm wide with a distance of 100 nm between two parallel trenches. During the first positioning of the microtrenches however, the distance between two parallel microtrenches is doubled to 200 nm. This double spacing is to compensate for the oxidation layer that will be deposited on the top of the wafer, which follows immediately after the definition of the microtrenches. The oxidation of the wafer is performed by thermally growing a layer of Silicon Oxide on top of the microtrenches using short-time oxidation, resulting to a 100 nm gap between the two microtrenches (Step- 3 in fig. 5.9). This step is followed with defining the height of the nanotrench in between the microtrenches. The definition of the nanotrenches requires a different mask than the one used for microtrenches, to ensure alignment specifications. Once the

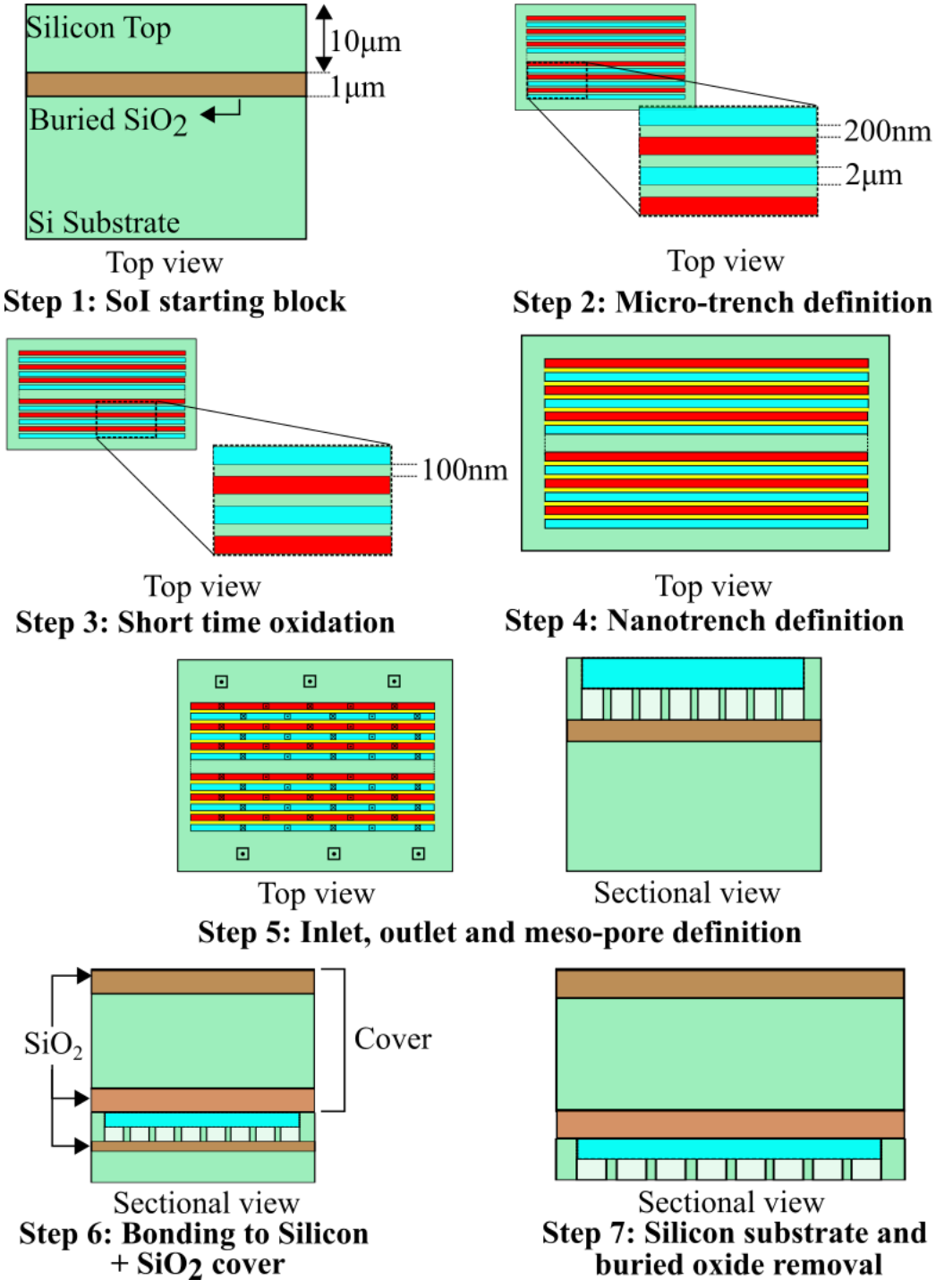

Figure 5.9: Fabrication protocol for Silicon wafer. The microtrenches with high, low concentration fluids are represented in red and blue respectively. The nanotrench is in yellow and the Silicon oxide is represented by the brown color.

trenches are etched on the wafer, the next step involves the drilling of inlet and outlet holes in the microtrenches and also then meso-pores for the waste liquid to exit the wafer. These holes are drilled from the top-face of the wafer, until it reaches the buried oxide layer underneath the surface. The inlet/exits in the microtrenches are circular with a diameter of 1μm. The penultimate step of the fabrication process is the direct bonding of a Silicon cover on top of the machined wafer. This cover has a thin layer of Silicon Oxide grown on its top and bottom face, which acts as a limiter for harsh etchants like TMAH, used in the definition of waste exits on the cover (fig. 5.4.2), from damaging the active region. The last step in the fabrication of the chip involves the removal of the buried oxide layer in the bottom of the chip, along with the excess substrate underneath the Silica layer.

5.6 Conclusions and Perspectives

This chapter proposes a three-layer microchip design to harvest electricity using the salinity gradient between two sources of water. The exchanger is called *The Sandwich Exchanger* and it consists of two microchips made out of PDMS polymer which house a Silicon wafer in between them. The Silicon wafer includes the *active region* consisting of parallel microtrenches separated form each other by a thin nanotrench spanning the entire length of the active region. The exchange of ions takes place inside the active region, on the place of the Silicon wafer and the third dimension (z-axis in this study) is used to feed fluid circulation to the exchanger.

The proposed device design is compatible with the current state of art in the Silicon lithography technology and utilizes *Silicon-on-Insulator* (SOI) fabrication technique to produce the required microtrenches and nanotrenches.

The dimensions of the active region and the mechanism of feeding liquids into the

exchanger impact the efficiency of the exchanger directly and therefore are subject to numerous constraints, elaborated in this chapter. This exchanger, once fabricated, should be able to bypass the problem of concentration polarization, which has been plaguing the development of nanopore-based Blue Energy technologies.

The proposed architecture of the device however still has to cope with the requirement of impurities - free solutions to be injected into the exchanger, which is not straightforward when extracting electricity from the mixing of sea water with rivers. The presence of impurities like dust or sand in the exchanger will ruin the functioning of the exchanger due to the extremely small dimensions of the active region. Therefore, the potential application of this exchanger in the near future is limited to industrial applications of small scale production of renewable energy.

CHAPTER 6

Conclusions and Summary of the Manuscript

The primary contribution of this manuscript is toward the modelling and the realization of a new type of device focused on the extraction of Blue energy. We started with an introduction to the field of nanofluidics, the length scale associated to it and the significance of novel phenomenon observed in fluids confined to nanometric lengths. We then detailed the recent advances in the field of Blue energy harvesting along with their perspectives and the bottlenecks. We identified the internal concentration polarization as the major issue that limits the development of membrane based processes aimed at harvesting energy from salinity gradient and set the premise for the development of an "exchanger" designed around multi-scale flow architecture which can successfully bypass the concentration polarization issue.

We then introduced the concept of an "Elemental Nanofluidic Exchanger", which consists of two microchannels carved parallel to one another, on a silicon substrate separated by a nanoslit running in between them, along their length. Here we developed a toy-model to identify two parameters, Sherwood number (Sh) and inlet contrast ratio (Cr), that can accurately characterize the state of the system at any point during its operation.

After ascertaining the parameters describing the state of the system we focused on the development of the non-linear dynamics of ions observed inside the nanoslit under 1D approximation and the estimated the limit of the electrical power that the elemental exchanger can produce per unit surface area it occupies. This limit power was calculated to be equal to 745 W/sq.m, which is significantly higher

than all of the existing technologies aimed at Blue energy harvesting. Here we also identified the surface charge of the nanoslit as the root cause of the non-linear dynamics observed at this length scale and quantified its effect on the ion selectivity of the nanoslit. It was found that the ion selectivity is coupled to the potential difference across the nanoslit implicitly, leading to non-linear current voltage (IV) characteristics.

The quantification of the nanoscale dynamics in the nanoslit gave us the basis to develop a robust model for the elemental exchanger which integrates the micro-scale dynamics observed in the microchannel and the non-linear transport observed inside the nanoslit. In chapter - 4 we detailed the full theoretical model of the multi-scale dynamics inside the Elemental Exchanger and highlighted the importance of tailoring fluid flow around the nanoslit to maximize the net power output of the exchanger. We calculated the dimensional aspects of the exchanger required to reduce the hydraulic dissipation and optimized the working regime of the exchanger to further increase its efficiency. We also focused on the dimensions of "mesochannels" that feed the exchanger and provided the first results of the 3D simulation of the elemental exchanger, where we found a power density equal to 300 W/sq.m, after optimization of the dimensions. We then suggested the means to further improve this density of power, by accounting for the osmotic volumetric flux through the nanoslit, which will improve the mixing of ions inside the microchannel.

In Chapter - 5 we detailed the fabrication of a prototype multi-scale exchanger, called "*The Sandwich*", which was aimed to be a proof of concept device for harvesting Blue energy using the theoretical models developed in the previous chapters of the manuscript. We described the fabrication protocol for the Elemental exchanger using the current development in Silicon-on-Insulator technology and also listed the constraints associated with the fabrication procedures. This

prototype device involved the use of PDMS microchips bonded to the elemental exchanger, these PDMS chips house the mesochannels and reservoirs required to feed the microchannels.

Bibliography

[1] Jan CT Eijkel and Albert van den Berg. "Nanofluidics: what is it and what can we expect from it?" In: *Microfluidics and Nanofluidics* 1.3 (2005), pp. 249–267.

[2] Reto B Schoch, Jongyoon Han, and Philippe Renaud. "Transport phenomena in nanofluidics". In: *Reviews of modern physics* 80.3 (2008), p. 839.

[3] George K Celler and Sorin Cristoloveanu. "Frontiers of silicon-on-insulator". In: *Journal of Applied Physics* 93.9 (2003), pp. 4955–4978.

[4] Li-Jun Wan. "Fabricating and controlling molecular self-organization at solid surfaces: Studies by scanning tunneling microscopy". In: *Accounts of chemical research* 39.5 (2006), pp. 334–342.

[5] Petra S Dittrich and Andreas Manz. "Lab-on-a-chip: microfluidics in drug discovery". In: *Nature reviews Drug discovery* 5.3 (2006), pp. 210–218.

[6] P Abgrall and AM Gue. "Lab-on-chip technologies: making a microfluidic network and coupling it into a complete microsystem-a review". In: *Journal of micromechanics and microengineering* 17.5 (2007), R15.

[7] Lydéric Bocquet and Elisabeth Charlaix. "Nanofluidics, from bulk to interfaces". In: *Chemical Society Reviews* 39.3 (2010), pp. 1073–1095.

[8] Massimiliano Di Ventra, Stephane Evoy, and James R Heflin Jr. *Introduction to nanoscale science and technology*. Springer, 2004.

[9] Hirofumi Daiguji. "Ion transport in nanofluidic channels". In: *Chemical Society Reviews* 39.3 (2010), pp. 901–911.

[10] Ngai Yin Yip et al. "Salinity gradients for sustainable energy: primer, progress, and prospects". In: *Environmental science & technology* 50.22 (2016), pp. 12072–12094.

[11] RA Robinson and RH Stokes. “The measurement and interpretation of conductance, chemical potential and diffusion in solutions of simple electrolytes”. In: *Electrolyte Solutions* (1959), p. 501.

[12] RE Pattle. “Production of electric power by mixing fresh and salt water in the hydroelectric pile”. In: *Nature* 174.4431 (1954), pp. 660–660.

[13] Sidney Loeb. “Production of energy from concentrated brines by pressure-retarded osmosis: I. Preliminary technical and economic correlations”. In: *Journal of Membrane Science* 1 (1976), pp. 49–63.

[14] Richard S Norman. “Water salination: a source of energy”. In: *Science* 186.4161 (1974), pp. 350–352.

[15] Andrea Achilli and Amy E Childress. “Pressure retarded osmosis: from the vision of Sidney Loeb to the first prototype installation”. In: *Desalination* 261.3 (2010), pp. 205–211.

[16] S Loeb and GD Mehta. “A two-coefficient water transport equation for pressure-retarded osmosis”. In: *Journal of Membrane Science* 4 (1978), pp. 351–362.

[17] Gurmukh D Mehta and Sidney Loeb. “Internal polarization in the porous substructure of a semipermeable membrane under pressure-retarded osmosis”. In: *Journal of Membrane Science* 4 (1978), pp. 261–265.

[18] GD Mehta and S Loeb. “Performance of permasep B-9 and B-10 membranes in various osmotic regions and at high osmotic pressures”. In: *Journal of Membrane Science* 4 (1978), pp. 335–349.

[19] F Vigo and C Uliana. “Suitability of reverse osmosis membranes for energy recovery by submarine osmotic power plants”. In: *Desalination* 60.1 (1986), pp. 45–57.

[20] Jan W Post et al. “Salinity-gradient power: Evaluation of pressure-retarded osmosis and reverse electrodialysis”. In: *Journal of membrane science* 288.1-2 (2007), pp. 218–230.

[21] JC Fair and JF Osterle. “Reverse electrodialysis in charged capillary membranes”. In: *The Journal of Chemical Physics* 54.8 (1971), pp. 3307–3316.

[22] John N Weinstein and Frank B Leitz. “Electric power from differences in salinity: the dialytic battery”. In: *Science* 191.4227 (1976), pp. 557–559.

[23] Ramato Ashu Tufa et al. “Progress and prospects in reverse electrodialysis for salinity gradient energy conversion and storage”. In: *Applied energy* 225 (2018), pp. 290–331.

[24] Bruce E Logan and Menachem Elimelech. “Membrane-based processes for sustainable power generation using water”. In: *Nature* 488.7411 (2012), pp. 313–319.

[25] David A Vermaas, Michel Saakes, and Kitty Nijmeijer. “Enhanced mixing in the diffusive boundary layer for energy generation in reverse electrodialysis”. In: *Journal of membrane science* 453 (2014), pp. 312–319.

[26] David A Vermaas, Michel Saakes, and Kitty Nijmeijer. “Power generation using profiled membranes in reverse electrodialysis”. In: *Journal of membrane science* 385 (2011), pp. 234–242.

[27] Piotr Długołęcki et al. “Ion conductive spacers for increased power generation in reverse electrodialysis”. In: *Journal of Membrane Science* 347.1-2 (2010), pp. 101–107.

[28] Bopeng Zhang, Haiping Gao, and Yongsheng Chen. “Enhanced ionic conductivity and power generation using ion-exchange resin beads in a reverse-electrodialysis stack”. In: *Environmental Science & Technology* 49.24 (2015), pp. 14717–14724.

[29] Enver Guler et al. “Tailor-made anion-exchange membranes for salinity gradient power generation using reverse electrodialysis”. In: *ChemSusChem* 5.11 (2012), pp. 2262–2270.

[30] REDstack Group. *King officially puts Blue Energy pilot plant into operation*. https://redstack.nl/en/koning-stelde-proefinstallatie-blue-energy-officieel-in-gebruik/. 2016.

[31] Michele Tedesco et al. “Performance of the first reverse electrodialysis pilot plant for power production from saline waters and concentrated brines”. In: *Journal of Membrane Science* 500 (2016), pp. 33–45.

[32] Michele Tedesco et al. “Towards 1 kW power production in a reverse electrodialysis pilot plant with saline waters and concentrated brines”. In: *Journal of Membrane Science* 522 (2017), pp. 226–236.

[33] Doriano Brogioli. “Extracting renewable energy from a salinity difference using a capacitor”. In: *Physical review letters* 103.5 (2009), p. 058501.

[34] BB Sales et al. “Direct power production from a water salinity difference in a membrane-modified supercapacitor flow cell”. In: *Environmental science & technology* 44.14 (2010), pp. 5661–5665.

[35] Fabio La Mantia et al. “Batteries for efficient energy extraction from a water salinity difference”. In: *Nano letters* 11.4 (2011), pp. 1810–1813.

[36] Roger F Harrington. *Introduction to electromagnetic engineering*. Courier Corporation, 2003.

[37] Johannes Lyklema. *Fundamentals of interface and colloid science: soft colloids*. Vol. 5. Elsevier, 2005.

[38] Zhijun Jia et al. “A membrane-less Na ion battery-based CAPMIX cell for energy extraction using water salinity gradients”. In: *RSC advances* 3.48 (2013), pp. 26205–26209.

[39] Samira Haj Mohammad Hosein Tehrani, Seyed Abolfazl Seyedsadjadi, and Ali Ghaffarinejad. “Application of electrodeposited cobalt hexacyanoferrate film to extract energy from water salinity gradients”. In: *RSC Advances* 5.38 (2015), pp. 30032–30037.

[40] Youcef Brahmi and Annie Colin. “New membrane and electrode assembly concept to improve salinity energy harvesting.” In: *Energy Conversion and Management* 254 (2022), p. 115297.

[41] Mathijs Janssen, Andreas Härtel, and René Van Roij. “Boosting capacitive blue-energy and desalination devices with waste heat”. In: *Physical review letters* 113.26 (2014), p. 268501.

[42] Xiuping Zhu et al. “Energy recovery from solutions with different salinities based on swelling and shrinking of hydrogels”. In: *Environmental science & technology* 48.12 (2014), pp. 7157–7163.

[43] Mingzhu Liu and Tianhua Guo. “Preparation and swelling properties of crosslinked sodium polyacrylate”. In: *Journal of Applied Polymer Science* 82.6 (2001), pp. 1515–1520.

[44] Fengjun Hua and Mengping Qian. “Synthesis of self-crosslinking sodium polyacrylate hydrogel and water-absorbing mechanism”. In: *Journal of materials science* 36.3 (2001), pp. 731–738.

[45] Mark Olsson, Gerald L Wick, and John D Isaacs. “Salinity gradient power: utilizing vapor pressure differences”. In: *Science* 206.4417 (1979), pp. 452–454.

[46] Statkraft Group. *Statkraft halts osmotic power investments*. https://www.statkraft.com/newsroom/news-and-stories/archive/2013/Statkraft-halts-osmotic-power-investments/. 2013.

[47] Andrea Cipollina and Giorgio Micale. “Sustainable energy from salinity gradients”. In: (2016).

[48] Anthony P Straub, Akshay Deshmukh, and Menachem Elimelech. “Pressure-retarded osmosis for power generation from salinity gradients: is it viable?” In: *Energy & Environmental Science* 9.1 (2016), pp. 31–48.

[49] S Sarp, Z Li, and J Saththasivam. “Pressure Retarded Osmosis (PRO): Past experiences, current developments, and future prospects”. In: *Desalination* 389 (2016), pp. 2–14.

[50] Jan W Post, Hubertus VM Hamelers, and Cees JN Buisman. “Influence of multivalent ions on power production from mixing salt and fresh water with a reverse electrodialysis system”. In: *Journal of Membrane Science* 330.1-2 (2009), pp. 65–72.

[51] David A Vermaas et al. “Fouling in reverse electrodialysis under natural conditions”. In: *Water research* 47.3 (2013), pp. 1289–1298.

[52] O Scialdone et al. “Investigation of electrode material–Redox couple systems for reverse electrodialysis processes. Part I: Iron redox couples”. In: *Journal of Electroanalytical Chemistry* 681 (2012), pp. 66–75.

[53] E Brauns. “Salinity gradient power by reverse electrodialysis: effect of model parameters on electrical power output”. In: *Desalination* 237.1-3 (2009), pp. 378–391.

[54] Menachem Elimelech and William A Phillip. “The future of seawater desalination: energy, technology, and the environment”. In: *science* 333.6043 (2011), pp. 712–717.

[55] KL Lee, RW Baker, and HK Lonsdale. “Membranes for power generation by pressure-retarded osmosis”. In: *Journal of membrane science* 8.2 (1981), pp. 141–171.

[56] Jim C Chen, Qilin Li, and Menachem Elimelech. “In situ monitoring techniques for concentration polarization and fouling phenomena in mem-

brane filtration". In: *Advances in Colloid and Interface Science* 107.2 (2004), pp. 83–108. ISSN: 0001-8686.

[57] Li Wang et al. "Nanopore-based power generation from salinity gradient: why it is not viable". In: *ACS nano* 15.3 (2021), pp. 4093–4107.

[58] J Troy Littleton and Barry Ganetzky. "Ion channels and synaptic organization: analysis of the Drosophila genome". In: *Neuron* 26.1 (2000), pp. 35–43.

[59] RD Keynes and Hiss Martins-Ferreira. "Membrane potentials in the electroplates of the electric eel". In: *The Journal of physiology* 119.2-3 (1953), p. 315.

[60] Jian Xu and David A Lavan. "Designing artificial cells to harness the biological ion concentration gradient". In: *Nature nanotechnology* 3.11 (2008), pp. 666–670.

[61] Wei Guo et al. "Energy harvesting with single-ion-selective nanopores: a concentration-gradient-driven nanofluidic power source". In: *Advanced functional materials* 20.8 (2010), pp. 1339–1344.

[62] Alessandro Siria et al. "Giant osmotic energy conversion measured in a single transmembrane boron nitride nanotube". In: *Nature* 494.7438 (2013), pp. 455–458.

[63] Michal Macha et al. "2D materials as an emerging platform for nanopore-based power generation". In: *Nature Reviews Materials* 4.9 (2019), pp. 588–605.

[64] Jiandong Feng et al. "Single-layer MoS2 nanopores as nanopower generators". In: *Nature* 536.7615 (2016), pp. 197–200.

[65] Ryan C Rollings, Aaron T Kuan, and Jene A Golovchenko. "Ion selectivity of graphene nanopores". In: *Nature communications* 7.1 (2016), pp. 1–7.

[66] Michael I Walker et al. “Extrinsic cation selectivity of 2D membranes”. In: *ACS nano* 11.2 (2017), pp. 1340–1346.

[67] Neus Godino et al. “Mass transport to nanoelectrode arrays and limitations of the diffusion domain approach: theory and experiment”. In: *The Journal of Physical Chemistry C* 113.25 (2009), pp. 11119–11125.

[68] Joost H Weijs and Detlef Lohse. “Why surface nanobubbles live for hours”. In: *Physical review letters* 110.5 (2013), p. 054501.

[69] Makusu Tsutsui et al. “Sparse multi-nanopore osmotic power generators”. In: *Cell Reports Physical Science* 3.10 (2022), p. 101065. ISSN: 2666-3864.

[70] Matteo Altissimo. “E-beam lithography for micro-/nanofabrication”. In: *Biomicrofluidics* 4.2 (2010), p. 026503.

[71] Ampere A Tseng et al. “Electron beam lithography in nanoscale fabrication: recent development”. In: *IEEE Transactions on electronics packaging manufacturing* 26.2 (2003), pp. 141–149.

[72] Deying Xia, Juchao Yan, and Shifeng Hou. “Fabrication of nanofluidic biochips with nanochannels for applications in DNA analysis”. In: *Small* 8.18 (2012), pp. 2787–2801.

[73] Chao Wang et al. “Printing of sub-20 nm wide graphene ribbon arrays using nanoimprinted graphite stamps and electrostatic force assisted bonding”. In: *Nanotechnology* 22.44 (2011), p. 445301.

[74] Sung Hee Ko et al. “Nanofluidic preconcentration device in a straight microchannel using ion concentration polarization”. In: *Lab on a Chip* 12.21 (2012), pp. 4472–4482.

[75] Yoon Gi Kim et al. “Chemical vapor deposition of boron and boron nitride from decaborane (14)”. In: *Journal of Vacuum Science & Technology A: Vacuum, Surfaces, and Films* 7.4 (1989), pp. 2796–2799.

[76] Bart Jozef Van Zeghbroeck. *Principles of semiconductor devices*. 2011.

[77] Etienne Guyon et al. *Physical hydrodynamics*. Oxford university press, 2001.

[78] Hyomin Lee et al. "Diffusiophoretic exclusion of colloidal particles for continuous water purification". In: *Lab on a Chip* 18.12 (2018), pp. 1713–1724.

[79] Kei Matsuyama et al. "Power generation system based on pressure retarded osmosis with a commercially-available hollow fiber PRO membrane module using seawater and freshwater". In: *Desalination* 499 (2021), p. 114805.

[80] Clara B Picallo et al. "Nanofluidic osmotic diodes: Theory and molecular dynamics simulations". In: *Physical review letters* 111.24 (2013), p. 244501.

[81] Adolph Fick. "V. On liquid diffusion". In: *The London, Edinburgh, and Dublin Philosophical Magazine and Journal of Science* 10.63 (1855), pp. 30–39.

[82] Brian J Kirby. *Micro-and nanoscale fluid mechanics: transport in microfluidic devices*. Cambridge university press, 2010.

[83] Alexandros Daniilidis et al. "Experimentally obtainable energy from mixing river water, seawater or brines with reverse electrodialysis". In: *Renewable energy* 64 (2014), pp. 123–131.

[84] John H Lau. "Recent advances and new trends in flip chip technology". In: *Journal of Electronic Packaging* 138.3 (2016), p. 030802.

[85] Shantanu Bhattacharya et al. "Studies on surface wettability of poly (dimethyl) siloxane (PDMS) and glass under oxygen-plasma treatment and correlation with bond strength". In: *Journal of microelectromechanical systems* 14.3 (2005), pp. 590–597.

[86] Michelle L Kovarik, Kaimeng Zhou, and Stephen C Jacobson. “Effect of conical nanopore diameter on ion current rectification”. In: *The Journal of Physical Chemistry B* 113.49 (2009), pp. 15960–15966.

[87] Qi Liu et al. “Asymmetric properties of ion transport in a charged conical nanopore”. In: *Physical Review E* 75.5 (2007), p. 051201.

[88] Naichao Li et al. “Conical nanopore membranes. Preparation and transport properties”. In: *Analytical chemistry* 76.7 (2004), pp. 2025–2030.

[89] James M Gere and Barry J Goodno. *Mechanics of materials*. Cengage learning, 2012.

[90] Myron J Rand and James F Roberts. “Preparation and properties of thin film boron nitride”. In: *Journal of the Electrochemical Society* 115.4 (1968), p. 423.

[91] Preeti Sharma. “Coupled electrokinetic fluxes in a single nanochannel for energy conversion”. PhD thesis. Université Grenoble Alpes, 2017.

[92] Kanishka Biswas and S Kal. “Etch characteristics of KOH, TMAH and dual doped TMAH for bulk micromachining of silicon”. In: *Microelectronics journal* 37.6 (2006), pp. 519–525.

[93] Yu Chen, Hang-Rong Chen, and Jian-Lin Shi. “Construction of homogenous/heterogeneous hollow mesoporous silica nanostructures by silica-etching chemistry: principles, synthesis, and applications”. In: *Accounts of chemical research* 47.1 (2014), pp. 125–137.

[94] Maki Suemitsu, Tetsuya Kaneko, and Nobuo Miyamoto. “Low Temperature Silicon Surface Cleaning by HF Etching/Ultraviolet Ozone Cleaning (HF/UVOC) Method (I)–Optimization of the HF Treatment–”. In: *Japanese journal of applied physics* 28.12R (1989), p. 2421.

[95] Moslehi Wong, MM Moslehi, and DW Reed. “Characterization of Wafer Cleaning and Oxide Etching Using Vapor-Phase Hydrogen Fluoride”. In: *Journal of the Electrochemical Society* 138.6 (1991), p. 1799.

[96] Alexandra Borók, Kristóf Laboda, and Attila Bonyár. “PDMS bonding technologies for microfluidic applications: A review”. In: *Biosensors* 11.8 (2021), p. 292.

[97] Sorin Cristoloveanu and Sheng Li. *Electrical characterization of silicon-on-insulator materials and devices*. Vol. 305. Springer Science & Business Media, 1995.

[98] PLF Hemment et al. “Novel dielectric/silicon planar structures formed by ion beam synthesis”. In: *Nuclear Instruments and Methods in Physics Research Section B: Beam Interactions with Materials and Atoms* 21.1-4 (1987), pp. 129–133.

[99] KJ Reeson et al. “The role of implantation temperature and dose in the control of the microstructure of SIMOX structures”. In: *Microelectronic Engineering* 8.3-4 (1988), pp. 163–186.

[100] Michel Bruel. “The history, physics, and applications of the Smart-Cut® process”. In: *MRS bulletin* 23.12 (1998), pp. 35–39.

APPENDIX A

Modelling the Elemental Exchanger using *COMSOL Multiphysics*

This appendix chapter contains the technical details of the implementing a 1D simulation of the Elemental Exchanger in the *COMSOL Multiphysics* software. We use a equation-based modelling approach corresponding to the numerical resolution of the transport equations given in Chapter 4 Sections 2 and 3.

We start with the *Model Wizard* and select the *1D* space dimension that prepares the software to support a geometry suitable for our simulation. The next step is the selection of the *Physics Interfaces*, where we select *General Form PDEs* with two dimensionless variables and *Domain ODEs and DAEs*, which will be elaborated in the upcoming subsections. Following the physics interfaces, we select the type of *Study* we wish to perform on the model, where we choose the option for *Stationary*. After the study selection we get the access to the main interface of *COMSOL*, elaborated in the following subsections:

A.1 Simulation Geometry

The simulation geometry for our 1D model is just a straight line that is equal to the length of the exchanger (L_M). Therefore for the initial simulation we define a parameter, L in the parameter tab and declare its value to be equal to 100μm. Following this, we select the *Interval* option with *Coordinates* $(0, L)$ in the *Geometry* tab under the *Component* list. Additionally we also declare a point (*P*) 0.1μm

from the origin by selecting *Point* in the geometry tab and select *Build All Objects* option. This results our geometry being displayed on the *Graphics* pane on the right side of the window.

The additional point in the geometry is essential when defining the mesh required for the simulation as the ionic concentration in the microchannels varies rapidly in the beginning stages of the exchanger which will be elaborated further in the later subsection.

A.2 Governing Equations and Boundary Conditions

The governing equations (eq.4.13) are entered in the *General Form PDE* tab in the component list, where term PDE stands for *Partial Differential Equation*. The two variables that will be solved for are the two normalized microchannel concentrations ($\bar{c}_l, \bar{c}_h$) defined in equation 4.12. When this tab is selected, it allows the user to select the dimensions of the source term, which in our case is the nanochannel flux term after normalization with dimension [m^{-2}]. There are multiple sub-tabs under *General Form PDE* elaborated as follows:

A.2.1 General Form PDE sub-tab

When selected with two variables, this option allows the user to input the flux term and the source term for the governing equation, along with damping and mass coefficient. The equation is input in the following form:

$$e_a \frac{\partial^2 u}{\partial t^2} + d_a \frac{\partial u}{\partial t} + \nabla.\Gamma = f \qquad \nabla = \frac{\partial}{\partial x} \tag{A.1}$$

where e_a, d_a are the mass and the damping coefficient respectively, Γ is the flux term, f is the source term and u is a column matrix with two variables being solved.

When comparing eq. 4.13 and eq. A.1, it is evident that the mass and damping coefficients will be a zero matrix, as our governing equations are steady state equations with no time dependence. Hence the final governing equation in matrix form is given as:

$$\nabla. \underbrace{\begin{bmatrix} -(\frac{1}{Pe})(\frac{\partial \bar{c}_h}{\partial x}) + \frac{1}{L}\bar{c}_h \\ -(\frac{1}{Pe})(\frac{\partial \bar{c}_l}{\partial x}) + \frac{1}{L}\bar{c}_l \end{bmatrix}}_{\Gamma} = \underbrace{\begin{bmatrix} -\frac{(nanoj)}{2L^2Sh} \\ \frac{(nanoj)}{2L^2Sh} \end{bmatrix}}_{f} \qquad u = \begin{bmatrix} \bar{c}_h \\ \bar{c}_l \end{bmatrix} \tag{A.2}$$

where $(nanoj)$ is the implicit function $(1+S)(\mathcal{E}-\Delta\Psi)$, which will be calculated separately and is detailed in the "Algebraic Compuations" subsection. It should be noted that a partial space derivative of a variable is written as "variable name" followed by the name of the spacial axis. For example, if the variable name chosen for ionic concentration is "C" then ∂C/∂x would be written as "Cx".

The next option in the tab is for *Zero Flux* boundary condition, which need not be altered as it will be overridden by the boundary conditions we will apply. Following this, we have the *Initial Values* tab where we input the inlet values of $\bar{c}_l, \bar{c}_h$ from equation 4.12. Similar to the microchannel length, the real ionic concentrations of the microchannel liquids in [mol/m^3] are first declared as parameters, to give us the ability to vary the concentrations after each study.

The last step in this section is choosing the boundary condition at the inlet and outlet. At both these points, the microchannel liquids posses a flux, which is responsible for their travel across or out of the exchanger. Hence we choose the *Flux/Source* option from the right click menu on the main tab and select the outlet

point (right most point in the geometry). The equation for the *Flux/Source* option is as follows:

$$-n.\Gamma = g - qu \tag{A.3}$$

where n is the normal vector which always points in the outward direction from the geometry (positive $x-$axis in our study), g is the boundary flux term, q is the boundary absorption term and Γ, u are the flux and the variable matrices respectively. The final equation of flux at this boundary takes the following form:
Inlet:

$$-n. \begin{bmatrix} -(\frac{1}{Pe})(\frac{\partial \bar{c}_h}{\partial x}) + \frac{1}{L}\bar{c}_h \\ -(\frac{1}{Pe})(\frac{\partial \bar{c}_l}{\partial x}) + \frac{1}{L}\bar{c}_l \end{bmatrix} = \frac{1}{L} \begin{bmatrix} \bar{c}_H \\ \bar{c}_L \end{bmatrix} \tag{A.4}$$

here $\bar{c}_H$ and $\bar{c}_L$ are the normalized initial concentrations in the microchannels.
Outlet:

$$-n. \begin{bmatrix} -(\frac{1}{Pe})(\frac{\partial \bar{c}_h}{\partial x}) + \frac{1}{L}\bar{c}_h \\ -(\frac{1}{Pe})(\frac{\partial \bar{c}_l}{\partial x}) + \frac{1}{L}\bar{c}_l \end{bmatrix} = -\frac{1}{L} \begin{bmatrix} \bar{c}_h \\ \bar{c}_l \end{bmatrix} \tag{A.5}$$

A.3 Algebraic Computations

The algebraic computations involve the computations of all the variables that vary with the variation of the microchannel ion concentrations. We declare five separate *Domain ODEs and DAEs* by selecting it from the *Physics* tab on the *Ribbon Toolbar* on the top of the screen. The acronyms "ODE" and "DAE" stand for "ordinary differential equation" and "differential-algebraic equation" respectively. All the algebraic computations are performed simultaneously along with the *General form PDE* and hence these equations can be inherently coupled to each other. Each of these equations have only one dimensionless variable and the source terms is also non-dimensional. The equations and the associated variables are:

A.3.1 DAE - 1: Nanochannel Selectivity (S) Variable name: v

To facilitate the solving of equation 4.3, the expression for nanochannel selectivity (t) is modified by defining a new variable v as follows:

$$t = \frac{t_h - t_l}{2\tanh(v)} + \frac{t_h + t_l}{2} \tag{A.6}$$

As a result the implicit equation now takes the form:

$$v\left(\frac{t_h - t_l}{\tanh(v)} + (t_h + t_l)\right) = \Delta\Psi - \ln\left(\frac{\bar{c}_h(t_l + 1)}{\bar{c}_l(t_h + 1)}\right) \tag{A.7}$$

In the *Domain ODE and DAE* tab, the initial value for the variable is chosen to be a small positive value arbitrarily. This small value allows *COMSOL* to start the search for the roots of equation A.7 in the vicinity of the initial value. The initial value chosen in this study is $v = 10^{-4}$.

The next step is to input eq. A.7 in the *Algebraic Equation* sub-tab. *COMSOL* solves an algebraic equation for zero, hence the input equation is written as:

$$v\left(\frac{t_h - t_l}{\tanh(v)} + (t_h + t_l)\right) + \ln\left(\frac{\bar{c}_h(t_l + 1)}{\bar{c}_l(t_h + 1)}\right) - \Delta\Psi \tag{A.8}$$

The remaining options under the main tab are left unaltered.

A.3.2 DAE - 2: Nanochannel Flux (J_{nano}) Variable name: *nanoj*

The expression for nanochannel flux is changes to accommodate the variable "v", which now quantifies the nanochannel selectivity. The motive for the introduction

of variable v was to be able to simplify the expression of the nanochannel flux using Taylor expansion of certain hyperbolic functions. Using equation A.6 to express the nanochannel flux per unit exchanger length (eq. 4.2), we arrive at:

$$J^{+}_{nano} = -\frac{D\sigma}{2eW}\left(2 + \frac{t_h - t_l}{\tanh(v)} + t_h + t_l\right)(\mathcal{E} - \Delta\Psi) \tag{A.9}$$

This equation can be further simplified by using the implicit equation in v (eq. A.7) to substitute the normalized potential ($\Delta\Psi$) and introducing the following variables:

$$ss = (t_h + t_l) \qquad dd = (t_h - t_l) \qquad ff = \ln\left(\frac{\bar{c}_h(t_l + 1)}{\bar{c}_l(t_h + 1)}\right) \tag{A.10}$$

These variables will be evaluated individually on *COMSOL* as they only vary with the change in microchannel concentrations. From eq. A.7, the normalized potential can be substituted as:

$$\mathcal{E} - \Delta\Psi = dd\left(1 - \frac{v}{\tanh(v)}\right) + vss \tag{A.11}$$

This leads to the following expression for the nanochannel flux per unit exchanger length:

$$J^{+}_{nano} = \frac{D\sigma}{2eW}\frac{1}{\tanh(v)}\big(dd + (ss+2)\tanh(v)\big)\Big(dd\big(\frac{v}{\tanh(v)} - 1\big) + vss\Big) \tag{A.12}$$

The equation above calculates the value of nanochannel flux with high accuracy in *COMSOL* as long as the variable v does not approach values close to zero. Error in calculation of the nanochannel flux when v approaches zero arise as the term with hyperbolic tangent approaches infinity leading no an undefined nanochannel flux. This is rectified using Taylor expansion to approximate the value of the hyperbolic tangent as follows:

$$\frac{1}{\tanh(v)} = \frac{1}{v} + \frac{v}{3} - \frac{v^3}{45} \quad ; \quad \frac{v}{\tanh(v)} - 1 = \frac{v^2}{3} - \frac{v^4}{45} \qquad v \leq 0.1 \tag{A.13}$$

Hence the nanochannel flux when $v \to 0$ is expressed as:

$$J^{+}_{nano} = \frac{D\sigma}{2eW}\left(1 + \frac{v^2}{3} - \frac{v^4}{45}\right)\big(dd + (ss+2)\tanh(v)\big)\left(dd\left(\frac{v}{3} - \frac{v^3}{45}\right) + ss\right) \tag{A.14}$$

The equations input in *COMSOL* are the non-dimensional functions in equations A.12 and A.14. The dimensional coefficient in the equation is declared as a parameter. Therefore:

$$nanoj = \frac{1}{\tanh(v)}\big(dd + (ss+2)\tanh(v)\big)\Big(dd\big(\frac{v}{\tanh(v)} - 1\big) + vss\Big) \quad v > 0.1 \tag{A.15a}$$

$$nanoj = (1 + \frac{v^2}{3} - \frac{v^4}{45})\big(dd + (ss+2)\tanh(v)\big)\left(dd(\frac{v}{3} - \frac{v^3}{45}) + ss\right) \quad v \leq 0.1 \tag{A.15b}$$

The coefficient (J_{coef}), decalared as a parameter hence takes the form:

$$J_{coef} = \frac{D\sigma}{2eW} \quad \text{or} \quad J_{coef} = \frac{D\sigma}{2FW} \tag{A.16}$$

The Faraday constant (F) is used instead of the fundamental charge (e) when the input concentrations have the units [mol.m^{-3}].

The equations are written in the *Algebraic Equations* sub-tab, while the remaining options are left unaltered.

A.3.3 DAE - 3: $t_h + t_l$ — Variable name: *ss*

The expression for this variable is relatively simple and hence left unmodified. It is however important to provide an initial value to this variable as it should be equal to its value for the inlet concentration in the microchannels. The expression and the initial value is written as:

$$ss = \sqrt{1 + \bar{c}_h^2} + \sqrt{1 + \bar{c}_l^2} \tag{A.17a}$$

$$ss_{init} = \sqrt{1 + \left(\frac{FHc_h^{in}}{\sigma}\right)^2} + \sqrt{1 + \left(\frac{FHc_l^{in}}{\sigma}\right)^2} \tag{A.17b}$$

ss_{init} is the initial value of the variable and $c_{l/h}^{in}$ are the inlet concentrations in the low/high concentration microchannels respectively in the units [mol.m^{-3}].

A.3.4 DAE - 4: $t_h - t_l$ — Variable name: *dd*

This variable is treated exactly the same as the variable ss. The expression and the initial value for the variable dd is given below:

$$dd = \sqrt{1 + \bar{c}_h^2} - \sqrt{1 + \bar{c}_l^2} \tag{A.18a}$$

$$dd_{init} = \sqrt{1 + \left(\frac{FHc_h^{in}}{\sigma}\right)^2} - \sqrt{1 + \left(\frac{FHc_l^{in}}{\sigma}\right)^2} \tag{A.18b}$$

dd_{init} is the initial value of the variable and $c_{l/h}^{in}$ are the inlet concentrations in the low/high concentration microchannels respectively in the units [mol.m^{-3}].

A.3.5 DAE - 5: $\ln\left(\frac{\bar{c}_h(t_l+1)}{\bar{c}_l(t_h+1)}\right)$ Variable name: *ff*

The expression for the variable ff is a logarithm of a fraction is written below:

$$ff = \frac{1}{2}\ln\left(\frac{t_l+1}{t_l-1}\frac{t_h-1}{t_h+1}\right) \tag{A.19}$$

Therefore the solution for variable ff does not converge when t_l, t_h approach 1. Hence the expression is modified multiplying the numerator and the denominator in the fraction by the factor $(t_l+1)(t_h+1)$ to ensure that the denominator is always positive:

$$ff = \frac{1}{2}\ln\left(\frac{(t_l+1)^2(t_h^2-1)}{(t_l^2-1)(t_h+1)^2}\right) = \ln\left(\frac{\bar{c}_h(t_l+1)}{\bar{c}_l(t_h+1)}\right) \quad \text{as} \quad t_{l/h}^2 - 1 = \bar{c}_{l/h}^2 \tag{A.20}$$

Also since the variables t_l and t_h can be expressed as a function of ss and dd the final expression written in *COMSOL* takes the form:

$$ff = \ln\left(\frac{(ss-dd+2)\bar{c}_h}{(ss+dd+2)\bar{c}_l}\right) \tag{A.21}$$

The initial value of the this variable is written directly as a function of the initial microchannel concentrations:

$$ff_{init} = \ln\left(1+\sqrt{1+\left(\frac{FHc_l^{in}}{\sigma}\right)^2}\right) - \ln\left(1+\sqrt{1+\left(\frac{FHc_h^{in}}{\sigma}\right)^2}\right) + \ln\left(\frac{c_h^{in}}{c_l^{in}}\right) \tag{A.22}$$

This concludes all the algebraic computations for the elemental exchanger and we proceed to the configurations specific to the finite element simulation.

A.4 Mesh

As mentioned previously, defining the *mesh* is the fundamentally important aspect of finite element analysis. A mesh splits the simulation geometry into *nodes* and all the governing equations are solved at each individual node, revealing the values of the respective variables there. High number of nodes accounts to high accuracy of the solution but it also increases the simulation time significantly.

Since our geometry is a straight line, the nodes here are a number of points on the straight line where the variables $c_{l/h}^{-}, v, nanoj, ss, dd$ and ff are computed simultaneously.

The construction of the mesh is done by selecting the *Mesh* option in the *Model Builder* sidebar. As we want to define the mesh suitable for our geometry, the option of *User Defined Mesh* is selected from the *Sequence type* option. This allows the user complete freedom in the node distribution. Upon selecting a user defined mesh, it can be noticed that two additional options namely *Size* and *Edge* appear on the mesh sub-tab. The next step is to select *Distribution* from the right-click menu in the *Mesh* tab. The *Distribution* setting overrides the *Size* feature of the mesh in the selected domain of the geometry and gives the user control cover the number of nodes and the distribution of the nodes in the domain.

We first start by selecting *Domain - 1*, which is the segment of the line from the origin to the point *P*, 0.1μm from the origin. As this point is close to the inlet of the exchanger, the nodes here need to be dense to account for rapid change in microchannel concentrations. Hence we choose the following options:

- Domain Selection: 1 Number of elements: 100
- Element ratio: 10 Growth formula: Geometric Sequence

This specifies the mesh to have 100 nodes (*elements*) and the distance between each of the nodes increases by a factor of 10 over the length of 0.1μm.

The *Distribution* option, however, requires the user to define a feature on the geometry to notify the software that the region is of special interest. This is done by selecting *Domain - 1* in the *Edge* sub-tab and it below the *Distribution* sub-tab. This indicates *COMSOL* that a user-specified distribution of nodes takes place on *Domain-1* which happens to be an *Edge*.

Similar steps are followed for the remainder of the geometry. We select *Size* and *Edge* option again from the right-click menu in the mesh tab. This time we use a predefined mesh calibrated for *fluid dynamics* and select the *Extremely fine* element size from the *Size* sub-tab. We select the *Edge* option and choose *Remaining* in the *Domain Selection* and finally select *Build Mesh*. It should result to a mesh similar to the one shown in fig.A.1.

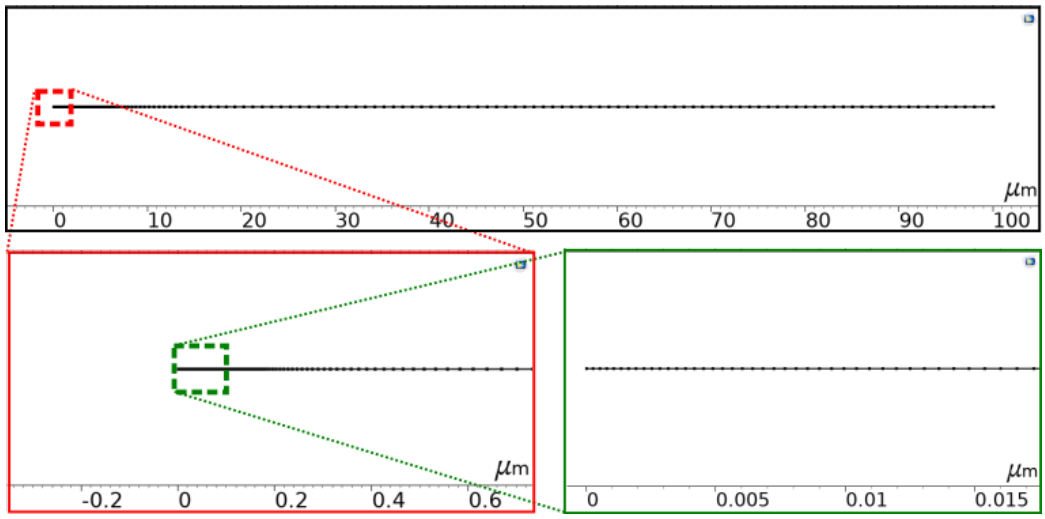

Figure A.1: *COMSOL* geometry after meshing. Nodes are represented by points on the line segment.

A.5 Study Steps and Solver Configuration

The study chosen for this simulation is *Stationary Study* which solves all the governing equations simultaneously for a given value of geometrical parameters, surface charge and the potential difference across the electrodes. The dependent variables are the normalized concentrations ($\bar{c_l}, \bar{c_h}$), v, $nanoj$, ss, dd and ff; which are fully coupled to one another.

By default the *Study* tab on the *Model Builder* is configured to solve simultaneous equations but as we declared the normalized potential difference between the electrodes ($\Delta\Psi$) as a parameter with a fixed value, we need to add an *Auxiliary Sweep* to the *Stationary Study* which allows us to plot the IV-characteristics of the exchanger. This is done by selecting *Stationary - Step 1 - Study Extensions - Auxiliary Sweep - ΔV* and selecting a range form 0mV to 100mV. The increments are small (0.01 mV) till the voltage reaches 1 mV and is increased to 2.5mV for the remaining range of voltages. Select the *Compute* option from the *Quick Access Toolbar* on the screen and if done correctly, the simulation should be finished under two minutes.

Next step is to vary the convection velocity of fluids in the microchannel by changing the value of Sherwood number (Sh). This is done by adding an extra *Parametric Sweep* in the study and selecting a range of Sherwood number. For our study we varied the Sherwood number from 10^{-3} to 10^{8} with 3 steps/decade increase. It is to be noted that the changing velocity results to a proportional increase in the Péclet number also. Hence the results obtained need to account for an increase in both the parameters (Sh, Pe).

Note: *COMSOL* can be configured to show certain results of the simulations simultaneously as it computes. This is very useful in determining the mesh dis-

tribution along the simulation geometry. In our study observing the variation of the normalized concentration in the high concentration microchannel indicates the accuracy of the mesh. This is performed before adding the parametric sweep for Sherwood number. Add a *Line Graph* in a *1D Plot Group* in the *Results*, after the initial stationary simulation. In the *1D Plot Group* tab, select the appropriate *Data Set* (default Study - 1), *Parameter Selection*(ΔV) - *Last*, choose *All domains* and plot $\bar{c}_h$ in the *y -Axis data*. This should be done before . Afterwards, select *Study - Solver Configurations - Stationary - Fully Coupled - Results While Solving*. Here, select *1D Plot Group 1* and check the *Plot* option. Errors in computation due to improper mesh configurations have a clear sign and is explained in the fig. A.2.

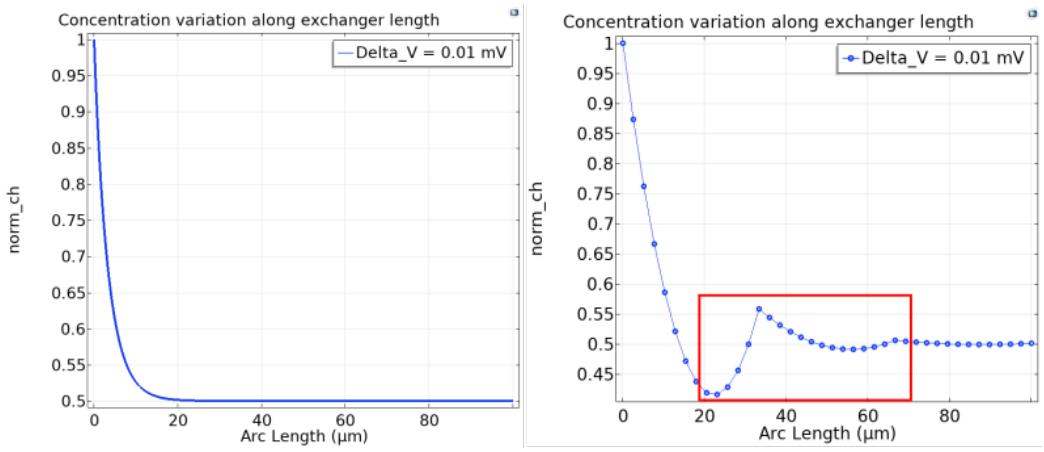

Figure A.2: Variation of normalized concentration in the high concentration microchannel. Image on the left indicates a good mesh and left image is the result of a coarse mesh. Concentration in high concentration microchannel should decrease monotonically with the exchanger length. Any kinks in the normalized concentration (red box) indicates the presence of mesh errors/imperfections.

A.6 Results and Evaluation Groups

Once the simulation is completed, the resulting values of the variables are stored as *Data Sets*, which can be accessed through the *Results* tab in the *Model Builder*.

The desired results from the simulation can be calculated using an *Evaluation Group*. An evaluation group gives the user the ability to perform computations on the evaluated variables. Here we can calculate the magnitude of nanochannel flux per unit length, electrical current and the power density by integrating the variables over the exchanger length. The expressions for quantities with normalized variables $\bar{c}_h, \bar{c}_l$ and v is given below:

$$J_{nano} = -\frac{D\sigma}{2FW}\int_0^L \frac{1}{L}(nanoj)dL \tag{A.23a}$$

$$I = -\frac{D\sigma}{W}\int_0^L \left(\frac{dd}{\tanh(v)} + ss\right)(dd + ff - \Delta\Psi)dL \tag{A.23b}$$

$$Pd_{elec} = -\frac{D\sigma}{bLW}\frac{k_B T}{e}\int_0^L \Delta\Psi\left(\frac{dd}{2\tanh(v)} + \frac{ss}{2}\right)(dd + ff - \Delta\Psi)dL \tag{A.23c}$$

The *Line Integration* option inside the evaluation group calculates the integral of the above expressions while the respective coefficients are declared as *Parameters*. Since each study consists of two parametric sweeps ($\Delta V, Sh$), the user can plot the variation of nanochannel flux with voltage, IV characteristics for the exchanger for a given Sherwood number and also the maximum power per unit exchanger surface with varying Sherwood number. The maxima of each quantity can be extracted by selecting *Operation - Maximum* in the *Data Series Operation* at the bottom of *Line Integration* screen.

This concludes the technical aspects of performing finite element simulations on the elemental exchanger using the *COMSOL Multiphysics* environment.

Abstract

The mixing of two electrolyte solutions of different concentrations is characterized by a free enthalpy of mixing. The conversion of this enthalpy into useful mechanical work or electricity has the potential to be a new source of clean renewable energy. The energy generated by this process is termed as ``osmotic energy'', or more specifically “blue energy'' when energy is generated by the mixing of sea water with river water. The necessity to drastically lessen the world's reliance on fossil fuels and the remarkable advancement of membrane technology have encouraged the development of novel techniques for harvesting blue energy. The establishment of large-scale power plants focused at harvesting this energy revealed some inherent limitations in membrane-based approaches for the extraction of blue energy, most notably concentration polarization. This manuscript proposes a silicon-based nanofluidic exchanger, which aims at optimizing the coupled solute transport at the microscale and nanoscale to minimize concentration polarization issues and enhance energy recovery. The focus of this manuscript is on the theoretical modelling of the exchanger and the optimization of the exchanger reveals an expected power density two magnitudes higher than existing strategies aimed at blue energy harvesting. These theoretical results are used to propose a fabrication protocol for a Multiscale Exchanger, in collaboration with CEA-Leti, incorporating recent developments of the microfabrication industry to produce minute channels with a large potential for parallelization.

Resumé

Le mélange de deux solutions électrolytiques de concentrations différentes est caractérisé par une enthalpie libre de mélange. Sa conversion en travail mécanique utile ou en électricité peut constituer une source d’énergie renouvelable propre communément appelée “énergie osmotique” ou “énergie bleue” dans le cas du mélange d’eau de rivière et d’eau de mer. La nécessité de réduire drastiquement notre dépendance aux combustibles fossiles et le développement remarquable de nouvelles membranes sélectives ont encouragé la mise au point de nouvelles techniques d’extraction de l’énergie bleue. La mise en place de centrales électriques à grande échelle a permis d’identifier certaines limites inhérentes aux approches membranaires pour l’extraction de l’énergie bleue, notamment la polarisation de concentration. Dans ce manuscrit, nous présentons un échangeur nanofludique à base de silicium qui vise à optimiser le transport couplé des solutés à l’échelle nanométrique et à l’échelle microscopique afin de minimiser les problèmes de polarisation de concentration et d’augmenter la récupération d’énergie. L’accent est mis sur la modélisation théorique d’un tel échangeur. Des densités de puissance de deux ordres de magnitudes supérieures aux stratégies existantes sont ainsi prédites. Ces résultats théoriques ont été utilisés pour concevoir un protocole de fabrication d’un échangeur multi-échelle, en collaboration avec le CEA-Leti, incorporant les développements récents de l’industrie de la microfabrication pour produire une série de canaux infimes massivement parallélisés. La dernière section du manuscrit discute d’un tel potentiel de parallélisation, qui pourrait conduire à un changement de paradigme dans la génération d’énergie basée sur le gradient de salinité en utilisant des nanopores.